SUM RULES AND PHOTON EMISSION IN HADRONIC MATTER

A Dissertation

by

NATHAN PRESCOTT MONTGOMERY HOLT

Submitted to the Office of Graduate and Professional Studies of
Texas A&M University
in partial fulfillment of the requirements for the degree of

DOCTOR OF PHILOSOPHY

Chair of Committee,	Ralf Rapp
Committee Members,	Rainer Fries
	Carl Gagliardi
	Philip Yasskin
Head of Department,	George Welch

August 2016

Major Subject: Physics

Copyright 2016 Nathan Prescott Montgomery Holt

ABSTRACT

In this work, we examine properties of quantum chromodynamics (QCD) at moderate temperatures and density. These conditions are reached in the later stages of ultra-relativistic heavy-ion collisions after the matter has cooled sufficiently to rehadronize from a quark-gluon plasma. The properties of matter in this stage are expected to change smoothly with temperature. We explore this behavior in two ways. First, we use finite-temperature sum rules to analyze the properties of vector and axial-vector spectral functions at low temperatures. Previous models used in sum rule analyses frequently led to ambiguous applications. Here we avoid such ambiguities by using an improved vacuum spectral function model together with a strict leading-order-in-temperature expansion. This results in well-defined finite-temperature spectral functions. Additionally, we incorporate a finite pion mass, which we show induces an analytical violation of the sum rules. We then proceed to numerically measure that violation.

Second, we calculate thermal photon emissivities of QCD matter from interactions involving both mesons and baryons. We identify a novel source of thermal photons from a system composed of π, ρ, and ω mesons, then calculate photon emission rates from this system using both relativistic kinetic theory and thermal field theory. These rates are compared to existing calculations and found to be significant. We then calculate thermal photon emission rates from baryon interactions, using an exhaustive set of both strange and non-strange particles. We again find novel sources of photons from this system, compare the total rates to calculations of current state-of-the-art photon emission rates, and find them to be comparable.

DEDICATION

The following people were integral in my path to where I am today.

The Reverend William Mayes Holt

Mrs. Patricia Faye Harper Holt

Dr. Marisa Rachel Adelman

Mr. Court Donner

Words can never truly convey my thanks or my gratitude for what you have given me and for what you have done for me. I would not be where I am without your unwavering confidence, love, and support.

ACKNOWLEDGEMENTS

First of all, I would like to thank my advisor Dr. Ralf Rapp for his patience, understanding, and motivation. I am truly lucky to have seen your presentation on October 5, 2010.

I would also like to thank the following people. Each of you has had a tremendous impact on my life, each in your own way. I am forever grateful for the grace you have shown me.

- Dr. Michael Causey
- Ms. Joy Durham
- Dr. Paul Hohler
- Mr. Noah Hungate
- Dr. Victor Montemayor
- Mr. Scott Pierce
- Dr. S. Steve Snow
- Mr. Marshall Stern
- Mr. Mark Summarell
- Mr. Dave Tate
- Mr. Dante Trudel

This work has been supported by the US National Science Foundation under Grant Nos. PHY-0969394 and PHY-1306359.

NOMENCLATURE

ALEPH	Apparatus for LEP PHysics at CERN
Condensate	The vacuum expectation value of a quantum field
KT	Kinetic Theory
LEP	Large Electron-Positron collider
LHS	Left-Hand Side
OPE	Operator Product Expansion
PCAC	Partial Conservation of Axial-vector Current
PDG	Particle Data Group
QCD	Quantum ChromoDynamics
QCDSR	Quantum ChromoDynamics Sum Rule
RIKM	Relativistically Improved K-matrix Model
RHS	Right-Hand Side
TFT	Thermal Field Theory
VMD	Vector Meson Dominance
WSR	Weinberg-type Sum Rule

In this work we use the following conventions:

- the Minkowski metric is $g_{\mu\nu} = \mathrm{Diag}(+1, -1, -1, -1)$,
- the speed of light in vacuum c, reduced Planck's constant $\hbar$, and Boltzmann's constant k_B are all defined to be unity,
- Lowercase Roman indices a, b, c, ... indicate Cartesian space components of isospin,

- Lowercase Roman indices i, j, k, ... indicate Cartesian components of spin (i.e., spatial components of a four-vector),
- Lowercase Greek letters α, β, μ, ν, ... indicate components of four-vectors, and
- the Dirac gamma matrices are in the Dirac representation, such that $\gamma^0 = \text{Diag}(+1, +1, -1, -1)$.

TABLE OF CONTENTS

Page

LIST OF FIGURES

FIGURE Page

LIST OF TABLES

TABLE Page

1. INTRODUCTION AND MOTIVATION

Nothing is ever finished, you just run out of time.

–Peter Jackson

On July 4, 2012, the ATLAS and CMS collaborations jointly announced their discovery of a particle matching the properties of the Higgs boson [10,11], tentatively confirming a nearly 50 year-old prediction. This was a monumental triumph for the Standard Model of particle physics and it explained the origin of the masses of all elementary particles in the Standard Model. It is currently believed that several picoseconds after the Big Bang, the universe cooled below a certain critical temperature and the Higgs field condensed into a "soup" that fills all space. Formerly massless particles, like quarks, interact with this soup thereby acquiring non-zero mass. As the universe cooled even further, quarks eventually became bound together into baryons, such as the proton and neutron (collectively known as "nucleons"), a phenomenon known as confinement. The Higgs mechanism for mass generation explains the ≈ 5 MeV mass [9] of up and down quarks. The proton, which is made up of two ups and one down quark, has a mass of ≈ 940 MeV [9]. Thus, the Higgs field condensation cannot account for the overwhelming majority of the nucleon mass. Since the vast majority of the visible universe is composed of protons and neutrons, $\approx 98\%$ of the visible mass in the universe is unexplained by the Higgs field. From whence does this "extra" mass originate?

The answer to this question lies under the purview of Quantum ChromoDynamics [12, 13] (QCD). QCD is widely believed to be the correct theory to describe the "strong" nuclear force. This force, mediated by particles known as gluons, is responsible for tightly binding quarks together into protons. The origin of the "extra"

nucleon mass is believed to come from what is known as "chiral symmetry." This is a symmetry displayed in the fundamental equation describing QCD. However, this symmetry is not displayed in the everyday universe around us, and is therefore a "broken" symmetry. An example of this broken symmetry lies in the masses of two subatomic particles, the ρ and a_1 mesons. If chiral symmetry was realized in nature, then these two particles would have the same mass, However, the a_1 is $\approx 60\%$ more massive than the ρ. This mass difference is generated by the breaking of chiral symmetry, which is also the source of the "extra" mass found in nucleons.

Another peculiar aspect of the strong nuclear force is that, as the momentum transfer between interacting quarks *increases*, the strength of the strong force *decreases*. Therefore, if we sufficiently heat up nucleons, eventually the energy their constituent quarks acquire from the heat would be so great that the strong force would no longer be strong enough to bind them together. At this point, protons and neutrons would melt away leaving only quarks and gluons which are no longer confined within the nucleons. Thus, matter undergoes a transition into a state known as quark-gluon plasma (QGP). In addition to this phenomenon of "deconfinement," it is also believed that the extra mass generated by the breaking of chiral symmetry melts away with increasing temperature, indicating the gradual restoration of chiral symmetry. The QGP is believed to have been the state of the universe when it was between approximately 10^{-12} to 10^{-6} seconds old.

The temperature required to attain a quark-gluon plasma is approximately 4 trillion degrees Fahrenheit. There is no known condition in the known universe where this environment naturally occurs. Not even the most extreme phenomena such as black holes nor supernova attain such temperatures. This does, however, occur in Brookhaven, New York and Geneva, Switzerland. The former is the home to the Relativistic Heavy Ion Collider (RHIC) and the latter is home to the Large

Hadron Collider (LHC). At both facilities, experiments are conducted where heavy ions, such as gold or lead nuclei, are slammed together at speeds in excess of 99.9999% the speed of light. These collisions result in a fireball where sufficient temperatures are attained to create the QGP. Luckily for humanity, these fireballs are only a few hundredths of a trillionth of a meter across, and only last for a handful of billionths of a second. These fireballs very rapidly cool, so that the QGP disappears and the only particles that reach the detectors of experiments are those with very long lifetimes ("long" in terms of strong-force interaction physics). By the time these particles are emitted, they have "thermalized." That is, they have interacted with each other in the fireball so much that they lose much information they were been carrying from the fireball itself. The question is then, how do we glean information about matter in these extreme conditions from this fireball? For that matter, how do we even know how hot it gets?

One answer is, "look" at it. Not as in seeing light with eyes, but by using experimental instruments to detect photons. Since photons do not interact via the strong nuclear force, they can pass almost unhindered through the fireball. We can estimate this effect by looking at the elastic mean free path of particles. In the simplest possible elastic photon scattering process there are two electromagnetic (EM) vertices, which together pick up one power of the electromagnetic coupling constant α_{EM}. Similarly, a tree-level quark and/or gluon scattering process picks up one power of the strong coupling constant, α_s. An interaction cross section involves effectively squaring the tree level process, so the cross section is proportional to the squared coupling constant. The mean free path of a particle is inversely proportional to its interaction cross section. Using the canonical value for the EM coupling constant of $\alpha_{\mathrm{EM}} = 1/137 \approx 1/100$ and using a very rough estimate of the strong coupling constant in the fireball of $\alpha_s \approx 1$, the ratio of their elastic mean

free paths is $\alpha_{EM}^2/\alpha_s^2 \approx 10,000$. Therefore, a photon is 10,000 times less likely to rescatter on its way through the QGP than a quark. Since matter in the fireballs of heavy-ion collisions continuously emit photons, they serve as an excellent probe of all stages of the fireball evolution.

In heavy-ion collisions, when the collision geometry is non-central, i.e., the nuclei "clip" one another instead of colliding head on, the parts of the nuclei that did not collide quickly move away from the central matter, leaving an almond-shaped blob of impacted matter. Over the progression of the fireball lifetime, this initial spatial anisotropy is converted to a momentum anisotropy whereby particles moving along the minor axis of the collision zone have a greater momentum than particles moving along the major axis. This is known as elliptic flow, v_2, and can be experimentally measured in heavy-ion collisions. By measuring the relative flow of particles, one can possibly glean such information as the shear viscosity, pressure, temperature, and even electrical conductivity of the fireball matter.

The goal of this work is to examine the properties of strongly-interacting matter in temperature ranges cooler than the QGP transition temperature. To do so, we analyze the behavior of the vector current-current correlator, Π_V. We first analyze the behavior of the isovector vector and axial-vector correlators as temperatures gradually rise towards the QGP phase transition temperature. As these particles associated with these correlators (viz. the ρ and a_1 mesons) heat up and slowly start to melt, their properties are expected to gradually change and become degenerate, signaling the restoration of chiral symmetry. We analyze these changes using a quantum field theoretic construct known as sum rules. We then proceed to calculate contributions to photon emission rates from the latter stages of fireball evolution by taking the zero-mass limit of the vector correlator. We then directly relate the vector correlator to the electromagnetic correlator, thereby allowing us to calculate thermal

photon emission rates by analyzing finite-temperature properties of photons. These photon emission rates can be used to glean information about the strongly-interacting matter from which these photons originate.

2. FINITE-TEMPERATURE QCD SUM RULES

The spontaneous breaking and ultimate restoration of chiral symmetry induces observable changes in the hadron spectrum, particularly among chiral partners. Were chiral symmetry to be unbroken in the QCD vacuum, all chiral multiplets, specifically their masses and widths, would remain unchanged under a rotation in chiral space. However, the QCD ground state spectrum does not display this symmetry. This is particularly evident in the large mass splitting between the isovector $\rho(770)$ and $a_1(1260)$ mesons.

Chiral symmetry is believed to be restored at high temperatures and/or baryon densities [14,15]. Its breaking and restoration can be described by an order parameter whose value is zero when the symmetry is restored and non-zero when the symmetry is broken. For the chiral phase transition of QCD, the typical order parameter is the expectation value of the quark condensate, $\langle 0|\bar{q}q|0\rangle$. It is believed that the chiral phase transition at finite temperature and small baryon chemical potential is neither first- nor second-order, but a crossover transition [15]. Therefore, the quark condensate is expected to smoothly "melt" with increasing temperature until chiral symmetry is restored, a prediction that has been confirmed by first-principle lattice QCD computations [16, 17]. The gradual melting of the quark condensate should then be accompanied by an approach towards degeneracy in ρ and a_1 masses, or more generally, the spectral distributions of the isovector-vector (ρ) and isovector-axial-vector (a_1) channels.

This temperature-dependent interplay of spectral functions can be analyzed non-perturbatively by the use of finite-temperature sum rules. Sum rules relate the spectral distribution of a particular channel to an expansion in powers of inverse

momenta which is expressed in low-energy condensates. The sum rules pertinent to the current work are the finite-temperature versions of the QCD sum rules (QCDSRs [18, 19]) and the Weinberg-type sum rules (WSRs) [20–22]. The QCDSRs are channel-specific; one such sum rule exists for each of the vector and axial-vector channels. The WSRs relate moments of the difference in vector and axial-vector spectral functions to various chiral order parameters.

At low temperatures, the thermal medium can be modeled as a gas of non-interacting pions [23]. In Ref. [24] it was found that, to leading order in temperature, this gas results in a linear mixing of the vacuum vector and axial-vector spectral functions. This model-independent "chiral mixing" is the result of thermal pion exchange between the two channels [25–27]. There it was also found that chiral mixing straightforwardly satisfies the finite-temperature WSRs.

Many previous works [28–34] that explored the QCDSRs in the context of chiral mixing have used a spectral function ansatz of a single resonance together with a perturbative continuum modeled by a sharp onset (i.e., Heaviside function) at some energy threshold s_0, following the original works in 1979 [18, 19]. However, those same works labeled this a "rough model" and "...it is in fact for the first time that we can test QCD beyond mere perturbation theory, and a rough model is preferable for a quantitative analysis." [19] Thus, the usage of such a schematic model was acceptable simply because this was a first attempt at the application of the QCDSRs. Additionally, regarding the usage of the sharp-onset continuum [19]:

> "It is worth noting that introducing the dimensionful parameter s_0... through the continuum model is in fact unsatisfactory. It might make a false impression that the sum rules just relate the ρ mass to s_0 introduced by hand and that is all. In fact, we can consider s_0 as a fit parameter

and find it from the sum rules themselves."

Therefore, the authors themselves realized that such sharp-onset a continuum model was unsatisfactory, but suitable for a first attempt at application of the sum rules.

The application of the above spectral function model to finite-temperature sum rules raises further questions. Should the threshold move as a function of temperature? If so, what should be its temperature dependence? Even when moving beyond a delta-function resonance with finite-width spectral distributions, it was found that the axial-vector channel did not satisfy the vacuum QCDSRs [35]. In addition, if the threshold moves with temperature and is treated as a fit parameter, the location of the threshold moves lower in energy with increasing temperature, and actually "consumes" the resonance in the spectral function [36].

In the context of chiral mixing, the threshold for each channel must remain fixed to its vacuum value since the finite-temperature spectral functions are linear combinations of the vacuum spectral functions. Even this presents an ambiguity: if the thresholds for the vector and axial-vector channels differ, then chiral mixing will induce a mixing between perturbative (continuum) and non-perturbative (resonance) structures. If the two regimes are, by definition, separate, what then does mixing them mean? The above questions suggest that the spectral function model of delta function and sharp-onset continuum may be too crude for a clear application within the QCDSRs. This suggests the usage of a more advanced model[1].

Such a model was constructed in Ref. [1]. The vector and axial-vector spectral functions from that work are shown in Fig. 2.1. They contain three features which prove to be important to the current work: a ground state resonance (the ρ and

[1]In the context of this work, the author found that, when using a spectral function model composed of a single ρ resonance together with a smooth-onset continuum which agreed with ALEPH data, he was unable to satisfy the vacuum QCDSR in the vector channel. However, when altering the spectral function to include the second resonance region visible in the ALEPH data (see Fig. 2.1), the vacuum QCDSR was well satisfied.

a_1), an excited state (ρ' and a_1'), and a smooth degenerate continuum. The spectral functions were constructed to satisfy τ decay data from the ALEPH collaboration [37] as well as the vacuum Weinberg-type sum rules, where near-perfect agreement was achieved. Most previous data-based WSR analyses of the τ decay data set the upper limit of the energy integration range at the τ mass [37–39]. However, at this energy the WSRs still display oscillatory behavior and are not yet convergent. The work of Ref. [1] overcame this limitation by extending the energy integration range from the τ mass to infinity and including an a_1' excited state, which compliments the ρ' state evident in the ALEPH data.

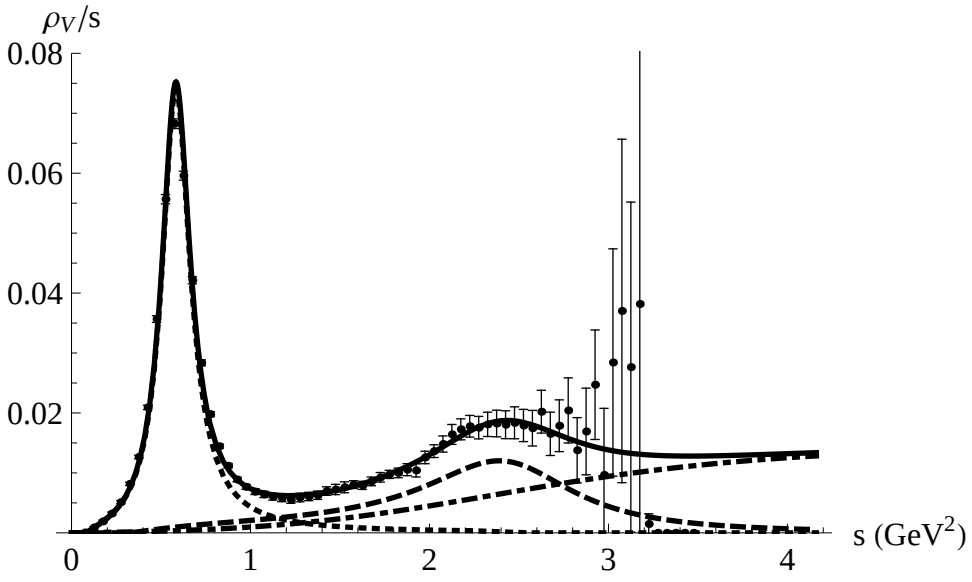

(a) Vector channel

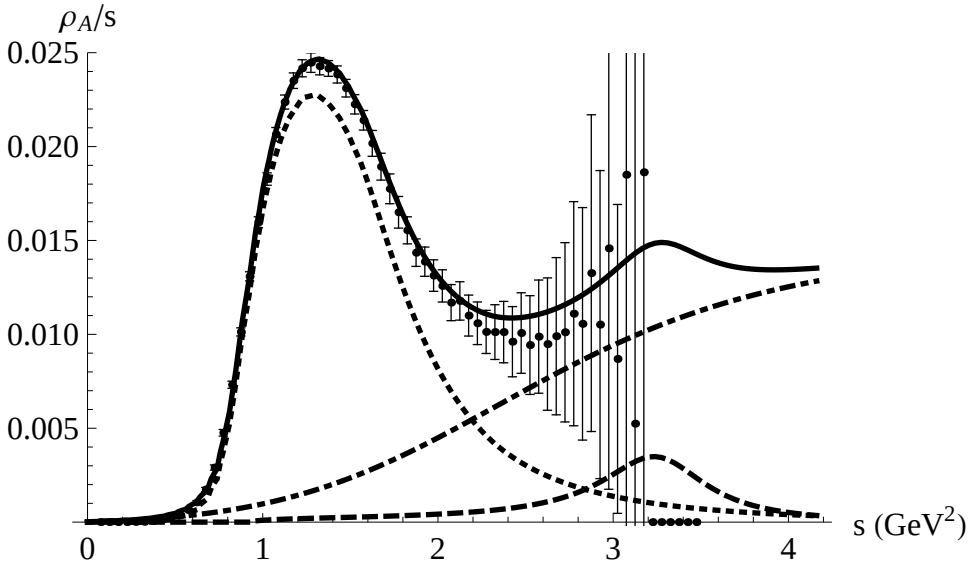

(b) Axial-vector channel

Figure 2.1: Vacuum vector and axial-vector spectral functions compared with ALEPH τ-decay data.

The agreement of these vacuum spectral functions with both the WSRs and QCDSRs suggests using them in an updated analysis of the finite-temperature sum rules. In this chapter we present and apply the finite-temperature QCDSRs and WSRs. We additionally employ a finite pion mass instead of working in the chiral limit of $m_\pi \to 0$, a feature which turns out to be pivotal in our analysis.

The remainder of this chapter is organized as follows. We first present the vacuum sum rules, then their finite-temperature counterparts. We then construct the finite-temperature spectral functions within the context of chiral mixing. Next, we apply the resulting spectral functions to both the finite-temperature WSRs and QCDSRs and evaluate the results. Finally, we summarize our findings.

2.1 Vacuum Sum Rules

Here we outline the derivations of the QCD and Weinberg sum rules in vacuum. Complete derivations can be found in Refs. [18–22].

2.1.1 QCD Sum Rule

We begin with the vector or axial-vector current-current correlator,

$$\Pi_{\mu\nu}(q) = i \int d^4x \, e^{iq\cdot x} \, \langle 0 | \mathcal{T} \left\{ j_\mu(x) j_\nu(0) \right\} | 0 \rangle \, . \tag{2.1}$$

This can be interpreted as the amplitude to propagate the current j_μ with the given quantum numbers from $x = 0$ to a variable location x. Here the currents have been time-ordered in the standard fashion, such that

$$\mathcal{T} \left\{ j_\mu(x,t_1) j_\nu(x,t_2) \right\} \equiv \Theta(t_1 - t_2) j_\mu(x,t_1) j_\nu(x,t_2) + \Theta(t_2 - t_1) j_\nu(x,t_2) j_\mu(x,t_1) \, , \tag{2.2}$$

where $\Theta(t)$ is the Heaviside step function. The currents are constructed of combinations of quark fields which yield the quantum numbers of the hadronic channel under study. For the present work we focus on the isovector-vector and isovector-axial-vector currents

$$j_\mu^V = \frac{1}{2}\left(\bar{u}\gamma_\mu u - \bar{d}\gamma_\mu d\right), \tag{2.3}$$

$$j_\mu^A = \frac{1}{2}\left(\bar{u}\gamma_\mu\gamma_5 u - \bar{d}\gamma_\mu\gamma_5 d\right), \tag{2.4}$$

where we have suppressed isospin indices for clarity and simplicity. The lowest-lying resonances in each of the vector and axial-vector channels (save for the pion in the axial-vector channel, which is "special" due to its Goldstone boson nature), are the ρ and a_1 mesons, respectively.

The current-current correlators can be decomposed into four-dimensional transverse and longitudinal parts,

$$\Pi_{\mu\nu}^{V,A} = \left(-g_{\mu\nu} + \frac{q_\mu q_\nu}{q^2}\right)\Pi_T^{V,A} + \frac{q_\mu q_\nu}{q^2}\Pi_L^{V,A}, \tag{2.5}$$

where q_μ is the four-momentum of the resonant state under study. In vacuum the longitudinal part of the vector correlator vanishes due to conservation of vector current. However, the conservation of the axial-vector current is broken by the finite pion mass, which is embodied in the partial conservation of axial-vector current (PCAC): the axial-vector current is not conserved, but its violation is only of order m_π^2. PCAC takes the explicit form [40, 41]

$$\left\langle 0|\partial_\mu j_\mu^A(x)|\pi\right\rangle = \frac{f_\pi\, m_\pi^2\, e^{iq\cdot x}}{\sqrt{2E_\pi}}, \tag{2.6}$$

where $f_\pi = 92.4$ MeV is the pion leptonic decay constant [9]. This violation of current conservation causes the longitudinal vacuum axial-vector correlator to pick up an "extra" part in the form of the pion pole,

$$\mathrm{Im}\,\Pi_L^A(q^2) = -\pi f_\pi^2\, q^2\, \delta(q^2 - m_\pi^2)\,. \tag{2.7}$$

In medium the pion acquires a self-energy which effectively smears out the δ-function representing its mass distribution.

The current-current correlators may also be expressed in terms of spectral functions, which we denote by the symbol ρ, by using the Källen-Lehmann spectral representation,

$$\Pi(q^2) = \int_0^\infty ds \frac{\rho(s)}{s - q^2 - i\epsilon}\,. \tag{2.8}$$

The explicit expression for the spectral function is

$$\rho(q^2) = -\frac{1}{\pi}\,\mathrm{Im}\,\Pi(q^2)\,. \tag{2.9}$$

The dispersion relation of Eq. (2.8) includes subtractions;

$$\frac{\Pi(q^2) - \Pi(0)}{q^2} = \frac{1}{\pi}\int \frac{ds}{s - q^2 - i\epsilon}\mathrm{Im}\left(\frac{\Pi(s) - \Pi(0)}{s}\right)\,. \tag{2.10}$$

Since $\mathrm{Im}\,\Pi(0) = 0$, this yields

$$\Pi(q^2) = \Pi(0) + \frac{q^2}{\pi}\int \frac{ds}{s}\frac{\mathrm{Im}\,\Pi(s)}{s - q^2 - i\epsilon}\,. \tag{2.11}$$

Repeating the subtraction procedure, we find

$$\Pi(q^2) = \Pi(0) + q^2\Pi'(0) + \frac{q^4}{\pi}\int \frac{ds}{s^2}\frac{\mathrm{Im}\,\Pi(s)}{s - q^2 - i\epsilon}\,. \tag{2.12}$$

In vacuum both $\Pi(0)$ and $\Pi'(0)$ vanish. We thus have a representation of the current-current correlator in a hadronic basis—as resonances encoded in the spectral functions of the vector and axial-vector channels.

The correlator may also be expressed in a quark basis, owing to the principle of quark-hadron duality [42]. The correlator can be evaluated using perturbative QCD when the four-momentum is large and negative; $-q^2 = Q^2$. Using Wilson's operator product expansion (OPE) [43–45], the correlator can be expanded as

$$\Pi(Q^2) = \sum_n C_n(Q^2, \mu) \langle 0|\mathcal{O}_n(\mu)|0\rangle \ , \tag{2.13}$$

where the C_n terms are complex-valued coefficients (Wilson coefficients), the $\mathcal{O}_n$ are local operators composed of quark and gluon fields, and μ is an arbitrary energy/momentum normalization point. The physics from momenta greater than μ is encoded in the Wilson coefficients, and physics from momenta less than μ is absorbed into the local operators, allowing an unambiguous application of the OPE [46]. The Wilson coefficients can be calculated via QCD perturbation theory, see, e.g., Refs [18, 19, 46]. The resulting vacuum expectation values of the local operators are known as "condensates," signifying the non-trivial propagation/coupling of quarks and gluons in and to the physical QCD vacuum.

Our general QCD sum rule is now given by equating Eqs. (2.12) and (2.13). Various integral transforms may be performed to improve series convergence; we focus on the Borel transform of a function $f(x)$, defined by [18]

$$\tilde{f}(M) = \frac{1}{2\pi i} \int_{c-i\infty}^{c+i\infty} e^{-M/x} f(x)\, d\left(\frac{1}{x}\right), \tag{2.14}$$

where the integration contour c is to the right of all singularities in $f(x)$. The Borel

transform may also be expressed in a derivative operator form,

$$\hat{L}_{\mathcal{M}} = \lim_{Q^2\to\infty, n\to\infty, Q^2/n=\mathcal{M}^2} \frac{1}{(n-1)!} \left(Q^2\right)^n \left(-\frac{d}{dQ^2}\right)^n . \tag{2.15}$$

When applied to a polynomial, this transform gives

$$\hat{L}_{\mathcal{M}} \left[\frac{1}{Q^{2k}}\right] = \frac{1}{(k-1)!} \left(\frac{1}{\mathcal{M}^{2k}}\right) . \tag{2.16}$$

Thus, when applied to the OPE of Eq. (2.13), the Borel transform results in a factorial suppression of higher-order terms as a result of Eq. (2.15). Additionally, when the Borel transform is applied to Eq. (2.12), it exponentially suppresses the higher resonant states in the spectral function. Applying the Borel transform to both Eqs. (2.12) and (2.13) and equating the two yields the usual QCD sum rule:

$$\frac{1}{\mathcal{M}^2} \int \frac{\rho(s)}{s} e^{-s/\mathcal{M}^2} ds = C_0 + \frac{C_1}{\mathcal{M}^2} + \frac{C_2}{\mathcal{M}^4} + \frac{C_3}{\mathcal{M}^6} . \tag{2.17}$$

The left-hand side (LHS) essentially contains information on the low-lying hadronic resonances, while the right-hand side (RHS) encodes quark and gluon physics in the form of condensates and Wilson coefficients. As a result of the Borel transform, the four-momentum Q has been replaced by the "Borel mass," $\mathcal{M}$, which is treated as a parameter. The C_n coefficients contain both numerical factors and condensates whose energy dimension matches that of the Borel mass in the denominator, as both sides of Eq. (2.17) are dimensionless. We truncate the OPE at dimension 6 due to the factorial suppression of higher-dimensional terms. We then assume convergence of the sum rules and evaluate the uncertainty in our results.

The resulting values for C_n in the vector and axial-vector channels [18, 19] read:

$$\begin{aligned} C_0^V = C_0^A &= \frac{1}{8\pi^2}\left(1+\frac{\alpha_s}{\pi}\right) , \\ C_1^V = C_1^A &= -\frac{3}{8}(m_u^2+m_d^2) \approx 0 , \\ C_2^V = C_2^A &= \frac{1}{24}\langle\frac{\alpha_s}{\pi}G^a_{\mu\nu}G^a_{\mu\nu}\rangle + \langle m_u\bar{u}u + m_d\bar{d}d\rangle , \\ C_3^V &= -\frac{56}{81}\pi\alpha_s\langle\mathcal{O}_4^V\rangle , \\ C_3^A &= \frac{88}{81}\pi\alpha_s\langle\mathcal{O}_4^A\rangle . \end{aligned} \tag{2.18}$$

Here all expectation values are taken over vacuum states; $\langle\mathcal{O}\rangle = \langle 0|\mathcal{O}|0\rangle$. In principle there exists a dimension-6 gluon condensate in C_3^V and C_3^A which we have not listed, $\left\langle f_{abc}G^a_{\mu\nu}G^b_{\nu\lambda}G^c_{\lambda\mu}\right\rangle$ (where f_{abc} are the $SU(3)$ structure constants). However, contributions from condensates with more than two gluon field strength operators are known to be suppressed relative to the other OPE terms [47–49]. Therefore we neglect this condensate in the present work, a convention which was followed by the original and many subsequent works [1, 28, 29, 32–35, 46, 48].

In Eq. (2.18) α_s is the strong coupling constant, m_u and m_d are the up and down current quark masses whose small size ($m_u \approx m_d \approx 5$ MeV) renders $C_1^{V/A}$ negligible relative to the other terms, and $\left\langle\frac{\alpha_s}{\pi}G^a_{\mu\nu}G^a_{\mu\nu}\right\rangle$ is the lowest possible dimension gluon condensate, which we refer to as "the" gluon condensate. The (lowest possible dimension) quark condensate $\left\langle m_u\bar{u}u + m_d\bar{d}d\right\rangle$ can be simplified by using the average current quark mass $m_q = \frac{1}{2}(m_u+m_d)$ and by using isospin symmetry to equate the up and down quark condensates, so that $\left\langle m_u\bar{u}u + m_d\bar{d}d\right\rangle = m_q\,\langle\bar{q}q\rangle$. The subscript 4 in the condensates appearing in the C_3 terms indicates that the quark content involves four fields; we refer to these as the four-quark condensates. The explicit quark field content in the vector and axial-vector four-quark condensates is given by

the expressions [19, 35]

$$\begin{aligned}
\left\langle \mathcal{O}_4^V \right\rangle &= \frac{81}{224} \left\langle \left(\bar{u}\gamma_\mu\gamma_5\lambda^a u - \bar{d}\gamma_\mu\gamma_5\lambda^a d \right)^2 \right\rangle + \frac{9}{112} \left\langle \left(\bar{u}\gamma_\mu\lambda^a u + \bar{d}\gamma_\mu\lambda^a d \right) \sum_{\psi=u,d,s} \bar{\psi}\gamma^\mu\lambda^a\psi \right\rangle , \\
\left\langle \mathcal{O}_4^A \right\rangle &= -\frac{81}{352} \left\langle \left(\bar{u}\gamma_\mu\lambda^a u - \bar{d}\gamma_\mu\lambda^a d \right)^2 \right\rangle - \frac{9}{176} \left\langle \left(\bar{u}\gamma_\mu\lambda^a u + \bar{d}\gamma_\mu\lambda^a d \right) \sum_{\psi=u,d,s} \bar{\psi}\gamma^\mu\lambda^a\psi \right\rangle .
\end{aligned} \tag{2.19}$$

Here the λ^a matrices are the Gell-Mann matrices, which are (up to an arbitrary normalization factor) the generators of the Lie algebra of the $SU(3)$ color symmetry group.

The four-quark condensates can be substantially simplified by using the factorization hypothesis, which states that the vacuum intermediate state in all channels is dominant, and that all higher states can be neglected. This results in the following simplification:

$$\langle \bar{q}\Gamma_1 q \bar{q}\Gamma_2 q \rangle = N^{-2} \left[\left(\operatorname{Tr}\Gamma_1 \operatorname{Tr}\Gamma_2 \right) - \operatorname{Tr}\left(\Gamma_1\Gamma_2 \right) \right] \langle \bar{q}q \rangle^2 , \tag{2.20}$$

where the Γ terms represent the matrix structure between the quark field operators. N is a normalization constant defined by the relation

$$\langle \bar{q}_A q_B \rangle = \frac{\delta_{AB}}{N} \langle \bar{q}q \rangle , \tag{2.21}$$

and the subscripts A, B stand for a combination of spin, color, and flavor indices. For the vector and axial-vector four-quark condensates, the numerical prefactor turns out to be unity. We additionally add a parameter $\kappa > 1$ to account for the violation of the factorization hypothesis, i.e., the contribution from the other states. We then

have

$$\left\langle \mathcal{O}_4^V \right\rangle = \kappa_V \left\langle \bar{q}q \right\rangle^2$$
$$\left\langle \mathcal{O}_4^A \right\rangle = \kappa_A \left\langle \bar{q}q \right\rangle^2 . \tag{2.22}$$

In principle, the values of κ_V and κ_A need not be identical, as the vector and axial-vector four-quark condensates are not the same. We note that all condensates appearing at zero temperature are Lorentz scalars, as they must be to ensure Lorentz invariance of the vacuum state.

2.1.2 Weinberg-Type Sum Rules

The Weinberg-type sum rules relate the moments of the difference between vector and axial-vector spectral functions to various order parameters of chiral symmetry breaking. The full derivations of the Weinberg-type sum rules can be found in the original works [20–22] and in Ref. [50]. The Weinberg-type sum rules take the general form

$$\int_0^\infty \frac{ds}{s^2}\, s^n \left[\rho_V(s) - \rho_A(s)\right] = f_n \,, \tag{2.23}$$

where the f_n represent various order parameters of spontaneous chiral symmetry breaking. Sum rules are known for $n = 0, 1, 2$, and 3. They are, in order of increasing n:

$$\text{(WSR-0)} \qquad \int_0^\infty \frac{ds}{s^2}\, \left[\rho_V(s) - \rho_A(s)\right] = \frac{1}{3} f_\pi^2 \left\langle r_\pi^2 \right\rangle - F_A \,, \tag{2.24}$$

$$\text{(WSR-1)} \qquad \int_0^\infty \frac{ds}{s}\, \left[\rho_V(s) - \rho_A(s)\right] = f_\pi^2 \,, \tag{2.25}$$

$$\text{(WSR-2)} \qquad \int_0^\infty ds\, \left[\rho_V(s) - \rho_A(s)\right] = f_\pi^2 m_\pi^2 \,, \tag{2.26}$$

$$\text{(WSR-3)} \qquad \int_0^\infty ds\, s\, \left[\rho_V(s) - \rho_A(s)\right] = -2\pi\alpha_s \left\langle \mathcal{O}_4^{SB} \right\rangle \,. \tag{2.27}$$

We label the first listed sum rule as number zero since it was discovered after the original Weinberg sum rules (WSR-1 and -2). Here $F_A = 0.0058$ is the pion radiative decay constant and $\langle r_\pi^2 \rangle = 0.439$ fm^2 is the average squared pion charge radius. In Eq. (2.27), $\left\langle \mathcal{O}_4^{SB} \right\rangle$ is the chiral symmetry-breaking combination of the vector and axial-vector condensates, and is given by [1]

$$\begin{aligned} \left\langle \mathcal{O}_4^{SB} \right\rangle &= \frac{16}{9}\left(\frac{7}{18}\left\langle \mathcal{O}_4^{V} \right\rangle + \frac{11}{18}\left\langle \mathcal{O}_4^{A} \right\rangle\right) \\ &= \frac{1}{4}\left\langle \left(\bar{u}\gamma_\mu\gamma_5\lambda^a u - \bar{d}\gamma_\mu\gamma_5\lambda^a d\right)^2 - \left(\bar{u}\gamma_\mu\lambda^a u - \bar{d}\gamma_\mu\lambda^a d\right)^2 \right\rangle . \end{aligned} \tag{2.28}$$

This condensate also may be factorized in the same manner as Eq. (2.22):

$$\left\langle \mathcal{O}_4^{V} \right\rangle = \frac{16}{9}\left(\frac{7}{18}\kappa_V + \frac{11}{18}\kappa_A\right)\langle \bar{q}q \rangle^2 . \tag{2.29}$$

2.2 Finite-Temperature Sum Rules

2.2.1 QCD Sum Rules at Finite Temperature

At finite temperatures, Lorentz invariance is broken due to the presence of a thermal rest frame. By considering the mesons (or, alternately, their associated currents) under study to be at rest relative to the thermal frame, the condensates retain a dependence only on temperature. The broken Lorentz invariance also necessitates the introduction of new, non-scalar condensates in the C_2 and C_3 terms. These new operators are typically characterized by the difference between their energy dimension and their spin, known as "twist," τ. Additionally, the expectation value must now be taken with respect to the thermal medium instead of the vacuum state. The

new, thermal OPE terms are then [29]

$$\begin{aligned} C_2^V(T) = C_2^A(T) &= \frac{1}{24}\langle\frac{\alpha_s}{\pi}G^a_{\mu\nu}G^a_{\mu\nu}\rangle_T + m_q\langle\bar{q}q\rangle_T + \left\langle\mathcal{O}^{\tau=2,s=2}\right\rangle_T \ , \\ C_3^V(T) &= -\frac{56}{81}\pi\alpha_s\langle\mathcal{O}_4^V\rangle_T + \left\langle\mathcal{O}^{\tau=2,s=4}\right\rangle_T + \left\langle\mathcal{O}^{\tau=4,s=2}\right\rangle_T \ , \\ C_3^A &= \frac{88}{81}\pi\alpha_s\langle\mathcal{O}_4^A\rangle_T + \left\langle\mathcal{O}^{\tau=2,s=4}\right\rangle_T + \left\langle\mathcal{O}^{\tau=4,s=2}\right\rangle_T \ . \end{aligned} \tag{2.30}$$

The temperature dependence of the OPE resides in the condensates, as the Wilson coefficients are temperature independent as a result of the separation of energy scales [28].

In the present work we focus on the leading-order temperature dependence of the QCD and Weinberg-type sum rules. We then need an expansion parameter that we require to be "small." Our setting contains three inherent energy scales: m_π, T, and Λ, where Λ is a typical hadronic energy scale of order $\mathcal{O}[1\,\mathrm{GeV}]$. We then have two expansion parameters, m_π/Λ and T/Λ (the possibility of m_π/T is addressed below.). The temperature regime pertaining to the current work is $T \lesssim m_\pi$, which leaves us with one effective parameter

$$\lambda = \frac{T}{\Lambda} \lesssim \frac{m_\pi}{\Lambda}\,. \tag{2.31}$$

Our consistent finite-temperature treatment of the QCD and Weinberg-type sum rules is then satisfied by working to leading order in λ.

Evaluation of the leading-order temperature dependence of the condensates is carried out by modeling the thermal medium as a dilute gas of non-interacting pions, which is a valid approximation for $T \lesssim m_\pi$ where the mean distance between pions suppresses their interaction [29, 51, 52]. One then integrates the expectation value of

the relevant operator over one-pion states, folded with the thermal Bose distribution:

$$\langle \mathcal{O} \rangle_T \approx \langle \mathcal{O} \rangle_0 + 3 \int \frac{d^3k}{(2\pi)^3 E_\pi} f^\pi(E_\pi, T) \left\langle \pi(\vec{k}) | \mathcal{O} | \pi(\vec{k}) \right\rangle , \tag{2.32}$$

where $E_\pi = \sqrt{\vec{k}^2 + m_\pi^2}$ is the pion energy in the thermal rest frame and $f^\pi = [\exp(E_\pi/T) - 1]^{-1}$ is the pion's Bose distribution function. The numerical prefactor 3 is a result of summing the over isospin states of the pion.

These integrals were carried out in Refs. [28, 29]. The integrals involving scalar condensates may be evaluated using vector and axial-vector current algebra together with the soft pion theorem, which relates transition matrix elements between single pion states with vanishingly small momentum to matrix amplitudes between vacuum states [29];

$$\lim_{\vec{p} \to 0} \langle \pi^a(\vec{p}) | \mathcal{O} | 0 \rangle = -\frac{i}{f_\pi} \langle 0 | [Q_5^a, \mathcal{O}] | 0 \rangle , \tag{2.33}$$

Where Q_5^a is the isovector axial charge of the pion, given by

$$Q_5^a = \int d^3x \, \bar{q}(x) \gamma_0 \gamma_5 \frac{\tau^a}{2} q(x) . \tag{2.34}$$

The $q(x)$ are the light-quark fields and τ^a is the Pauli matrix in isospin space.

The resulting temperature dependence of a scalar operator is then contained solely in the dimensionless quantity

$$\epsilon(T) = \frac{2}{f_\pi^2} \int_0^\infty \frac{d^3k}{(2\pi)^3 E_\pi} f^\pi(E_\pi, T) . \tag{2.35}$$

In the chiral limit of $m_\pi \to 0$ this expression reduces to $T^2/(6f_\pi^2)$. However, in this work we are concerned with the effects from a finite pion mass, so we retain the full expression for $\epsilon(T)$ above. The leading-order temperature dependencies of the scalar

condensates listed in Eq. (2.18) are [23, 29]:

$$\begin{aligned}
\langle \bar{q}q \rangle_T &= \langle \bar{q}q \rangle_0 \left(1 - \frac{3}{4}\epsilon(T) \right) , \\
\left\langle \frac{\alpha_s}{\pi} G^a_{\mu\nu} G^a_{\mu\nu} \right\rangle_T &= \left\langle \frac{\alpha_s}{\pi} G^a_{\mu\nu} G^a_{\mu\nu} \right\rangle_0 - \frac{2}{3} m_\pi^2 f_\pi^2 \epsilon(T) , \\
\left\langle \mathcal{O}_4^V \right\rangle_T &= \kappa_V \langle \bar{q}q \rangle_0^2 \left(1 - \frac{18}{7} \frac{\kappa}{\kappa_V} \epsilon(T) \right) , \\
\left\langle \mathcal{O}_4^A \right\rangle_T &= \kappa_A \langle \bar{q}q \rangle_0^2 \left(1 - \frac{18}{11} \frac{\kappa}{\kappa_A} \epsilon(T) \right) .
\end{aligned} \tag{2.36}$$

Calculation of the temperature dependencies of the non-scalar condensates is somewhat more involved. The matrix elements of the these operators appear in deep inelastic scattering of pions, i.e., they involve the light-quark distribution functions of the pion. The operators and their temperature dependence are [29, 32, 53]:

$$\begin{aligned}
\left\langle \mathcal{O}^{\tau=2,s=2} \right\rangle_T &= A_2^\pi \left(\frac{3}{4} m_\pi^2 I_1(T) + I_2(T) \right) , \\
\left\langle \mathcal{O}^{\tau=2,s=4} \right\rangle_T &= -A_4^\pi \left(\frac{5}{8} m_\pi^4 I_1(T) + \frac{5}{2} m_\pi^2 I_2(T) + 2 I_3(T) \right) , \\
\left\langle \mathcal{O}^{\tau=4,s=2} \right\rangle_T &= -B_2^\pi \left(\frac{3}{4} m_\pi^2 I_1(T) + I_2(T) \right) ,
\end{aligned} \tag{2.37}$$

where the $I_n(T)$ are temperature-dependent integrals similar to the expression for $\epsilon(T)$:

$$I_n(T) = \int_0^\infty \frac{d^3k}{(2\pi)^3} \frac{k^{2n-2}}{E_\pi} f^\pi(E_\pi, T) . \tag{2.38}$$

The coefficients A_n^π are moments of the light quark/anti-quark pion distribution functions, given by [29]

$$A_n^\pi = 2 \int_0^1 dx\, x^{n-1} \left[q(x,\mu) + (-1)^n \bar{q}(x,\mu) \right] . \tag{2.39}$$

We adopt the values of these coefficients to be [29, 54] $A_2^\pi = 0.97$ and $A_4^\pi = 0.255$.

While experimental data on the B_2 term exist for the nucleon, similar data for the pion are not available. However, analyses using the MIT bag model estimate B_2^π to be small [55, 56]. Therefore, we will assume the value of B_2^π to be zero, and estimate the effect of possible deviations from this value as part of the uncertainty in our calculations.

Our numerical evaluation of the QCD sum rules will require a metric to quantify deviation between the spectral and OPE sides. We shall use the method introduced by the original authors [18, 19] and refined by Leinweber [48, 57, 58]. This measure uses the average deviation between the LHS and RHS of Eq. (2.17) over a finite range of the Borel mass. This measure, which we refer to as the d value, is given by

$$d = \frac{1}{\mathcal{M}^2_{\text{max}} - \mathcal{M}^2_{\text{min}}} \int_{\mathcal{M}^2_{\text{min}}}^{\mathcal{M}^2_{\text{max}}} \left| 1 - \frac{\text{LHS}(\mathcal{M}^2)}{\text{RHS}(\mathcal{M}^2)} \right| d\mathcal{M}^2 \,. \tag{2.40}$$

The minimal and maximal values of the Borel mass form a "Borel window" wherein the sum rules are considered to be valid. We choose $\mathcal{M}^2_{\text{min}}$ such that the C_3 term contributes at most 10% of the total from the OPE side, and $\mathcal{M}^2_{\text{max}}$ such that the contribution from the spectral continuum is at most 50% of the contribution from resonant states. Previous works used a limit of 100% contribution from the continuum. We use a more stringent limit due to our larger continuum threshold.

2.2.2 Weinberg-Type Sum Rules at Finite Temperature

The leading-order temperature dependence of WSR-1, -2, and -3 was derived in Ref. [22]. To the best of our knowledge, no such temperature dependence has yet been found for WSR-0. For mesons at rest relative to the thermal frame (the same condition used for the finite-temperature QCD sum rules), the finite-temperature

Weinberg-type sum rules are:

$$\begin{aligned}
&\text{(WSR-1)} \qquad \int_0^\infty \frac{ds}{s}\left[\rho_V(s,T) - \bar{\rho}_A(s,T)\right] = 0\,, \\
&\text{(WSR-2)} \qquad \int_0^\infty ds\left[\rho_V(s,T) - \bar{\rho}_A(s,T)\right] = 0\,, \\
&\text{(WSR-3)} \qquad \int_0^\infty ds\, s\,\left[\rho_V(s,T) - \bar{\rho}_A(s,T)\right] = -2\pi\alpha_s \left\langle O_4^{SB}\right\rangle_T\,. \qquad (2.41)
\end{aligned}$$

Here we introduce the notation $\bar{\rho}_A = \rho_A + f_\pi^2 s\delta(s - m_\pi^2)$ to indicate we have absorbed the pion pole contribution to the axial-vector correlator into the definition of the axial-vector spectral function. As stated earlier, at finite temperature the pion develops a self-energy. This effectively smears the δ-function in Eq. (2.7) into a spectral distribution. The pion pole can then no longer be simply integrated out of the spectral side of the WSRs and is more naturally included along with the vector and axial-vector spectral functions. The temperature dependence of the chirally-breaking four-quark condensate has been shown to be [22, 59]

$$\left\langle O_4^{SB}\right\rangle_T = \left\langle O_4^{SB}\right\rangle_0 \left[1 - 2\epsilon(T)\right]\,. \qquad (2.42)$$

Now that the leading-order temperature dependence of the sum rules has been established, we turn to the temperature dependence of the spectral function.

2.3 Finite-Temperature Spectral Function

To consistently match the leading-order temperature dependence on the RHS of the QCD sum rules, we require an equivalent temperature expansion for the vector and axial-vector spectral functions. This was derived in Ref. [59] in a model-independent manner by using precisely the same techniques used to derive the leading-order OPE temperature dependence. The correlators were evaluated in a

thermal medium of a non-interacting pion gas, and the resulting transition matrix elements were evaluated using current algebra and soft-pion theorems. The resulting leading-order in temperature spectral functions were found to be linear combinations of the vacuum spectral functions:

$$\begin{aligned}\rho_V(s,T) &= [1-\epsilon(T)]\,\rho_V(s,0) + \epsilon(T)\bar{\rho}_A(s,0)\,,\\ \bar{\rho}_A(s,T) &= [1-\epsilon(T)]\,\bar{\rho}_A(s,0) + \epsilon(T)\rho_V(s,0)\,.\end{aligned} \tag{2.43}$$

This results in the temperature dependence of the finite-temperature spectral functions residing solely in the mixing parameter $\epsilon(T)$, which is identical to that of Eq. (2.35). The two sides of the QCDSR sharing a temperature dependence governed by the same thermal parameter is reasonable, as the leading-order temperature dependence was calculated in precisely the same fashion—via a non-interacting thermal pion gas. The thermal parameter $\epsilon(T)$ induces a mixing of the vector and axial-vector spectral functions. For $\epsilon = \frac{1}{2}$ ($T \approx 215$ MeV) the finite-temperature spectral functions become degenerate, indicating restoration of chiral symmetry. However, Eq. (2.43) was obtained using current algebra, which is a low-energy effective theory. Therefore, its applicability to the high-energy perturbative part of the spectral function is questionable at best, and should not be applied to the perturbative continuum of the spectral functions.

While the above method of chiral mixing completely determines the leading-order temperature dependence of the spectral functions, it still requires vacuum spectral functions as input. As previously stated, we use the vacuum spectral functions from Ref. [1]. The parameter combinations from this work are shown in Table 2.1. These parameters resulted in d values in the vector and axial-vector channels of $d_V = 0.24\%$ and $d_A = 0.56\%$, displaying satisfactory agreement with the vacuum QCD sum rules.

Vacuum QCDSR parameters	
m_π	139.6 MeV
f_π	92.4 MeV
m_q	5 MeV
$\alpha_s(1\,\mathrm{GeV})$	0.5
$\langle r_\pi^2 \rangle$	0.439 fm^2
F_A	0.0058
$\langle \bar{q}q \rangle$	$(-0.25\,\mathrm{GeV})^3$
$\left\langle \frac{\alpha_s}{\pi} G^2 \right\rangle$	0.022 GeV^4
κ_V	2.1
κ_A	2.1

Table 2.1: List of vacuum QCD sum rule parameters.

The vacuum spectral functions were shown at the beginning of this chapter in Fig. 2.1. In both plots the contributions to the total spectral function (solid lines) are due to the ground-state resonance (dotted curve), excited resonance (dashed curve) and a universal continuum (dotted-dashed curve). These plots show how the inclusion of excited states shift the onset of the perturbative continuum to higher energies, and display the excellent agreement of the spectral functions with the ALEPH data.

We now use these vacuum spectral functions together with the chiral mixing scheme given by Eq. (2.43) to generate our finite-temperature spectral functions. The resulting finite-temperature spectral functions are shown in Fig. 2.2 for three different temperatures. The nonperturbative resonance regions of the spectral functions mix smoothly with increasing temperature. Additionally, the degenerate continua avoid any ambiguity of mixing of onset thresholds. The chirally-mixed spectral functions show an oscillatory pattern of "peaks" and "valleys" where the peaks in one channel fill in the the valleys in the other. By doing so, the spectral functions show a clear trend toward chiral restoration.

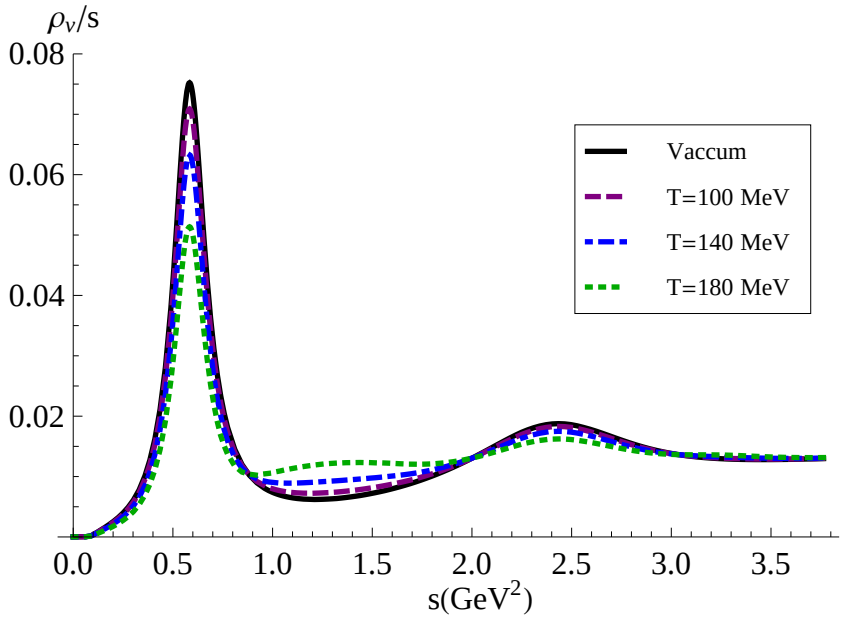

(a) Vector channel

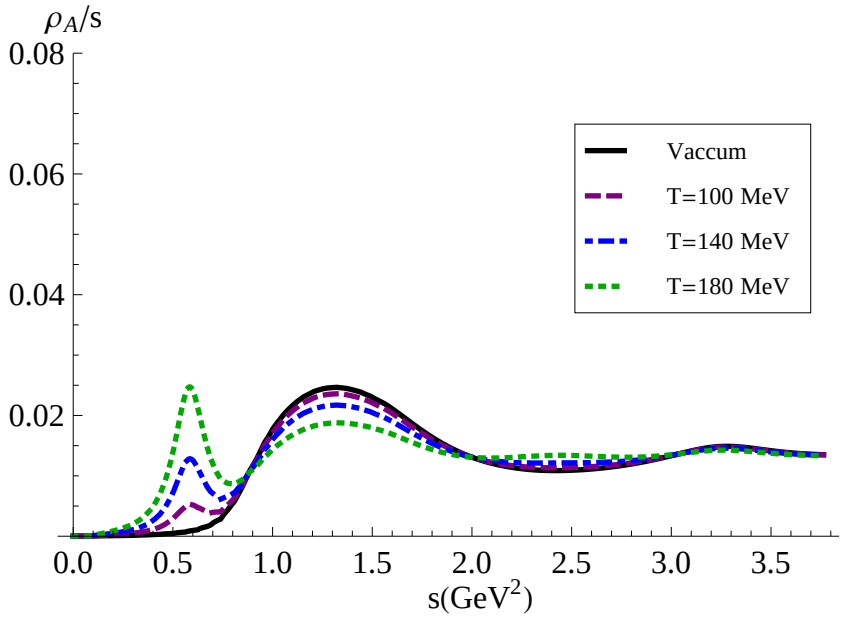

(b) Axial-vector channel

Figure 2.2: Temperature evolution of vector and axial-vector spectral functions.

2.4 Finite-Temperature Sum Rule Analysis

Having established the leading-order finite-temperature Weinberg-type and QCD sum rules, as well as our leading-order finite-temperature spectral functions, we are now ready to analytically and numerically evaluate the finite-temperature sum rules.

2.4.1 Weinberg Sum Rules with Chiral Mixing

As shown in Eq. (2.41), the temperature dependence of WSR-1 and -2 depends strictly on the difference of the finite-temperature vector and axial-vector spectral functions. This is easily evaluated within the scheme of chiral mixing, and yields

$$\begin{aligned}\rho_V(s,T) - \bar{\rho}_A(s,T) &= [1-\epsilon(T)]\,\rho_V(s,0) + \epsilon(T)\bar{\rho}_A(s,0) \\ &\quad - \{[1-\epsilon(T)]\,\bar{\rho}_A(s,0) + \epsilon(T)\rho_V(s,0)\} \\ &= [1-2\epsilon(T)]\,[\rho_V(s,0) - \bar{\rho}_A(s,0)]\ . \end{aligned} \tag{2.44}$$

The temperature dependence of the spectral functions factors outside the energy integral in the finite-temperature Weinberg sum rules in Eq. (2.41), and we immediately recover the vacuum sum rules. Thus, the finite-temperature analogs of WSR-1 and -2 are satisfied within the chiral mixing scheme if the vacuum sum rules are satisfied. Since our input vacuum spectral functions satisfy WSR-1 and -2 to a high degree of accuracy, the finite-temperature analogs of WSR-1 and -2 are automatically satisfied as well. The finite-temperature analog of WSR-3 also yields the same result, although not as trivially. When we combine the temperature dependence of the chirally-breaking four-quark condensate from Eq. (2.42) with the finite-temperature spectral functions, we find

$$[1-2\epsilon(T)]\int_0^\infty ds\, s\ [\rho_V(s,0) - \bar{\rho}_A(s,0)] = -2\pi\alpha_s \left\langle O_4^{SB}\right\rangle_0 [1-2\epsilon(T)]\ . \tag{2.45}$$

The temperature dependence of WSR-3 drops out since the leading-order temperature dependence of the spectral functions is identical to that of the chirally-breaking four-quark condensate. This again leaves us with the vacuum sum rule, which is satisfied by the vacuum spectral functions.

Thus, within the scheme of chiral mixing, the finite-temperature Weinberg-type sum rules are automatically satisfied if the corresponding vacuum sum rules are satisfied.

2.4.2 QCD Sum Rules with Chiral Mixing

2.4.2.1 Analytical Analysis

Before we proceed with the numerical evaluation of the QCD sum rules, we can use a simple approximation to analytically examine their leading-order temperature dependence. To do so, let us consider the chiral limit of $m_\pi \to 0$, so that $\epsilon(T) = T^2/(6f_\pi^2)$. Therefore, we should retain only terms with temperature dependence on the order of T^2. This automatically eliminates the non-scalar terms, since the temperature dependence of the I_n integrals in Eq. (2.38) involves powers of T greater than 2. For definiteness, we work with the vector channel, although we shall see that the results are equally applicable to the axial-vector channel. In the chiral limit the leading-order temperature dependence of the LHS is given by

$$\frac{1}{\mathcal{M}^2}\int ds \frac{\rho_V(s,0)}{s} e^{-s/\mathcal{M}^2} + \epsilon(T)\frac{1}{\mathcal{M}^2}\int ds \frac{\bar{\rho}_A(s,0)-\rho_V(s,0)}{s} e^{-s/\mathcal{M}^2}\,. \tag{2.46}$$

The second integral may be eliminated by using the vacuum QCDSRs, Eq. (2.18). Upon taking the difference between the axial-vector and vector channels only the

contribution from the four-quark condensates remains:

$$\begin{aligned}\mathrm{OPE}_A - \mathrm{OPE}_V &= \frac{\epsilon(T)}{\mathcal{M}^6}\frac{88}{81}\pi\alpha_s\left\langle O_4^A\right\rangle_0 + \frac{\epsilon(T)}{\mathcal{M}^6}\frac{56}{81}\pi\alpha_s\left\langle O_4^V\right\rangle_0 \\ &= \frac{\epsilon(T)}{\mathcal{M}^6}\pi\alpha_s\frac{16}{9}\left(\frac{7}{18}\left\langle \mathcal{O}_4^V\right\rangle_0 + \frac{11}{18}\left\langle \mathcal{O}_4^A\right\rangle_0\right) \\ &= \frac{\epsilon(T)}{\mathcal{M}^6}\pi\alpha_s\left\langle \mathcal{O}_4^{SB}\right\rangle_0 , \end{aligned} \tag{2.47}$$

where we have used the definition of the chiral symmetry-breaking four-quark condensate, Eq. (2.28), in the last line. The left-hand side of the vector QCDSR is then

$$\mathrm{LHS} = \frac{1}{\mathcal{M}^2}\int \frac{\rho_V(s,0)}{s}e^{-s/\mathcal{M}^2} + \frac{\epsilon(T)}{\mathcal{M}^6}\pi\alpha_s\left\langle \mathcal{O}_4^{SB}\right\rangle_0 . \tag{2.48}$$

We now turn to the right-hand side of the sum rule. Since we are now working in the chiral limit, all terms multiplied by a pion mass on the OPE side of the sum rule must vanish. This eliminates the quark condensate term via the Gell-Mann–Oakes–Renner relation, which states [60, 61]

$$-f_\pi^2 m_\pi^2 = m_u\left\langle \bar{u}u\right\rangle + m_d\left\langle \bar{d}d\right\rangle + \mathcal{O}[m_q^2] . \tag{2.49}$$

The finite-temperature correction to the gluon condensate must also be omitted since it enters at order T^8 in the chiral limit [23]. The remaining terms on the OPE side are then

$$\begin{aligned}\mathrm{RHS} &= C_0 + \frac{1}{24\mathcal{M}^4}\left\langle\frac{\alpha_s}{\pi}G_{\mu\nu}^2\right\rangle_0 + \frac{1}{\mathcal{M}^6}\left[-\frac{56}{81}\pi\alpha_s\left\langle \mathcal{O}_4^V\right\rangle_0 - \frac{18}{7}\epsilon(T)\left(-\frac{56}{81}\pi\alpha_s\right)\left\langle \mathcal{O}_4^V\right\rangle_0\right] \\ &= C_0 + \frac{1}{24}\left\langle\frac{\alpha_s}{\pi}G_{\mu\nu}^2\right\rangle_0 + \frac{1}{\mathcal{M}^6}\left[-\frac{56}{81}\pi\alpha_s\left\langle \mathcal{O}_4^V\right\rangle_0 + \frac{16}{9}\pi\alpha_s\epsilon(T)\left\langle \mathcal{O}_4^V\right\rangle_0\right] . \end{aligned} \tag{2.50}$$

Recalling that we are working with $\kappa_V = \kappa_A = \kappa$, we now we use the factorization hypothesis on the term in brackets to find

$$\text{RHS} = C_0 + \frac{1}{24\mathcal{M}^4}\left\langle \frac{\alpha_s}{\pi} G^2_{\mu\nu} \right\rangle_0 + \frac{1}{\mathcal{M}^6}\left[-\frac{56}{81}\pi\alpha_s\kappa \left\langle \bar{q}q \right\rangle_0^2 + \pi\alpha_s\epsilon(T)\kappa \left\langle \bar{q}q \right\rangle_0^2 \right] . \quad (2.51)$$

We now equate the two sides of the sum rule, Eqs. (2.48) and (2.51), to find

$$\frac{1}{\mathcal{M}^2}\int \frac{\rho_V(s,0)}{s} e^{-s/\mathcal{M}^2} + \frac{\epsilon(T)}{\mathcal{M}^6}\pi\alpha_s\kappa \left\langle \bar{q}q \right\rangle_0^2 = C_0 + \frac{1}{24\mathcal{M}^4}\left\langle \frac{\alpha_s}{\pi} G^2_{\mu\nu} \right\rangle_0 + \frac{1}{\mathcal{M}^6}\left[-\frac{56}{81}\pi\alpha_s\kappa \left\langle \bar{q}q \right\rangle_0^2 + \pi\alpha_s\epsilon(T)\kappa \left\langle \bar{q}q \right\rangle_0^2 \right] . \quad (2.52)$$

Comparison with Eqs. (2.17) and (2.18) shows that this expression is just the vacuum QCDSR in the chiral limit for the vector channel along with two factorized four-quark condensate terms, which identically cancel. This procedure may also be applied to the axial-vector channel with the same result.

If we now move away from the chiral limit and work with a finite pion mass, several of the above simplifications do not occur. The LHS remains the same, but the RHS now retains the quark condensate term which was eliminated by taking m_π to zero. In addition, since $\epsilon(T)$ no longer reduces to $T^2/(6f_\pi^2)$, we must now work to order λ^2 instead of T^2. Thus we must include both the gluon condensate temperature correction and the non-scalar condensates. These extra terms explicitly violate the QCDSR at order λ^2.

Our conclusion is that, when using the factorization hypothesis with $\kappa_V = \kappa_A$ and working strictly to leading order, the inclusion of a finite pion mass explicitly violates the QCD sum rules. This magnitude of this violation will be determined not only by the numerical values of the condensates, but also by the shape of the vector

and axial-vector spectral functions. Therefore, we proceed to a numerical analysis in order to quantify the violation of the QCDSRs.

2.4.2.2 Numerical Analysis

The graphical display of the results from the vector and axial-vector sum rules is shown in Fig. 2.3. The LHS (solid curve) and RHS (dashed curve) of each channels' sum rule are plotted as a function of Borel mass at four different temperatures. The vertical line in each plot indicates the vacuum Borel window, as discussed below. In Table 2.2 we quantify the agreement between the two sides of the sum rules in terms of the d value given by Eq. (2.40). Since the vacuum sum rules are not exactly satisfied, we have included the zero-temperature results for comparison. We see that the finite-temperature QCDSRs are reasonably satisfied ($d \lesssim 1\%$) for temperatures up to $\approx$ 140 MeV. Within this temperature range the deviations are approximately linear in ϵ, as one would expect from the leading-order linear temperature dependencies of the spectral functions and condensates (which are linear in ϵ). We therefore conclude that the QCD sum rules are reasonably satisfied for temperatures $T \lesssim 140$ MeV.

Since we are conducting a numerical analysis of the sum rules, we must ensure that we have control over the associated numerical uncertainties. Fig. 2.3 shows that the lower limit of the Borel window significantly decreases with rising temperature. This decrease stems from the temperature dependence of the C_3 terms. Since those terms decrease with temperature, the limit of a 10% contribution to the OPE by the C_3 term causes the minimum acceptable Borel mass to drop appreciably below the vacuum limit. This is shown in Fig. 2.3 where the vertical lines indicate the lower bound of the vacuum Borel window. If we keep the vacuum Borel window instead of altering it with temperature, the sum rules remain reasonably satisfied up to $T \approx$ 160–170 MeV. This is displayed in Table 2.2 where the values in parentheses show

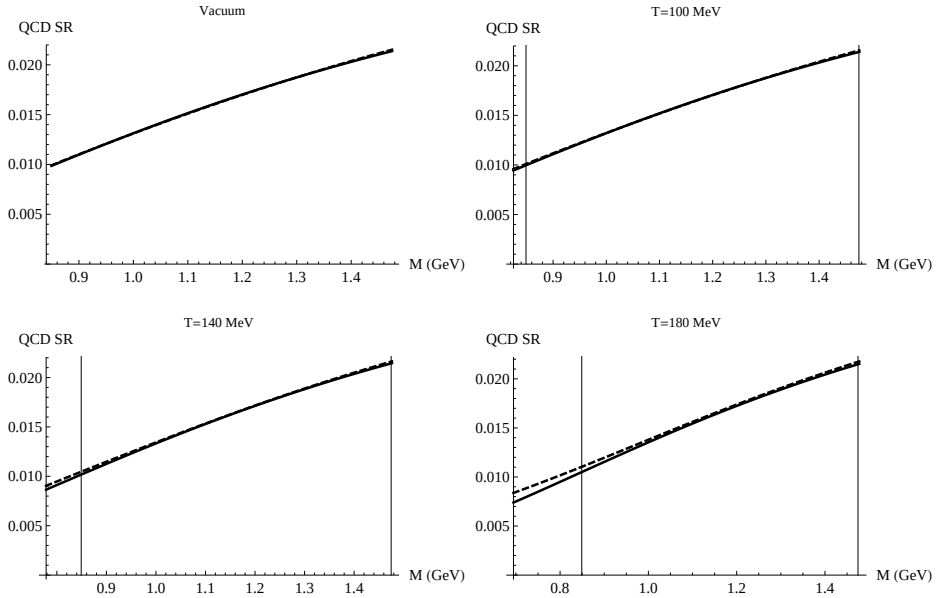

(a) Vector Channel

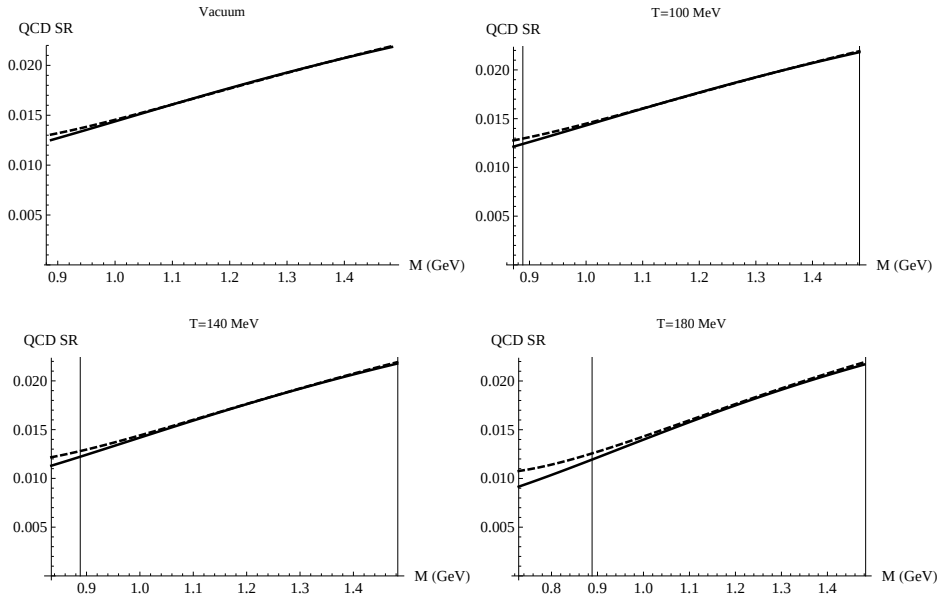

(b) Axial-Vector Channel

Figure 2.3: Comparison of the LHS (solid curve) and RHS (dashed curve) of the QCDSRs for the the vector (upper panels) and axial-vector (lower panels) channels at select temperatures. The extent of each plot corresponds to the Borel window at that temperature, while the vertical lines designate the Borel window in vacuum.

T (MeV)	0	100	110	120	130
ϵ	0	0.06	0.08	0.10	0.13
$d_V(\%)$	0.24	0.32(0.29)	0.38(0.33)	0.48(0.39)	0.64(0.51)
$d_A(\%)$	0.56	0.65(0.57)	0.70(0.58)	0.78(0.61)	0.90(0.67)
T (MeV)	140	150	160	170	180
ϵ	0.16	0.20	0.23	0.28	0.32
$d_V(\%)$	0.85(0.64)	1.11(0.74)	1.43(0.97)	1.82(1.17)	2.29(1.39)
$d_A(\%)$	1.08(0.76)	1.30(0.88)	1.60(1.01)	1.98(1.17)	2.53(1.34)

Table 2.2: Average deviation of the QCDSRs over the Borel window for the vector and axial-vector channels at select temperatures. Values in parentheses are based on a frozen Borel window identical to the vacuum one.

the d value calculated with the vacuum Borel window.

The non-scalar terms in the OPE are another source of uncertainty in our analysis. The values of the twist-2 condensates, A_2^π and A_4^π, are not well-known, as they are based on the pion structure functions. However, we have found the effect of changing their values on the deviation to be small. Altering the value of A_2^π by 20% causes a *relative* change in the d value in both channels of only 0.7% for all temperatures. A 20% change in the A_4^π condensate causes a relative change in the d values of 0.1% at the lowest temperatures, up to a relative change of $\approx 5\%$ at the highest temperatures. Therefore, we find that changing the values of the twist-2 condensates has minimal effect on the d values in both channels.

The effects of changes to the twist-4 condensate B_2^π are more pronounced. In our analysis, we have set this condensate to zero due to a lack of experimental data on its value. However, we may estimate the effect of a non-zero value by using the value for the nucleon, $B_2^N = -0.247$ GeV^2. The effect of this change on the vector deviation is a change in d_V by less than 1% at 100 MeV and up to a 25% change at 180 MeV. The effect in the axial-vector channel is less, with a relative change in d_A

of 5% at $T = 180$ MeV. We note, however, that the largest changes of the d values take place at the highest temperatures, where the sum rule agreement has already broken down.

2.5 Discussion and Summary

We now put our results into the context of previous finite-temperature sum rule analyses. Most previous works have been based on the ground-state plus sharp-onset continuum ansatz for both the vector and axial-vector channels. This causes two issues. The first is that the continuum onset thresholds for the vector and axial-vector channels are different. The second is that the thresholds can in principle be temperature-dependent. When one uses a rigorous leading-order treatment of spectral functions, i.e., chiral mixing, this raises questions about the mixing of nonperturbative resonances with perturbative continua, where the latter should be chirally invariant. In this work we could avoid such ambiguities in application of finite-temperature effects by using spectral functions with continua between the vector and axial-vector channels which are chirally-invariant (i.e., identical) to begin with. This is enabled by the inclusion of a second excited state in each channel. In addition, we have implemented leading-order temperature dependencies with a strictly-defined expansion parameter which has an unambiguous application in the spectral functions. We have found that the resulting finite-temperature Weinberg-type sum rules are analytically fulfilled for all temperatures, and that the finite-temperature QCD sum rules are analytically fulfilled in the chiral limit. We have also found that the inclusion of a finite pion mass explicitly violates the QCD sum rules at leading order in temperature. Numerically this causes the QCDSRs to break down at temperatures $T \approx m_\pi$. However, as noted in Refs. [29, 51, 52], at these temperatures the mean distance between pions becomes small enough so that their

interactions could become relevant. This indicates that the model of the thermal medium as a non-interacting pion gas begins to break down at that point. In addition, for temperatures above ≈ 140 MeV, thermal resonances other than the pion should become important. For example, the thermal number density ratio between the ρ and the π, $n_\rho/n_\pi \approx 3(m_\rho/m_\pi)^{3/2} e^{-(m_\rho - m_\pi)/T}$, goes from $\approx 3\%$ at $T = 100$ MeV to $\approx 15\%$ at $T = 140$ MeV.

3. THERMAL PHOTON EMISSION FROM HADRONIC SYSTEMS

The utility of photons as probes of QCD matter, as outlined in Sec. 1, reflects the necessity of having theoretical models capable of reliably calculating photonic observables from URHICs, specifically spectra and elliptic flow. Indeed, within the last several years a putative "photon puzzle" has been presented wherein the same models which reproduced dilepton spectra [15, 62] were found to leave discrepancies [63] with direct photon spectra from both the PHENIX and ALICE experiments by a factor ≈ 2 for photon energies between $q_0 \lesssim 3$ GeV [64]. This is accompanied by a slight underprediction in v_2 at PHENIX and to a lesser degree at ALICE [65–71].

Much theoretical work has gone into addressing this photon puzzle [63,64,72–80], with the tentative conclusion that the fireball source has hitherto unaccounted-for thermal sources of photons. The difficulty in addressing this problem lies in the variety of possible sources. For example, QGP radiation contributes heavily to photon spectra, particularly at high energies. However, during this time the fireball has not yet developed sufficient momentum anisotropy to provide the needed v_2 for the emitted photons. In addition, the PHENIX collaboration measured the *effective* temperature of direct-photon spectra to be $T_{\rm eff} \approx 240 \pm 20$ MeV. However, since this radiation originates from matter moving towards the detector at an appreciable fraction of the speed of light, the photons have been blue-shifted. The observed temperature is related to the local rest-frame temperature, T, by a relativistic Doppler shift [81]:

$$T_{\rm eff} = T\sqrt{\frac{1+\beta}{1-\beta}}\,. \tag{3.1}$$

For a typical average flow velocity of $\beta \approx 0.3$–0.5 [63], the effective temperature corresponds to $T \approx 130$–180 MeV, which suggests the notion of direct photons

originating from a hadronic source.

Recently Ref. [64] explored the effect of unaccounted-for hadronic contributions by enhancing hadronic photon emission rates by hand by a factor 2–3 for temperatures $140 \lesssim T \lesssim 200$ MeV. After processing these rates through the evolution of the fireball, they found improved agreement of photon spectra together with the photon v_2 increasing into the lower area of the error bars (c.f. Figs. 10 and 11 in that work).

Recent advances in fireball evolution models used in thermal photon emission calculations, such as dissipative relativistic hydrodynamics [79] or coarse-grained transport [82], still require local photon emission rates from QCD matter as input. These rates are convolved over the entire evolution of the fireball to calculate photon spectra and v_2. However, few advances in photon emission rates from hadronic matter have been made over the past ~ 10 years, the last notable ones being from an extensive calculation of photon-producing meson and nucleon/antinucleon scattering processes [83], meson gas calculations with an in-medium ρ spectral function [84] (2003), and meson Bremsstrahlung [3] (2007), extended to higher photon energies in 2014 [4].

Therefore, it is in order to revisit hadronic emission rates and search for sources of thermal photons which have not yet been accounted for. In the following two chapters we do so, focusing first on purely mesonic contributions. We then examine the baryonic contributions to photon rates and compare the results to those from an in-medium ρ spectral function.

3.1 Thermal Photon Emission Framework

In the remainder of this chapter we present our methods for calculation of thermal photon emission rates from hadronic systems. These methods will be used in the next two chapters to calculate photon rates for both mesonic and baryonic processes.

First we present how we couple the electromagnetic field to hadrons using the vector meson dominance (VMD) model. Then we present our methods of photon rate calculations using both thermal field theory (TFT) and kinetic theory (KT).

3.1.1 Vector Meson Dominance

To introduce electromagnetic interactions into hadronic interactions, we employ the vector meson dominance model [50, 85–87] which postulates that all hadronic electromagnetic interactions proceed through vector mesons. This is realized through in the current-field identity

$$j^{\mu}_{\rm EM} = \frac{m_V^2}{g_V} V^{\mu} \,, \tag{3.2}$$

where $j^{\mu}_{\rm EM}$ is the electromagnetic current, m_V the vector meson mass, g_V its coupling strength, and V^{μ} the field of the vector meson. This can also be expressed in terms of the electromagnetic current correlator:

$$\Pi^{\mu\nu}_{\rm EM} = \frac{m_V^4}{g_V^2} D_V^{\mu\nu} \,, \tag{3.3}$$

where $D_V^{\mu\nu}$ is the vector meson propagator. We neglect the contributions of the ω and ϕ mesons to the electromagnetic current, as their couplings are suppressed by factors of ≈ 11 and ≈ 7, respectively, relative to the $\rho\gamma$ coupling [50, 88]. We use the following interaction Lagrangian to couple the neutral ρ field to the electromagnetic field:

$$\mathcal{L}_{\rho\gamma} = -A^{\mu} C_{\rho} m_{\rho}^2 \rho^0_{\mu} \,. \tag{3.4}$$

Here A^{μ} is the photon field and ρ^0_{μ} the neutral ρ field. Were we to use strict VMD the value of the coupling C_{ρ} would be fixed to be e/g_{ρ}. However, we instead treat it as an adjustable parameter which can be evaluated through the ρ dielectron decay. In practice, these two values only differ by $\approx 15\%$.

3.1.2 Calculations using Thermal Field Theory

Here we lay out the method for calculation of thermal photon rates using thermal field theory. We follow the outline of derivation from Refs. [89, 90]. Consider the interaction between two generic initial and final states, $|i>$ and $|f>$ which results in the emission of an on-shell photon with four-momentum $q_\mu = (q_0, \vec{q})$ and polarization vector ϵ^μ. We are interested in finding the transition rate between the initial and final states, which is

$$R_{fi} = \frac{|S_{fi}|^2}{tV}\,, \tag{3.5}$$

where tV is the proper four-volume and S_{fi} the S-matrix connecting the two states. The S-matrix element for the emission of one photon is

$$\left\langle f \left| \int d^4x j_\mu(x) A^\mu(x) \right| f \right\rangle\,, \tag{3.6}$$

where j_μ is the hadronic electromagnetic current operator and A^μ is the photon field. We make a free-field ansatz for the electromagnetic field, such that

$$A^\mu(x) = \frac{\epsilon^\mu}{\sqrt{2q_0 V}} \left(e^{iq\cdot x} + e^{-iq\cdot x}\right)\,. \tag{3.7}$$

Using translational invariance of the hadronic EM current operator we displace it to the origin by means of a plane wave:

$$\langle f\,|j_\mu(x)|\,i\rangle = e^{i(p_f - p_i)\cdot x}\,\langle f\,|j_\mu(0)|\,i\rangle\,. \tag{3.8}$$

We now insert the expression for the Dirac delta function

$$\int d^4x\, e^{-i(p_x - p_y)\cdot x} = (2\pi)^4 \delta^4(p_x - p_y) \tag{3.9}$$

and the completeness relation for on-shell photons [91]

$$\sum_{\text{spin}} \epsilon_\mu^* \epsilon_\nu = -g_{\mu\nu}\,, \tag{3.10}$$

into the S-matrix element above, integrate over x, and perform the complex square in Eq. (3.5) to obtain

$$\begin{aligned} R_{fi} =& \frac{-g^{\mu\nu}}{2q_0 V}(2\pi)^4[\delta^4(p_i + q - p_f) + \delta^4(p_i - q - p_f)] \\ & \times \langle f\,|j_\mu(0)|\,i\rangle\,\langle i\,|j_\nu(0)|\,f\rangle\ . \end{aligned} \tag{3.11}$$

The first delta function corresponds to absorption of a photon with four-momentum q^μ, and the second delta function to emission of a photon. The former process is not of concern in this work and is omitted from here on. In order to convert this into a thermal emission rate, we sum over final states and average over initial states with the Boltzmann factor $e^{-E_i/T}/Z$, where $Z = \sum_i e^{-E_i/T}$ (i.e., thermal averaging). Doing so yields the differential rate [90]

$$\begin{aligned} q_0 \frac{dR}{d^3q} =& -\frac{g^{\mu\nu}}{2(2\pi)^3}\frac{1}{Z}\sum_{i,f} e^{-E_i/T}(2\pi)^4\delta^4(p_i - p_f - q) \\ & \times \langle f\,|j_\mu(0)|\,i\rangle\,\langle i\,|j_\nu(0)|\,f\rangle\ . \end{aligned} \tag{3.12}$$

This expression is greatly simplified by identifying the finite-temperature spectral function for the photon:

$$\rho_{\mu\nu}(q) = -\frac{1}{Z}\sum_{i,f} e^{-E_i/T}(2\pi)^3\delta^4(p_i - p_f - q)\,\langle f\,|j_\mu(0)|\,i\rangle\,\langle i\,|j_\nu(0)|\,f\rangle\ . \tag{3.13}$$

Performing the sum over states gives us

$$q_0 \frac{dR}{d^3q} = \frac{g^{\mu\nu}}{(2\pi)^3} \pi \, f^B(q_0, T) \, \rho_{\mu\nu}(q) \, . \tag{3.14}$$

Since the spectral function is related to the imaginary part of the (retarded) current-current correlator, we then have [84, 90]

$$q_0 \frac{dR}{d^3q} = -\frac{\alpha_{\rm em}}{\pi^2} f(q_0, T) \, {\rm Im} \, \Pi_{\rm em}(q_0 = |\vec{q}|, T) \, . \tag{3.15}$$

This expression is exact to all orders in the strong coupling and to leading order in the electromagnetic coupling. It is our basis for calculation of thermal photon rates using TFT.

3.1.3 Calculations using Kinetic Theory

Here present our method for calculation of thermal photon emission rates using relativistic kinetic theory. Our outline follows that of Ref. [88].

The cross section for a $1 + 2 \to 3 + \gamma$ photon-producing scattering process is

$$\sigma = \int \frac{2\pi}{4E_1 E_2 v_{12}} \frac{d^3p_3}{2E_3(2\pi)^3} \frac{d^3q}{2q_0} \, \overline{|M|^2} \, \delta^4(p_1 + p_2 - p_3 - q) \, , \tag{3.16}$$

where v_{12} is the relative velocity between the incoming particles, q is the four-momentum of the emitted photon, and $\overline{|M|^2}$ is the initial-state averaged and final-state summed matrix amplitude. The production rate for this process is

$$R = \sum_{E_1, E_2} I n \sigma \, , \tag{3.17}$$

were I is the intensity of incoming particle 1 and n is the target density of particle

2, which are given by

$$I = v_{12}\,\mathcal{N}_1\,\frac{dE_1\,g(E_1)\,f(E_1)}{V}\,, \quad n = \mathcal{N}_2\frac{dE_2\,g(E_2)\,f(E_2)}{V}\,, \tag{3.18}$$

with $g(E_i)$ being the density of states of the i^{th} particle inside the volume V, $f(E_i)$ its thermal distribution factor, and $\mathcal{N}_i$ its spin/isospin degeneracy factor. Inserting these expressions into Eq. (3.16) and taking the thermodynamic limit

$$\sum_{E_1} dE_1\,g_{E_1} \to V\int\frac{d^3p}{(2\pi)^3} \tag{3.19}$$

gives the differential rate

$$\begin{aligned} q_0\frac{dR_\gamma}{d^3q} =& \mathcal{N}\int\frac{d^3p_1}{(2\pi)^3 2E_1}\frac{d^3p_2}{(2\pi)^3 2E_2}\frac{d^3p_3}{(2\pi)^3 2E_3}\,\overline{|M|^2} \\ & \times(2\pi)^4\delta^4(p_1+p_2-p_3-q)f(E_1,T)f(E_2,T)\frac{[1\pm f(E_3,T)]}{2(2\pi)^3}\,, \end{aligned} \tag{3.20}$$

where $\mathcal{N} = \mathcal{N}_1\mathcal{N}_2$ is the overall degeneracy factor of incoming particles, and the "$\pm$" is "+" if particle 3 is a boson (Bose enhancement) and "$-$" if it is a fermion (Pauli blocking). This expression is our basis for calculating thermal photon emission rates using kinetic theory.

4. PHOTON EMISSION FROM MESONS: THE $\pi\rho\omega$ SYSTEM

The exploration of thermal photon emission from a system of π, ρ, and ω particles is motivated by two factors. The first is the relatively large size of the $\pi\rho\omega$ coupling constant [92, 93]. This coupling was pivotal to the identification of the ω t-channel exchange in the $\pi\rho \to \gamma\pi$ process as a significant contributor to thermal photon emission rates generated by both a hot meson gas [84] and by the $\omega \to \pi^0\gamma$ radiative decay [94]. However, in Ref. [84] the ω was treated solely as an exchange particle in photon-producing scattering processes and neither as an incoming nor as an outgoing particle. Since the ω is an unstable 3π state under strong interactions, some care must be taken when evaluating scattering diagrams where the ω is an external particle. The second motivating factor is the fact that the particles involved are relatively light. This results in their thermal distribution factors being less suppressive than heavier-mass particles. In this chapter, we calculate the thermal photon emission rates from the $\pi\rho\omega$ system using relativistic kinetic theory, while cross-checking and verifying our results using thermal field theory.

4.1 Microscopic Ingredients

The ingredients for calculation of thermal photon emission rates using TFT are the ρ/γ self-energy (equivalent within our VMD model), and for KT the Born scattering amplitudes. Both of these are derived from the same effective Lagrangian interactions and form factors. We also must evaluate the parameters in our model.

4.1.1 Effective Lagrangians

We begin with free-field Lagrangians for π and ρ mesons,

$$\mathcal{L}_\pi^0 + \mathcal{L}_\rho^0 = \frac{1}{2}\partial_\mu\vec{\pi}\cdot\partial^\mu\vec{\pi} - \frac{1}{2}m_\pi^2\vec{\pi}\cdot\vec{\pi} - \frac{1}{4}\vec{\rho}_{\mu\nu}\cdot\vec{\rho}^{\mu\nu} - \frac{1}{2}m_\rho^2\vec{\rho}_\mu\cdot\vec{\rho}^\mu\ , \tag{4.1}$$

with the usual definition of the ρ field strength tensor as

$$\vec{\rho}_{\mu\nu} = \partial_\mu\vec{\rho}_\nu - \partial_\nu\vec{\rho}_\mu\ . \tag{4.2}$$

Interactions between the π and ρ may be generated by treating the ρ as the gauge particle of the $SU(2)$ isospin symmetry [50, 87, 95]. We minimally couple the ρ to itself and to the π by promoting simple derivatives to gauge-covariant derivatives such that

$$\partial_\mu \to \partial_\mu + ig_\rho\vec{\rho}_\mu\cdot\vec{\mathcal{T}}\,, \tag{4.3}$$

where g_ρ is the isospin gauge coupling of the ρ. Due to vector meson universality [50, 96], the ρ has approximately the same coupling to all particles with isospin. We identify the coupling g_ρ with the $\rho\pi\pi$ coupling constant, so that $g_\rho = g_{\rho\pi\pi}$. Since we are applying the gauging procedure to isospin-1 fields, we need the matrix elements connecting two isovector fields; $\left\langle\vec{\phi}|\mathcal{T}|\vec{\phi}\right\rangle$. In Cartesian isospin notation, the isospin operator $\vec{\mathcal{T}}$ connecting two isovector fields ϕ_a and ϕ_c has matrix elements of [96]

$$\langle\phi_a|\mathcal{T}_b|\phi_c\rangle = i\epsilon_{abc}\,. \tag{4.4}$$

Applying this procedure to Eq. (4.1) gives $\rho\pi\pi$ and $\pi\pi\pi$ interactions of

$$\begin{aligned}\mathcal{L}_{\rho\pi\pi} &= -g_\rho \vec{\rho}^{\,\mu} \cdot (\partial_\mu \vec{\pi} \times \vec{\pi}) \ , \\ \mathcal{L}_{\rho\rho\rho} &= -\frac{1}{2} g_\rho \vec{\rho}^{\,\mu\nu} \cdot (\vec{\rho}_\mu \times \vec{\rho}_\nu) \ . \end{aligned} \tag{4.5}$$

The anomalous parity-violating $\pi\rho\omega$ interaction is incorporated using the Wess-Zumino term [92, 93]

$$\mathcal{L}_{\pi\rho\omega} = g_{\pi\rho\omega} \epsilon^{\mu\nu\alpha\beta} \partial_\alpha \omega_\beta \partial_\mu \vec{\rho}_\nu \cdot \vec{\pi} \ . \tag{4.6}$$

Interaction terms are typically not gauged, as they are obtained from the gauging of free field Lagrangians. However, our ad-hoc introduction of the Wess-Zumino interaction requires us to gauge this term to maintain gauge invariance in our scattering matrices. Applying the covariant derivative to this term generates a contact term

$$\mathcal{L}_{\pi\rho\rho\omega} = g_{\pi\rho\omega} g_\rho \epsilon^{\mu\nu\alpha\beta} \partial_\alpha \omega_\beta \, (\vec{\rho}_\mu \times \vec{\rho}_\nu) \cdot \vec{\pi} \ . \tag{4.7}$$

Photon interactions are included by coupling the ρ directly to the photon using VMD as laid out in Sec. 3.1.1. Restated for reference, that interaction is

$$\mathcal{L}_{EM} = -A^\mu C_\rho m_\rho^2 \rho_\mu^0 \ . \tag{4.8}$$

With the above Lagrangian interactions established, we may now apply Feynman rules to construct both the needed Born scattering diagrams and the ρ/photon self-energy diagrams.

4.1.2 Form Factors

The above phenomenological Lagrangian interactions treat the particles involved as point-like, i.e., as having zero size. However, mesons are spatially extended objects.

An effective way of treating finite-size effects in scattering theory is with the use of form factors. Simply put, form factors represent the Fourier transform of the spatial charge distribution of an object. They represent the charge distribution "seen" by an external probe. Take the case of an electron scattering off of a spatially-extended charge distribution (e.g., a nucleus) via a virtual photon, schematically shown in Fig. 4.1. If of the electron is much smaller than the mass of the charge distribution,

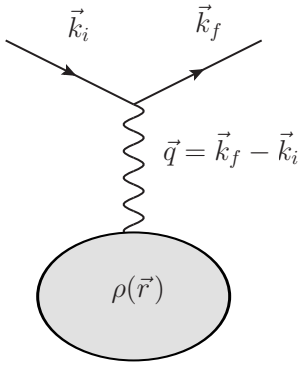

Figure 4.1: Schematic drawing of electron with initial momentum $\vec{k}_i$ and final momentum $\vec{k}_f$ scattering off a charge distribution $\rho(\vec{r})$.

we may neglect any energy transfer between the two. In this case, the relation between the differential cross section of electron scattering off a point charge (i.e., Mott scattering) and the cross section of electron scattering of the charge distribution can be shown to be (see Chap. 8.1 and 8.2 of Ref. [91] for details)

$$\frac{d\sigma}{d\Omega} = \frac{d\sigma}{d\Omega}_{\text{Mott}} |FF(q)|^2 \,, \tag{4.9}$$

where $q = |\vec{q}| = |\vec{k}_f - \vec{k}_i|$ is the three-momentum of the virtual photon and the form factor $FF(q)$ is given by the Fourier transform of $\rho(x)$;

$$FF(q) = \int d^3r\, \rho(\vec{r})\, e^{i\vec{q}\cdot\vec{r}}\,. \tag{4.10}$$

From the above expression we see that the form factor can be interpreted as a measure of how much charge distribution the photon probe encounters in its interaction with the charge distribution. When $q \ll r$ such that the photon has a wavelength (given by the de Broglie relation $q = h/\lambda$) much larger than the size of the charge distribution, the exponential in the Fourier transform is nearly unity. This turns the form factor into the simple integral of the charge distribution over all space, yielding the total charge contained in the distribution. We then recover the Mott cross section for scattering off a point object with a total charge $Q = \int d^3r\, \rho(\vec{r})$. However, if $q \gg r$ such that the wavelength of the photon is comparable to or smaller than the size of the system, the oscillatory behavior of the exponential results in a suppression of the integral. This results in the photon "seeing" a lesser amount of net charge which decreases the scattering cross section relative to the Mott cross section.

The implementation of hadronic form factors is analogous to that of electric form factors. To approximately evaluate interactions between hadrons of finite size, at each hadronic vertex we introduce a form factor which depends on the four-momentum transfer through that vertex. With higher momentum transfer, smaller hadronic structures are resolved which is reflected in a greater form factor suppression. For

s-channel decay processes, we apply to each vertex a dipole[1] form factor of the type

$$FF(s) = \left(\frac{2\Lambda^2 + m_R^2}{2\Lambda^2 + \left[E_2(p_{CM}) + E_3(p_{CM})\right]^2} \right)^2 , \tag{4.11}$$

where $E_i(p_{CM}) = \sqrt{m_i^2 + p_{CM}^2}$ and $p_{CM}(s)$ is the center-of-mass momentum of each hadronic decay particle, i=2,3, and m_R is the mass of the resonant (or decay) particle. Our value of Λ is addressed below. For t-channel scattering processes, we apply to each vertex a dipole form factor

$$FF(t) = \left(\frac{2\Lambda^2}{2\Lambda^2 - t} \right)^2 , \tag{4.12}$$

with $t = (p_1 - p_3)^2$ for incoming (p_1) and outgoing (p_3) four-momenta (and likewise for u-channel processes).

Save for the simplest of processes, like those involving only one Feynman diagram, the implementation of form factors in a gauge-invariant manner is known to be a complicated and involved process [97], especially when more than two particle species are involved. However, we can approximate the effect of form factors by following the prescription of Ref. [84] and implementing a "factorized" form factor. We do so by identifying the dominant scattering diagram for the process, i.e., the diagram with the largest contribution to the photoemission rates at high photon energies, since at low photon energies the form factor effects are small. The dominant process is usually the t-channel diagram involving a light meson as the exchange particle, for example the t-channel π exchange diagram in the process $\pi\rho \to \gamma\omega$, shown in Fig. 4.2 (g). The s-channel processes are suppressed by the exchanged particle propagator

[1]Monopole form factors of the type $(1 + q^2/\Lambda^2)^{-1}$ result from exponentially decreasing charge distributions of $\rho(r) = e^{-\Lambda r}$, while dipole form factors of $(1 + q^2/\Lambda^2)^{-2}$ result from "Yukawa"-type charge distributions of $\rho(r) = r^{-1}e^{-\Lambda r}$.

$(s - m_R^2)^{-1}$. We then use an averaged exchange momentum, $\bar{t}$, in the form factors involved in the dominant diagram. This average momentum is a function of the emitted photon's energy, and is evaluated via the expression

$$\left(\frac{1}{m_X^2 - \bar{t}}\right)^2 \left(\frac{2\Lambda^2}{2\Lambda^2 - \bar{t}}\right)^8 = -\frac{1}{4q_0^2}\int_0^{-4q_0^2} dt \left(\frac{1}{m_X^2 - t}\right)^2 \left(\frac{2\Lambda^2}{2\Lambda^2 - t}\right)^8 , \tag{4.13}$$

where q_0 is the energy of the emitted photon and m_X is the mass of the exchanged particle. If a u-channel diagram dominates, we follow the same procedure but with $\bar{u}$ instead of $\bar{t}$. The resulting form factor is independent of the four-momentum transfer and thus factors out of the total matrix amplitude such that

$$\overline{|M|^2} = \overline{|M_{\text{point}}|^2} F F(\bar{t})^4 . \tag{4.14}$$

This retains the gauge invariance in the amplitude, M_{point}, which is evaluated from the point-like Lagrangian interactions from Sec. 4.1.1.

4.1.3 Evaluation of Parameters

Before we move on to photoemission rate calculations, we must evaluate the four parameters C_ρ, g_ρ, $g_{\pi\rho\omega}$, and Λ. We use the value $\Lambda = 1$ GeV following Ref. [94]. In that work, the above s-channel form factor was applied to the $\rho\pi a_1$, $\rho K K_1$, $\rho\pi h_1$, and $\pi\rho\omega$ mesonic vertices. The cutoff value of $\Lambda = 1$ GeV was found to satisfactorily recover experimental results on the decay widths for both hadronic and radiative decays simultaneously. As mentioned in Sec. 3.1, were we to strictly use VMD our value of C_ρ would be fixed to e/g_ρ. However, we may use experimental data from the $\rho \to e^+e^-$ decay to directly evaluate C_ρ. We similarly use data from the decay

$\rho \to \pi\pi$ decay to evaluate g_ρ. For a 1→2+3 decay where the daughter particles have negligible width, the partial decay width is [91]

$$\Gamma_{1\to 2+3} = \frac{p_{CM}\overline{|M|^2}FF^2(p_{CM})}{8\pi m_1^2} \ , \tag{4.15}$$

where we have used the s-channel form factor from Sec. 4.1.2. The decay matrices for each decay process are listed in Appendix A. Calculations of g_ρ and C_ρ are straightforward. To evaluate $g_{\pi\rho\omega}$, we can use VMD in the $\omega \to \pi^0\gamma$ decay such that the photon proceeds through a virtual ρ. The resulting values for g_ρ, C_ρ, and $g_{\pi\rho\omega}$ are collected in Table 4.1. Now that we have established the necessary Lagrangian in-

Decay Channel	Partial Width	Resulting Coupling
$\Gamma_{\rho\to\pi\pi}$	149.1 MeV	$g_\rho = 6.01$
$\Gamma_{\rho\to e^+e^-}$	7.04 keV	$C_\rho = 0.0611$
$\Gamma_{\omega\to\pi^0\gamma}$	0.703 keV	$g_{\pi\rho\omega} = 21.6$ GeV^{-1}

Table 4.1: Coupling constant values calculated from 2016 PDG [9] data.

teractions, form factors, and coupling constants, we proceed to calculation of thermal photon emission rates.

4.2 Kinetic Theory

As laid out in Sec. 3.1.3, the calculation of photo-emission rates within the framework of relativistic KT requires the squared matrix amplitude of the scattering processes. The $\pi\rho\omega$ system is comprised of three 2→2 scattering processes: $\pi\rho \to \gamma\omega$, $\pi\omega \to \gamma\rho$, and $\rho\omega \to \gamma\pi$. Each processes contains one each of an s-, t-, and u-channel diagram, and a contact (c) term which arises as a result of the gauging procedure,

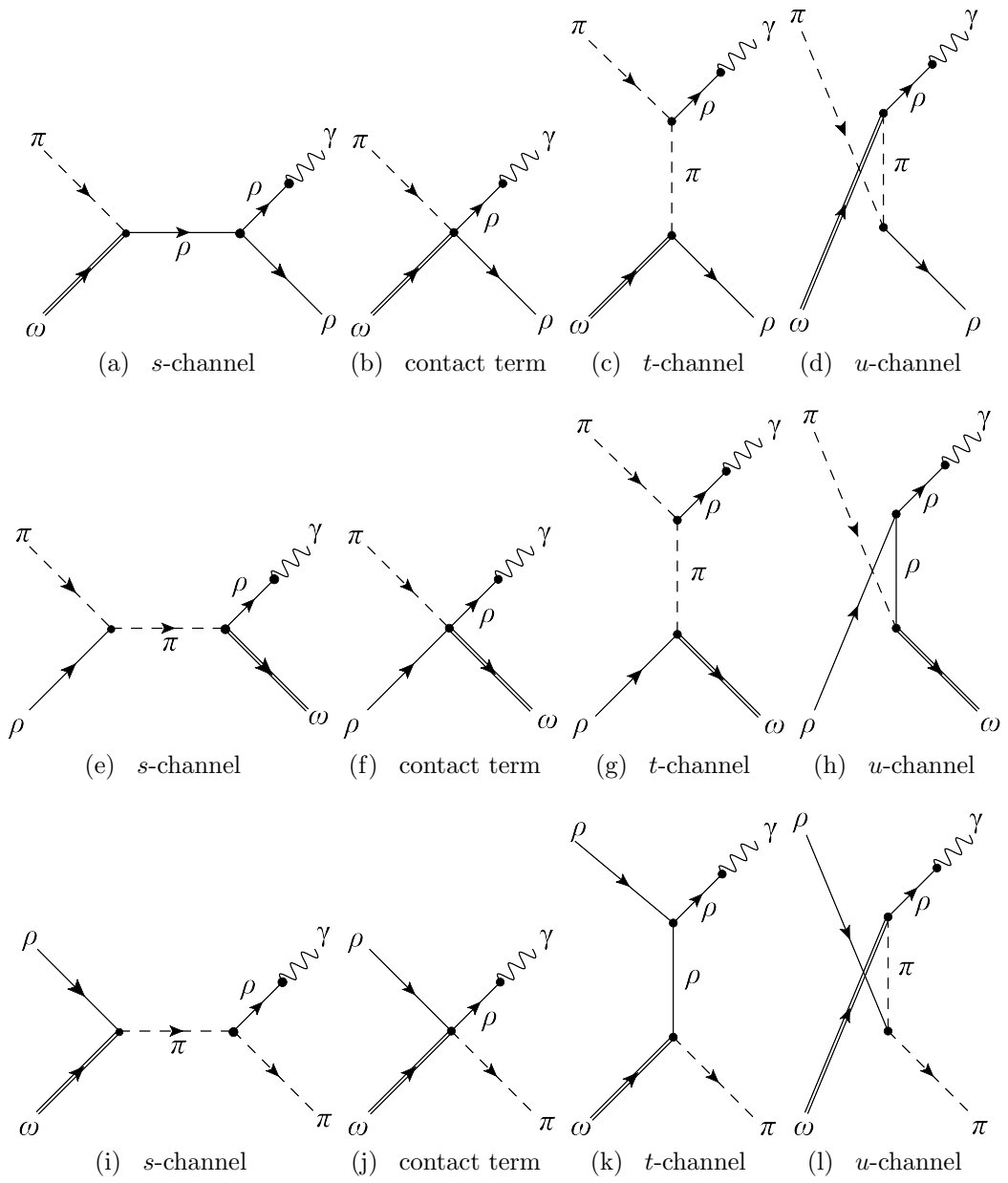

Figure 4.2: Feynman Born diagrams for photon emission from the $\pi\rho\omega$ system. Figs. (a)-(d) show the processes for $\pi\omega \to \gamma\rho$, Figs. (e)-(h) show the processes for $\pi\rho \to \gamma\omega$, and Figs. (i)-(l) show the processes for $\rho\omega \to \gamma\pi$.

and is required for gauge-invariance of the scattering process. The resulting diagrams for each process $\pi\rho \to \gamma\omega$, $\pi\omega \to \gamma\rho$, and $\rho\omega \to \gamma\pi$ are shown in Fig. 4.2.

The input for our KT calculation is the (squared) coherent sum of the matrix amplitudes for each diagram;

$$|M|^2 = |M_s + M_t + M_u + M_c|^2 \ . \tag{4.16}$$

These are constructed by applying Feynman rules to the diagrams in Fig. 4.2 using the previously established Lagrangian interactions and form factor procedure. The matrix elements for each process are given in Appendix A.

Photon emission rate calculations with KT are straightforward for the $\pi\rho \to \gamma\omega$ and $\rho\omega \to \gamma\pi$ processes. However, the $\pi\omega \to \gamma\rho$ process contains a subtlety. In the u-channel diagram shown in Fig. 4.2 (d), it is kinematically allowable that the exchanged pion goes on-shell, such that $u = (p_\omega - p_\rho)^2 = m_\pi^2$. This creates a non-integrable singularity in the corresponding pion propagator when applying Eq. (3.20). This pion pole configuration corresponds to the $\omega \to \pi^0\gamma$ radiative decay, which has already been included in previous rate calculations [84, 94]. We thus need to eliminate this contribution in order to prevent double-counting of the radiative ω decay. To do so, we can exploit the structure of the Wess-Zumino interaction of Eq. (4.6). The four-dimensional Levi-Civita symbol ensures that, when the outgoing ρ is converted to a photon, any diagram containing the Wess-Zumino interaction is automatically gauge-invariant. We demonstrate this by confirming the Ward identity for the $\pi\omega \to \gamma\rho$ process, using the matrix element from Appendix A. This involves contracting the four-momentum of the photon with the Lorentz index of the photon's polarization vector:

$$M_\gamma q^\gamma = \frac{g_{\pi\rho\omega} g_\rho C_\rho}{u - m_\pi^2} (p_2 - q)^\mu p_2^\alpha (p_1 - p_2 + q)_\delta \, \epsilon_{\mu\gamma\alpha\beta} q^\gamma \, \varepsilon^\beta(p_2) \varepsilon^{*\delta}(p_3) \, \epsilon^{3ab} e_a e_b^* \, . \tag{4.17}$$

Focusing on the Lorentz structure of the Levi-Civita symbol, we see that

$$\epsilon_{\mu\gamma\alpha\beta}(p_2 - q)^\mu q^\gamma p_2^\alpha \varepsilon^\beta(p_2) = \epsilon_{\mu\gamma\alpha\beta} p_2^\mu q^\gamma p_2^\alpha \varepsilon^\beta(p_2) - \epsilon_{\mu\gamma\alpha\beta} q^\mu q^\gamma p_2^\alpha \varepsilon^\beta(p_2)\,. \tag{4.18}$$

The Levi-Civita symbol is zero when any two indices are the same. In each of the two terms in Eq. (4.18) the Levi-Civita symbol is contracted with two of the same momenta, p_2 in the first term and q in the second. This same phenomenon will repeat for any such diagram where the photon is emitted from the Wess-Zumino vertex. We conclude that the Lorentz structure of the Levi-Civita symbol ensures that the Ward identity is fulfilled for these diagrams, rendering them gauge invariant without the need for additional diagrams.

We may then separate the u-channel diagram from the other three diagrams in the $\pi\omega \to \gamma\rho$ process without affecting the gauge invariance of the total process. Naïvely, we can avoid the ω radiative decay by excluding timelike pion configurations with $u > 0$ from the integration range in Eq. (3.20), which avoids the singularity. However, this is somewhat of an ad hoc approach and not is not rigorously justified. To scrutinize this issue in detail, we turn to thermal field theory, where this issue does not occur.

4.3 Thermal Field Theory

As mentioned in Sec. 3.1.2, thermal field theory provides a rigorous framework for the calculation of photon emission rates. To calculate rates using Eq. (3.15), we must evaluate the relevant photon self-energy. Each diagram in the KT calculation has a corresponding photon self-energy.

In our current analysis, we focus on the two self-energy diagrams shown in Fig. 4.3. The imaginary parts of these self-energies give rise to the u-channel Feynman diagrams of the $\rho\omega \to \gamma\pi$ (Fig. 4.3 (a)) and $\pi\omega \to \gamma\rho$ (Fig. 4.3 (b)) processes. The latter

process involves the diagram which contains the divergence and double-counting of the ω radiative decay in the KT framework. We use the former as a benchmark of the equivalence between the TFT and KT calculations. In both cases, the photon couples to the Wess-Zumino vertex through the ρ, rendering the diagrams gauge-invariant by themselves.

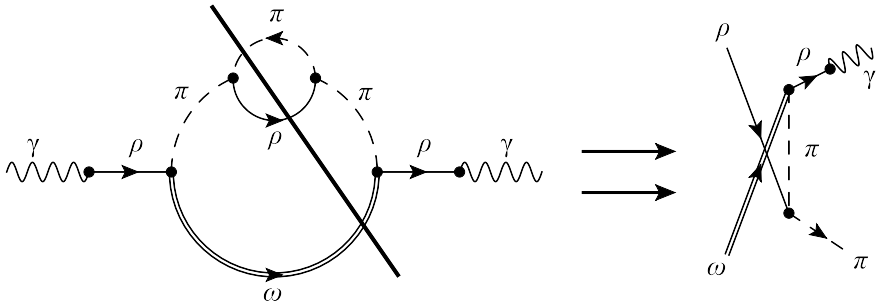

(a) $\rho\omega \to \gamma\pi$ process

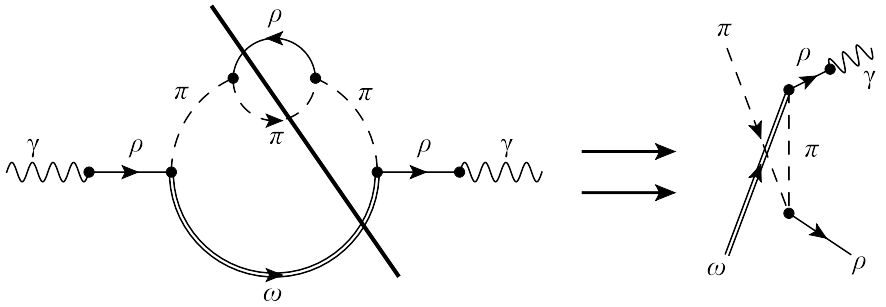

(b) $\pi\omega \to \rho\gamma$ process

Figure 4.3: Cuts of the photon self-energy which generate imaginary parts corresponding to the u-channel diagrams of the $\rho\omega \to \gamma\pi$ and $\pi\omega \to \gamma\rho$ processes.

The two ρ self-energy diagrams have similar structure, differing only by the pion self-energy in the inner loop. The pion propagator is treated fully resummed in a Dyson series, yielding $(u - m_\pi^2)^{-1} \to (u - m_\pi^2 - \Sigma_\pi)^{-1}$. The Σ_π is the self-energy arising from the $\pi\rho$ loop with the thermal pion[2]. We can set up the ρ self-energy

[2]In the TFT diagrams in this work, the "thermal" particle corresponds with the loop particle

without yet evaluating either pion self-energy. By applying standard Feynman rules, we find the ρ self energy to be

$$\Sigma_\rho(q) = \frac{1}{2} P_T^{\mu\mu'} \int \frac{d^3p}{(2\pi)^3} \frac{dp_0}{2\pi} v_{\pi\rho\omega}^{\mu\nu} v_{\pi\rho\omega}^{\mu'\nu'} D_\omega^{\nu\nu'}(p_0, \vec{p}) D_\pi(q_0 - p_0, \vec{q} - \vec{p}) \,. \tag{4.19}$$

Here p is the four-momentum of the ω, which we have separated into its spatial and temporal components. The four-momentum of the ρ is q, D_π is the propagator for the π, and $D_\omega^{\mu\nu} = (-g^{\mu\nu} + p^\mu p^\nu / m_\omega^2) D_\omega$ is the propagator for the ω meson. The $\pi\rho\omega$ vertex function is $v_{\pi\rho\omega}^{\nu\beta} = g_{\pi\rho\omega} \epsilon^{\mu\nu\alpha\beta} q_\mu p_\alpha$. The transverse projection operator P_T removes the 4-D longitudinal components of Σ_ρ as required for a conserved vector current. When taking the ρ self-energy to the photon point of $|\vec{q}| = q_0$ as we are doing, the transverse projection operator becomes $P_T^{\beta\beta'} = -g^{\beta\beta'}$ and the longitudinal component of the ρ self-energy vanishes.

When evaluating the thermal photon emission rates using Eq. (3.15), we omit the real part of the ρ self energy as it is small compared to the ρ mass and has a negligible effect on the rates. We therefore focus on calculating the imaginary part of Σ_ρ. To evaluate Eq. (4.19) using TFT, we use an elegant method from Ref. [89]. This procedure works only for propagators which have simple poles, as ours do. We first set up the integral in vacuum, as we have done above. To obtain the finite-temperature analogue of the vacuum expression, we simply make the propagator replacement

$$\frac{1}{p^2 - m^2 + i\epsilon} \to \frac{1}{p^2 - m^2 + i\epsilon} - \frac{2\pi i}{e^{|p_0|/T} \pm 1} \delta(p^2 - m^2) \,. \tag{4.20}$$

The first term obviously recovers the vacuum expression, while the second term gives

whose arrow points to the left.

the finite-temperature contribution when the delta function is used on p_0. The "$\pm$" term becomes +1 for fermions and -1 for bosons, thus resulting in either the Fermi or Bose thermal distribution function of the particle. There are two possible solutions from the delta function. The first, $p_0 = +\sqrt{\vec{p}^2 + m^2}$, corresponds to a topological configuration where the energy is "positive," or flowing in the direction it would in a vacuum Feynman diagram. The second solution, $p_0 = -\sqrt{\vec{p}^2 + m^2}$, corresponds to a "negative" energy which flows in the opposite direction from its flow in a vacuum Feynman diagram. This method allows us to obtain thermal field theory results from a suitable modification of our vacuum integral.

To evaluate this integral, we first rewrite each propagator using a dispersion relation;

$$D(p_0, \vec{p}) = -\frac{1}{\pi} \int_{-\infty}^{\infty} d\omega \frac{\mathrm{Im}\, D(\omega, \vec{p})}{p_0 - \omega + i\epsilon} \ . \tag{4.21}$$

We treat the ω as a zero-width particle which corresponds to its treatment as an external particle in the KT approach. Therefore,

$$\mathrm{Im}\, D_\omega(p_0, \vec{p}) = -\pi \delta\left(p_0^2 - \vec{p}^2 - m_\omega^2\right) \ . \tag{4.22}$$

Now making the propagator substitution of Eq. (4.20), evaluating the full expressions for the vertex factors, and contracting over Lorentz indices, we find:

$$\begin{aligned}
\Sigma_\rho^T(q_0, \vec{q}, T) = & 4 g_{\pi\rho\omega} \int_{\omega,\omega'=0}^{\infty} \frac{d^3p}{(2\pi)^3} \frac{dp_0}{2\pi}\, d\omega\, d\omega'\, \omega\, \omega' [(p \cdot q)^2 - p^2 q^2] \\
& \times \frac{1}{\pi^2} \mathrm{Im}\, D_\pi(\omega', \vec{p} - \vec{q})\, \mathrm{Im}\, D_\omega(\omega, \vec{p}) \\
& \times \left(\frac{1}{\omega'^2 - (q_0 - p_0)^2} + f_\pi(\omega'; T)\, \delta(\omega'^2 - (q_0 - p_0)^2) \right) \\
& \times \left(\frac{1}{\omega^2 - p_0^2} + f_\omega(\omega; T)\, \delta(\omega^2 - p_0)^2 \right)
\end{aligned} \tag{4.23}$$

Since we are working at the photon point, $q^2 = 0$. The imaginary part of Σ_ρ which concerns us uses the delta function solutions of $p_0 = \omega$ and $p_0 = q_0 - \omega'$. We use those solutions and use the Bose function identity of $f^B(-x) = -1 - f^B(x)$ to find

$$\begin{aligned}\mathrm{Im}\,\Sigma_\rho(q_0,\vec{q},T) &= g^2_{\pi\rho\omega}\int\frac{d^3p}{(2\pi)^3}\frac{1}{2E_\omega}\\ &\times\Big\{(E_\omega q_0-\vec{p}\cdot\vec{q})\,\mathrm{Im}\,D_\pi\left(q_0-E_\omega,\vec{q}-\vec{p}\right)\left[1+f_\pi(q_0-E_\omega,T)+f_\omega(E_\omega,T)\right]\\ &-(E_\omega q_0+\vec{p}\cdot\vec{q})\,\mathrm{Im}\,D_\pi\left(E_\omega-q_0,\vec{q}-\vec{p}\right)\left[f_\pi(E_\omega-q_0,T)-f_\omega(E_\omega,T)\right]\Big\}\,,\end{aligned} \tag{4.24}$$

where $E_\omega = \sqrt{\vec{p}^2+m_\omega^2}$. The inner loop of either diagram constitutes a pion self-energy which enters into the denominator of the resummed pion propagator in Eq. (4.24). The pion self-energies from interactions with a thermal meson m take the form [94]

$$\Sigma_{\pi m}(k_0,\vec{k},T) = \int\frac{d^3p}{(2\pi)^3}\frac{M_{\pi m}(p,\vec{k})}{2E_m}\Big\{f_m(E_m,T)-f_{\pi m}(E_m+k_0,T)\Big\}\,, \tag{4.25}$$

where $M_{\pi m}$ is the forward-scattering amplitude for the $\pi + m \to \pi + m$ process and $f_{\pi m}$ is the Bose factor for the resonance particle in the scattering process. The self-energy for the inner loop in Fig. 4.3 (a) constitutes $\pi\pi$ scattering through an s-channel ρ resonance, while the pion self-energy in Fig. 4.3 (b) is comprised of $\pi\rho$ scattering through an s-channel pion resonance. Taking the imaginary part of the ρ self-energy involves cutting through the loop diagrams, as shown in Fig 4.3. This means each propagator that is severed by the thick line is put on-shell. Thus, the π self-energy $\Sigma_{\pi\pi}$ generates the $\rho\omega \to \gamma\pi$ process, and the π self-energy $\Sigma_{\pi\rho}$ generates the $\pi\omega \to \gamma\rho$ process.

We now proceed to analyze each process in more detail. First we use the process

$\rho\omega \to \gamma\pi$ as a benchmark to establish the equivalence of the photo-emission calculations resulting from the TFT and KT calculations. We will also show how the TFT calculation provides a solution to the issue encountered in the KT calculation. Then we apply this solution to the $\pi\omega \to \gamma\rho$ process to eliminate any double-counting with the ω radiative decay.

4.3.1 $\rho\omega \to \pi\gamma$ u-channel

The u-channel diagram of the $\rho\omega \to \pi\gamma$ process is topologically similar to the $\pi\omega \to \gamma\rho$ process, with one important difference: in the former process the exchanged pion is kinematically forbidden from going on-shell. This allows us to calculate the photon emission rates using both KT and TFT without encountering any ambiguities. The pertinent imaginary part of the ρ self energy has two contributions, schematically shown in Fig. 4.4. These are commonly known as the unitary cut, which represents $\rho \to \pi\omega$ decay on the left-most $\pi\rho\omega$ vertex, and the Landau cut, representing $\pi\rho \to \omega$ scattering on the same vertex. These different cuts can be differentiated based on the direction of the energy flow of the virtual pion. Focusing on the right-most $\pi\rho\omega$ vertex, the unitarity cut is associated with pion energy flow *into* the vertex, as displayed in Fig. 4.4 (a). Since the energy of the ρ is equal to the sum of the energy of the ω and the pion, we can quantitatively classify this cut by noting the energy of the ω must always be less than the energy of the photon; $E_\omega < q_0$. This cut corresponds to the first term in the braces in Eq. (4.24). The Landau cut is associated with a virtual pion energy flow *out of* the right-most $\pi\rho\omega$ vertex, shown in Fig. 4.4 (b). We may classify this cut by noting that $E_\omega > q_0$.

We have calculated the photo-emission rates for the $\rho\omega \to \gamma\pi$ process using both TFT and KT (both without form factors). The resulting rates at $T = 150$ MeV are shown in Fig. 4.5. We find excellent agreement between the full TFT calculation,

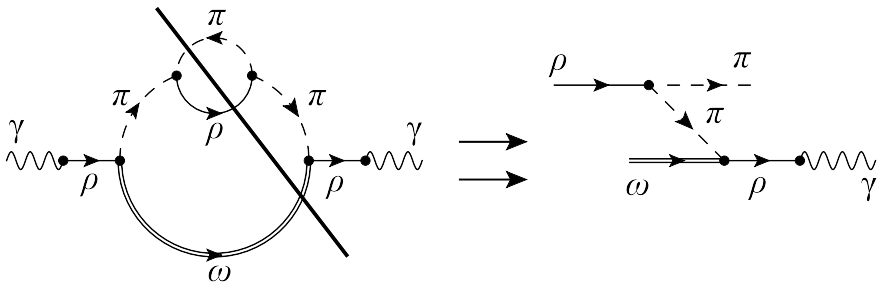

(a) Unitarity cut

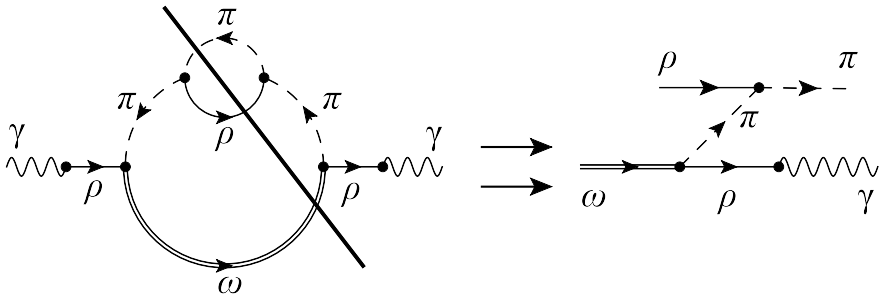

(b) Landau cut

Figure 4.4: Two cuts of the photon self-energy which give rise to imaginary parts corresponding to the u-channel diagram of the $\rho\omega \to \gamma\pi$ process.

given by the sum of the unitarity and Landau cuts, and the KT calculation using Born diagrams. This confirms the equivalence of the two thermal photon emission rate calculations. In addition, we find that the relation of energy flow between the ω and the photon, which differentiate the unitarity and Landau cuts, can be mapped to a KT calculation with an appropriate phase space restriction. Specifically, the unitarity cut, which is given by the energy flow configuration of $E_\omega < q_0$, corresponds to a KT calculation where the phase space is restricted to the exchanged pion energy flowing *into* the $\pi\rho\omega$ vertex, which also corresponds to $E_\omega < q_0$. A similar correspondence exists between the Landau cut, $E_\omega > q_0$, and a KT calculation with phase space restricted to the energy of the exchanged pion flowing *out of* the $\pi\rho\omega$ vertex. This identification of a mapping between the unitarity and Landau cuts to KT is facilitated by the u-channel Born calculation being free from on-shell singularities, contrary to

the case in the $\pi\omega \to \gamma\rho$ process.

Fig. 4.4 (b) demonstrates that the Landau cut of the ρ self-energy gives rise to a Born diagram featuring an $\omega \to \pi\gamma$ decay topology. However, the emitted pion is prevented from going on shell by the top vertex of the diagram, where an on-shell ρ absorbs the emitted pion and converts to an on-shell pion. This is only possible if the pion emitted from the ω decay is heavily space-like. A similar situation exists in the diagram resulting from the unitarity cut, where an on-shell ρ decays into two pions, which is allowable for two on-shell pions. However, one of the emitted pions is absorbed by an on-shell ω which then converts into an on-shell photon. Again, this is only possible for a highly virtual pion. We use these correspondences in the following section to avoid ambiguous results and remove the double-counting the ω radiative decay.

4.3.2 $\pi\omega \to \rho\gamma$ u-channel

As shown in Fig. 4.6, the ρ self-energy corresponding to the u-channel diagram of the $\pi\omega \to \rho\gamma$ process can be separated into unitarity and Landau cuts. In the Born diagram corresponding to the Landau cut, the exchanged pion can go on-shell, which results in the double-counting of the $\omega \to \pi^0\gamma$ radiative decay. In principle, we could use TFT to calculate this process, which unlike its KT counterpart, contains no divergences associated with a pion pole. This is effectively due to a Dyson series resummation of propagator of the pion, which generated a self-energy term that "shields" the propagator from singular behavior: $(u-m_\pi^2)^{-1} \to (u-m_\pi^2-\Sigma_\pi)^{-1}$. However, this calculation would still be double-counting the ω radiative decay, which has already been included in previous calculations of thermal photon emission rates [84, 94] and does not constitute a novel source of thermal photons from the $\pi\rho\omega$ system.

We now use the energy flow distinction between the unitarity cuts and the cor-

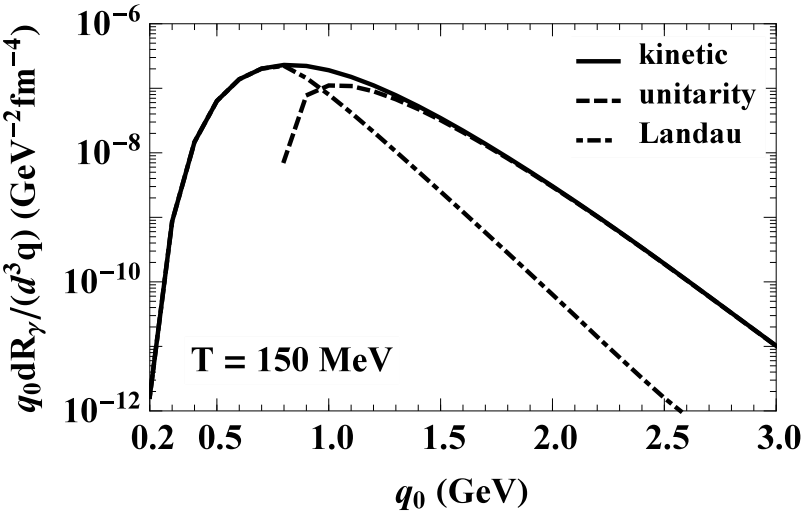

Figure 4.5: Results from photo-emission calculation of $\rho\omega \to \gamma\pi$ via the u-channel diagram at $T = 150\,\mathrm{MeV}$. The solid line is the result using KT over the full kinematic range of the exchanged pion, the dashed line is from TFT via the unitarity cut of Fig. 4.4, and the dot-dashed is from the Landau cut of Fig. 4.4. The sum of the unitarity and Landau cuts is plotted but cannot be seen as it coincides with the solid curve.

respondence between TFT and KT to apply a criterion for what to include in our rates. We omit the Landau cut contribution completely in order to remove the possibility of double-counting the ω radiative decay. We have found that the contribution to photo-emission rates from the TFT unitarity cut agrees with a KT calculation when the phase space is restricted such that $E_\omega < q_0$. We do not explicitly plot this correspondence, since the difference between the two rates is not visible over our plot ranges; c.f. Fig. 4.5 as an example. In principle, this selection is a conservative one, since it removes not only all timelike pions, but also spacelike pions whose energy is allowable by $E_\omega < q_0$.

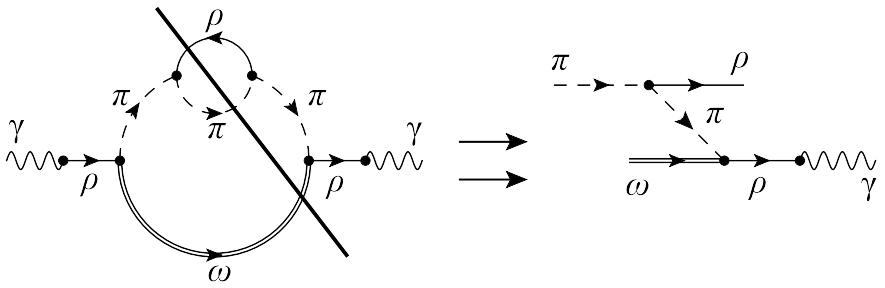

(a) Unitarity cut

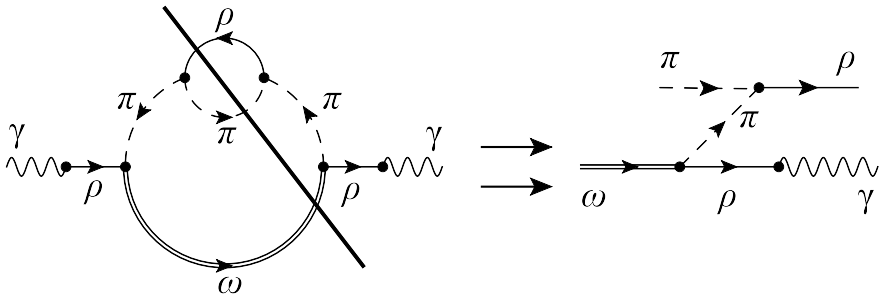

(b) Landau cut

Figure 4.6: Two cuts of the photon self-energy which give rise to imaginary parts corresponding to the u-channel diagram of the $\pi\omega \to \gamma\rho$ process.

4.4 Thermal Photoemission Rates from the $\pi\rho\omega$ System

Before presenting our final results, we will elaborate on our implementation of form factors. The $\pi\omega \to \gamma\rho$ process is dominated by the t- and u-channel pion exchange diagrams. Since the form factors for these diagrams have the same structure (recall Eq. (4.13)), their factorized average form factors are identical and should be applied as an overall form factor to the entire squared matrix amplitude. In the $\pi\rho \to \gamma\omega$ process, the t-channel pion exchange is expected to give a higher contribution to photo-emission rates than the u-channel diagram, which is suppressed by a ρ mass in the propagator. Therefore the pertinent form factor for this process is the average t-channel form factor. Before implementation of form factors, the $\rho\omega \to \gamma\pi$ process has two approximately equal contributions, one being the u-channel

pion exchange and the other being the combined contact, s-, and t-channel terms, which we refer to as "*stc*" for brevity. Again, this separation is possible due to the gauge-invariance of the u-channel process alone. This equality of contributions is shown in Fig. 4.7.

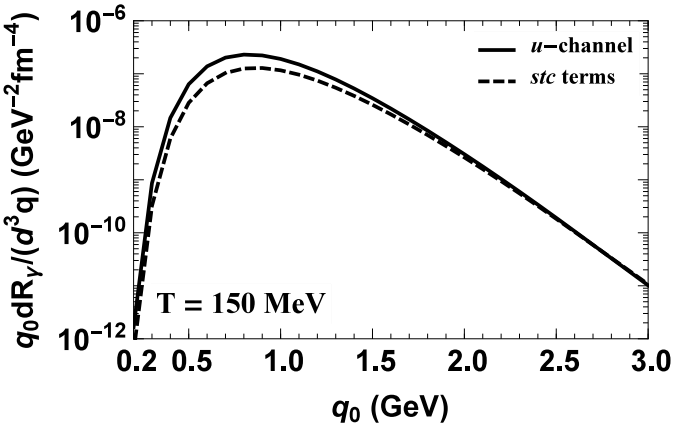

Figure 4.7: Comparison of the contributions to the $\rho\omega \to \gamma\pi$ process from the u-channel diagram (solid line) and the combined *stc* terms (dashed line); no form factors included.

As discussed in Sec. 4.1.2, the factorized form factor suppression is driven by the mass of the exchanged particle. The u-channel diagram involves an exchanged pion whose associated form factor generates a suppression up to a factor 4.5 at $q_0 = 3.0$ GeV. The *stc* terms are dominated by a t-channel ρ exchange at high energies, whose associated form factor generates a suppression up to a factor 30 at $q_0 = 3.0$ GeV. Clearly, using either form factor alone would result in an under- or overestimation of the net form factor suppression. However, once again we find a solution in the form of individually gauge-invariant diagrams. Since we can separate the u- channel and *stc* terms, we can apply an average π-exchange form factor (FF_π) to the u-channel, an

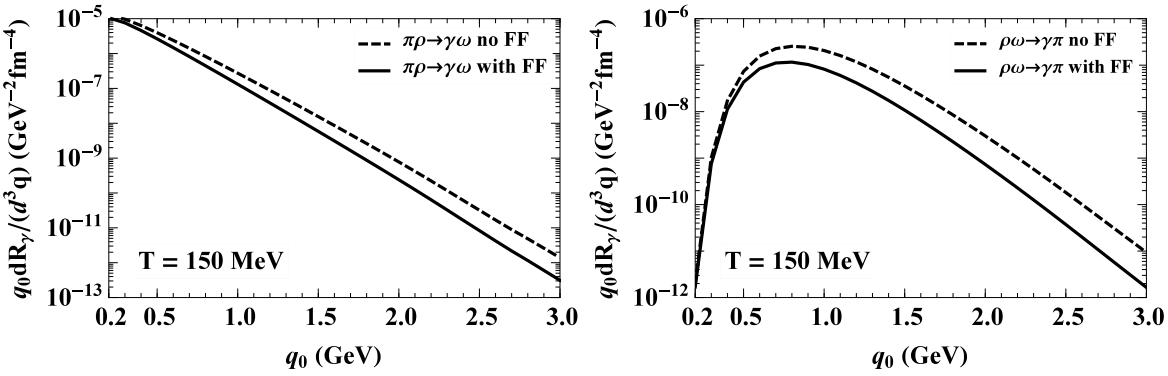

(a) $\pi\rho \to \gamma\omega$ (b) $\rho\omega \to \gamma\pi$

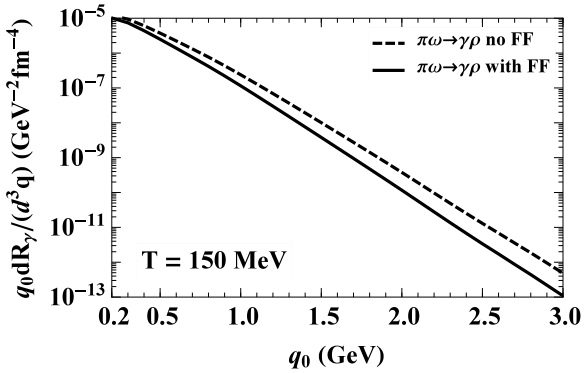

(c) $\pi\omega \to \gamma\rho$

Figure 4.8: Impact of hadronic form factors on the photo-emission rates at $T = 150$ MeV for $\pi\rho \to \gamma\omega$(a), $\rho\omega \to \gamma\pi$(b), and $\pi\omega \to \gamma\rho$(c) processes. The rates with form factor (solid lines) are compared to the ones without form factor (dashed lines).

averaged ρ exchange form factor (FF_ρ) to the *stc* terms, and a combination of the two form factors to the interference term, which is also gauge-invariant. Schematically, we have

$$|M_{\rm FF}|^2 = FF_\pi^4|M_u|^2 + FF_\rho^4|M_{stc}|^2 + FF_\pi^2FF_\rho^2\left(M_uM_{stc}^* + M_{stc}M_u^*\right) \ . \qquad (4.26)$$

The net effect of this implementation is that the total $\pi\rho \to \gamma\omega$ rate is suppressed by a somewhat larger magnitude than the other two processes, but less suppressed than

if we had applied an overall t-channel ρ exchange form factor. We quantitatively show the effect of form factor implementation in all three processes in Fig. 4.8.

We have also examined how variations in the $\Lambda = 1$ GeV form factor cutoff value affect our rates. As mentioned in Sec. 4.1.3, this value simultaneously recovered hadronic and radiative decay width for numerous mesonic interactions. This value was used to calculate all coupling constants in this work. By lowering this cutoff, the form factor suppression is increased, which demands a compensatory increase in the couplings in order to recover the partial decay widths. However, it turns out that a smaller cutoff value of $\Lambda = 0.8$ GeV yields an insignificant change in our decay rates over a photon energy range up to $q_0 = 5.0$ GeV. This is a result of the seesaw effect of lowered form factor cutoffs yielding larger couplings.

4.4.1 Results and Comparison to Existing Rates

Our final results for photon emission rates for all three processes are summarized in Fig. 4.9 (a)-(c) for temperatures of 120, 150, and 180 MeV. In the phenomenologically pertinent regime of $q_0 \approx 1$ GeV, the rates from all three processes are comparable. Below this value the $\rho\omega \to \gamma\pi$ process quickly dies as a result of a lack of phase space. For $q_0 \gtrsim 1.5$ GeV, this process becomes dominant for all temperatures. The relative strength of the processes is stable with temperature; only the $\pi\rho \to \gamma\omega$ process varies slightly. Parametrizations of all three rates are for $0.2 \leq q_0 \leq 5.0$ GeV and $100 \leq T \leq 180$ MeV are given in Appendix B.

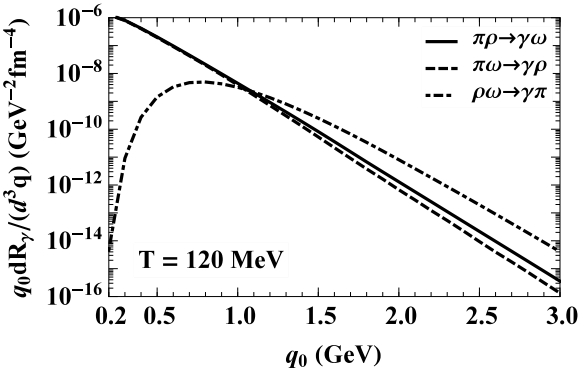

(a) $T = 120$ MeV

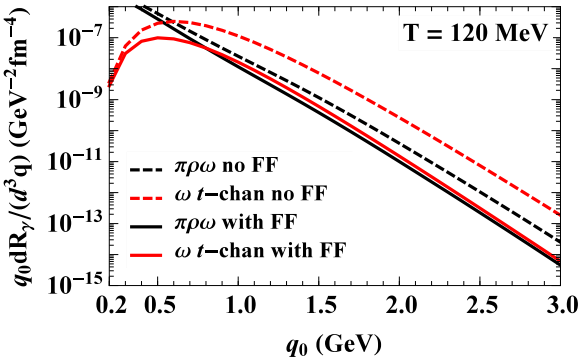

(d) $T = 120$ MeV

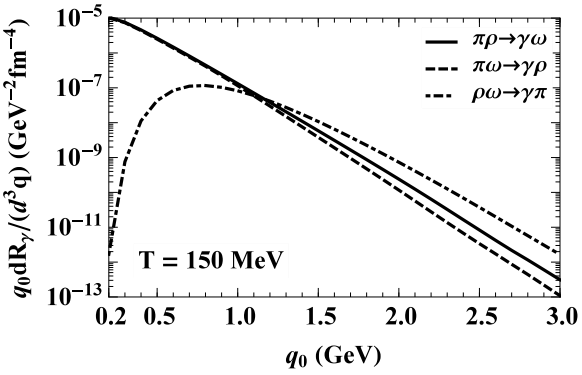

(b) $T = 150$ MeV

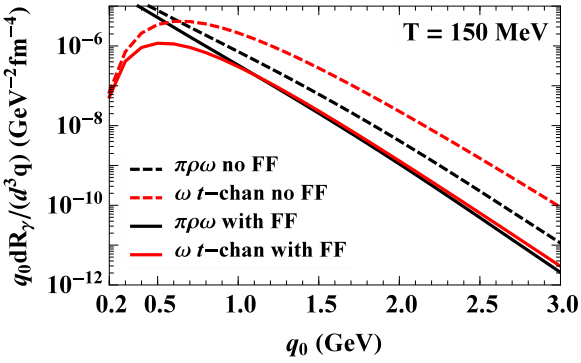

(e) $T = 150$ MeV

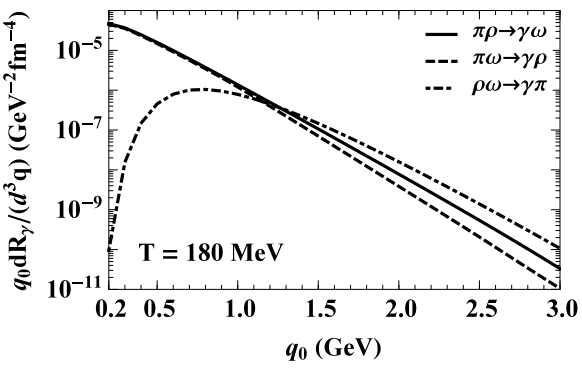

(c) $T = 180$ MeV

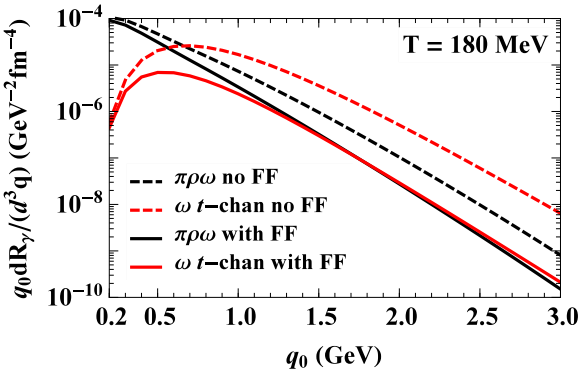

(f) $T = 180$ MeV

Figure 4.9: **LEFT COLUMN:** Rates from the $\pi\rho\omega$ system broken down by individual process at varying temperatures. **RIGHT COLUMN:** Total rates from the $\pi\rho\omega$ system as calculated in the present work (black lines) versus the ω t-channel rate (red line) at varying temperatures. Dashed lines are without form factor; solid lines are with form factor.

We compare our total photon emission rate for the $\pi\rho\omega$ system with two previously-established mesonic calculations. The first is the ω t-channel exchange diagram in the $\pi\rho \to \gamma\pi$ process, calculated in Ref. [84]. This diagram contains the same $\rho\pi\pi$ and $\pi\rho\omega$ vertices employed in this work, but features the ω only as an exchange particle rather than an external one. Its thermal photo-emission rate was found to be comparable to other known thermal photon sources at energies $q_0 \gtrsim 1.5$ GeV, c.f. Refs. [4, 84]. Fig. 4.9 (d)-(f) displays the rates from this process as compared to the $\pi\rho\omega$ system at three temperatures. Each plot shows the photo-emission rates with and without form factors. We see that prior to inclusion of form factors, the ω t-channel rate is larger by a factor 4–5 for photon energies over 1 GeV. However, in the realistic case including form factor implementation, the rates are similar in the phenomenologically relevant regime of $q_0 \lesssim 2.0$ GeV.

We also compare our work to the $\pi\pi$ Bremsstrahlung calculated in Refs. [3, 4]. These rates were found to be appreciable for photon energies $q_0 \lesssim 1$ GeV, and at the lowest energies ($q_0 < 0.3$ GeV) even exceeding the contribution from in-medium ρ mesons with baryonic sources [98, 99]. Fig. 4.10 shows a comparison of the rates from the $\pi\rho\omega$ system, $\pi\pi$ Bremsstrahlung, and the ω t-channel exchange. We see that the rates from the $\pi\rho\omega$ system are comparable to the Bremsstrahlung rates for $0.5 \geq q_0 \geq 1.0$ GeV, suggesting the contribution from this novel source of photons may be significant compared to existing thermal photon rate calculations.

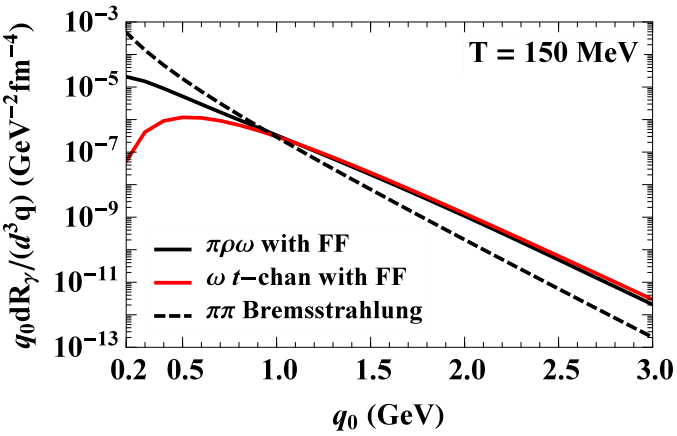

Figure 4.10: Total rates at $T = 150\,\mathrm{MeV}$ from the $\pi\rho\omega$ system (solid black line) compared to the $\pi\pi$ Bremsstrahlung rate (dashed black line) [3, 4] and the $\pi\rho \to \gamma\pi$ ω t-channel rate (red line).

While our current work focuses strictly on thermal photon emission rates, in ultra-relativistic heavy-ion collisions below the chemical freezeout temperature of $T_{\mathrm{ch}} = 160$ MeV effective pion chemical potentials build which will significantly augment two of the three processes in the $\pi\rho\omega$ system. The processes $\pi\omega \to \gamma\rho$ will pick up a pion fugacity factor $z_\pi = \exp\mu_\pi/T$ to the 4^{th} factor, since the ω is a 3π state. Likewise, the process $\rho\omega \to \gamma\pi$ will pick up a pion fugacity to the 5^{th} power, since the ρ is a 3π state. This additional enhancement induces a further significance for its contribution to direct-photon spectra [64].

We have focused on the thermal photon emission rates from the $\pi\rho\omega$ system due to the relatively large $g_{\pi\rho\omega}$ coupling constant and relatively small particle masses which result in relatively large thermal densities. The question remains if higher mass states should also be considered. To answer this question, we can estimate the possible contribution from the a_1 meson. This exhibits a relatively large coupling to $\pi\rho$, approximately half that of the $\pi\rho\omega$ coupling [94]. In that work the contribution

to the ρ self-energy at the photon point from the a_1 is around an order of magnitude smaller than the contribution from the ω meson. This is a result of both the larger $\pi\rho\omega$ coupling, which enters into the photon rate squared, and the thermal densities of the a_1 which, at $T = 150$ MeV, is a factor ≈ 4 smaller than that of the ω. Therefore the contribution from the a_1 and higher mass states should be negligible.

4.5 Discussion and Summary

In this chapter we have calculated the thermal photon emission rates from a system composed of π, ρ, and ω mesons using relativistic kinetic theory. We performed complimentary calculations of photon emission rates using thermal field theory for the u-channel diagrams of two of the processes. By doing so, we established the equivalence between the two approaches, which allowed quality control of our results. Additionally, these dual calculations allowed us both to avoid an ambiguity in the kinetic theory calculation and to identify a criterion by which we avoided double-counting of a previously-calculated contribution to thermal photon emission rates corresponding to the $\omega \to \pi^0\gamma$ radiative decay. After accounting for finite-size effects in hadronic interactions by implementing phenomenological form factors, we found our resulting rates from the entire $\pi\rho\omega$ system to be comparable to rates from the ω t-channel exchange in the $\pi\rho \to \gamma\pi$ process [84] and from $\pi\pi$ Bremsstrahlung [3, 4]. This identification of a novel source of thermal photon production directly supports the conjecture put forth in Ref. [64] that there are unaccounted-for hadronic sources of thermal photons which contribute to both photon spectra and to elliptic flow. Work has been done which supports our expectation of a significant contribution of our rates to photon spectra and v_2 [79, 82].

5. THERMAL PHOTON EMISSION FROM BARYONS

In this chapter we extend our search for thermal photons to include effects from interactions with baryons. We first re-examine and augment the state of existing calculations of thermal photon rates from nucleon and delta resonances, and identify novel contributions from baryonic interactions with the ω meson. We then set forth the microscopic ingredients to our calculations in the form of non-relativistic Lagrangian interactions and form factors. We then constrain our parameter choices using available data from particle decays, proton photoabsorption cross sections, and πN scattering phase shifts. We then show the resulting photon emission rates and compare them to previous calculations.

5.1 Overview of Existing Calculations

Contrary to mesonic sources, exploration of thermal photon rates from baryonic sources has been somewhat limited. Perhaps due to the large number of nucleon and delta resonances, many previous works have leaned toward calculations which use an equation of state obtained from a hadron resonance gas model [100, 101] without explicitly calculating baryon interactions. Other studies included the nucleon, Δ, and $N(1520)$, but could not achieve a quantitative reproduction of proton photoabsorption data [102]. Baryonic photon rates calculated within the Parton-Hadron String Dynamics model [103] included only $V+N \to \gamma+N$ processes with phenomenological cross sections, where V is a vector meson. However, Ref. [83] conducted an extensive calculation of baryon radiative decays and thermal photon-producing processes of the types $XN \to \gamma N$ and $N\bar{B} \to \gamma X$, where X is any of the mesons $\pi, \eta, \rho, \omega, \phi$, and a_1. However, all the photon-producing scattering process involved only the nucleon and not other baryon resonances.

The current state-of-the-art calculations of thermal photon rates from baryonic sources come from the in-medium ρ spectral function of Refs. [94, 98, 99, 104]. By taking this spectral function to the photon point, photon rates from baryonic interactions were generated [84]. The self-energy loops in that spectral function generate direct $\rho B \to \gamma B$ through s-channel baryon resonances. In addition, $\pi\pi$ cloud modifications to the ρ were included which correspond to $\pi B_1 \to \gamma B_2$ scattering processes, such as those shown in Fig. 5.1. However, only nucleons and Δs were explicitly calculated in these loops. The effect of higher baryon resonances in the $\pi\pi$ cloud was approximated by using an effective nucleon density of $\varrho_{\rm eff} = \varrho_N + \frac{1}{2}\varrho_{B^*}$ [98], where the baryon resonance density ϱ_{B^*} was estimated using a hadron resonance gas approach.

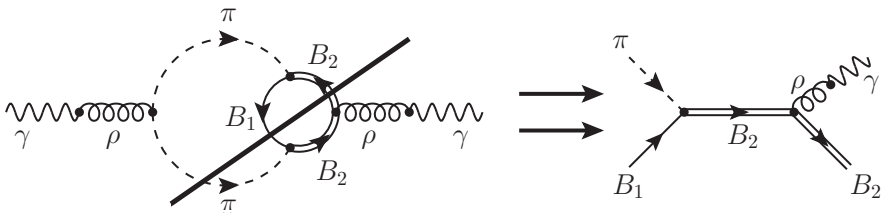

(a) s-channel

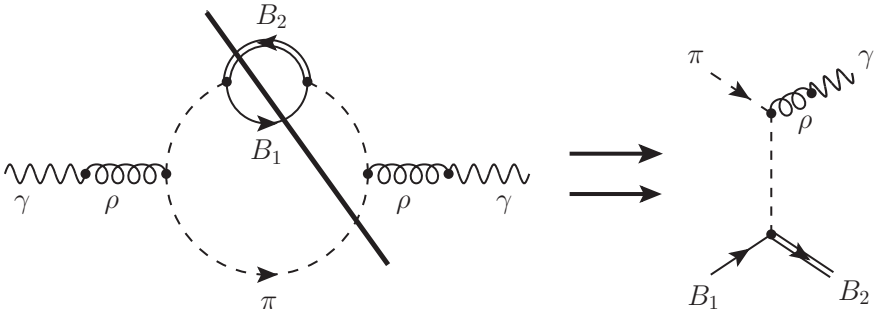

(b) t-channel

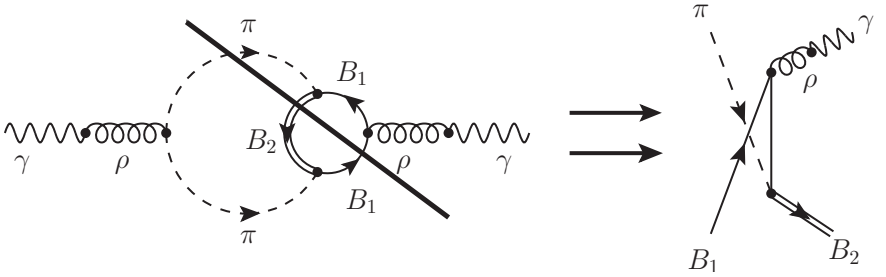

(c) u-channel

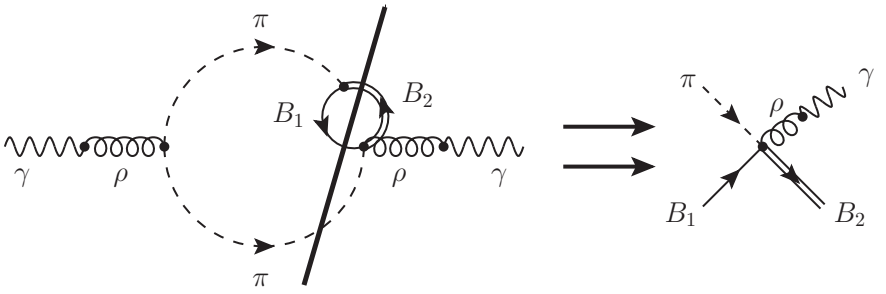

(d) contact term

Figure 5.1: Cuts to pion cloud modifications of the in-medium ρ spectral function which yield our Born scattering diagrams.

The aim of this chapter is to provide direct calculations of thermal photon rates using as full a spectrum of baryons as possible, including hyperons (strangeness-carrying baryons). We calculate thermal photon rates from $\pi B_1 \to \gamma B_2$ processes as shown in Fig. 5.1. In addition, due to the relatively large couplings of the $\pi\rho\omega$ and ωNN, we explore additional baryonic sources which involve the ω meson, shown in Fig. 5.2. Save for the process $\omega N \to \gamma N$, which was previously calculated in Ref. [83], these modifications to the $\pi\omega$ cloud of the ρ are novel contributions to thermal photon emission rates.

The remainder of this chapter is organized as follows. We first lay out the microscopic ingredients for our calculations, which involve Lagrangian interactions, hadronic form factors, and evaluation of free parameters. We constrain the latter using particle decay information from the PDG, elastic πN phase shifts, and proton photoabsorption cross sections. We then present our resulting thermal photon rates, first from the $\pi\pi$ cloud processes, then from the $\pi\omega$. Finally we compare our results to those of the in-medium ρ spectral function and discuss the results.

5.2 Microscopic Ingredients

5.2.1 Effective Lagrangians

We begin with the free-field Lagrangians terms π mesons, ρ mesons, and massive spin-1/2 baryons:

$$\mathcal{L}^0_{B_1} = \bar{\psi}\left(i\gamma^\mu\partial_\mu - m_B\right)\psi\,, \tag{5.1}$$

$$\mathcal{L}^0_{\pi} = \frac{1}{2}\partial_\mu\vec{\pi}\cdot\partial^\mu\vec{\pi} - \frac{1}{2}m_\pi^2\vec{\pi}\cdot\vec{\pi}\,, \tag{5.2}$$

$$\mathcal{L}^0_{\rho} = -\frac{1}{4}\vec{\rho}_{\mu\nu}\cdot\vec{\rho}^{\mu\nu} + \frac{1}{2}m_\rho^2\vec{\rho}_\mu\cdot\vec{\rho}^{\mu}\,. \tag{5.3}$$

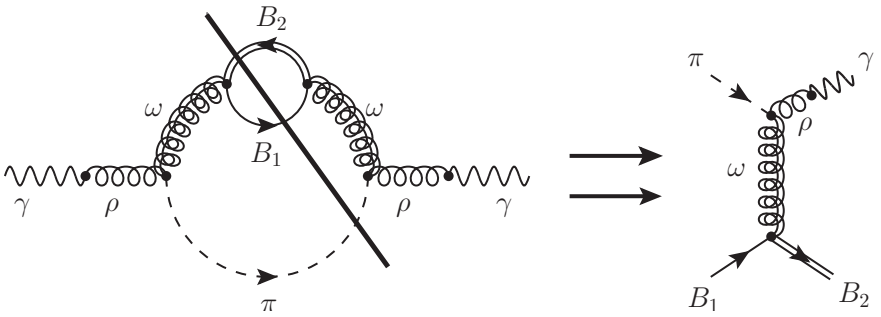

(a) "Internal" ω

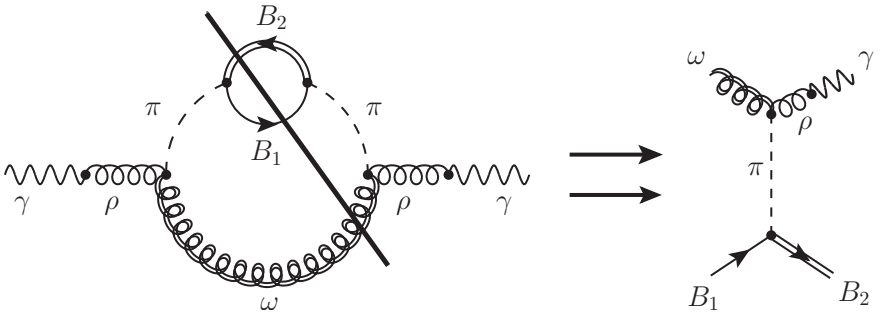

(b) "External" ω

Figure 5.2: Cuts to the $\pi\omega$ cloud of the ρ self-energy which give rise to processes involving an "internal" ω in the scattering process (top), and to an "external" ω (bottom).

The notation B_1 indicates a spin-1/2 baryon. To describe spin-3/2 baryons we start from the Rarita-Schwinger formalism [105]. The free-field Lagrangian for a massive spin-3/2 particle is

$$\mathcal{L}^0_{B_3} = -\bar{\psi}_\mu \left(i\gamma^\mu\partial_\mu - m_B\right)\psi^\mu + \frac{i}{3}\bar{\psi}_\mu \left(\gamma^\mu\partial_\nu + \gamma_\nu\partial^\mu\right)\psi^\nu - \frac{1}{3}\bar{\psi}_\mu\gamma^\mu \left(i\gamma^\mu\partial_\mu + m_B\right)\gamma_\nu\psi^\nu \,. \tag{5.4}$$

For a $\pi B_1 B_2$ interaction term with spin-1/2 baryons, we choose a derivative coupling to respect chiral symmetry [40],

$$\mathcal{L}_{\pi B_{11}} = \frac{f_{\pi B_1 B_2}}{m_\pi}\bar{\psi}(i\gamma_5)\gamma^\mu\partial_\mu\vec{\pi}\cdot\vec{\mathcal{T}}\psi \,. \tag{5.5}$$

The notation B_{11} indicates an interaction between two spin-1/2 baryons. Since the pion field is parity-odd an $i\gamma_5$ factor is needed (or not) if both baryon fields are of the same (different) internal parity. In the above expression $\vec{\mathcal{T}}$ is the isospin transition operator connecting the pion and baryon fields. Its specific form depends on the isospin quantum numbers of the particle to which it couples, i.e., whether the baryons are isospin-1/2 or -3/2; see Table 5.1 for representations of this operator (further details are given in Appendix A). For couplings between pions and two spin-3/2 baryons we make the ansatz

$$\mathcal{L}_{\pi B_{33}} = \frac{f_{\pi B_1 B_2}}{m_\pi}\bar{\psi}_\mu \left(i\gamma_5\right)\gamma^\nu\partial_\nu\vec{\pi}\cdot\vec{\mathcal{T}}\psi^\mu \,, \tag{5.6}$$

with the same requirement for inclusion of the $i\gamma^5$ term as Eq. (5.5). Interactions between pions, spin-1/2, and spin-3/2 particles are given by

$$\mathcal{L}_{\pi B_{13}} = -\frac{f_{\pi B_1 B_2}}{m_\pi}\bar{\psi}_\mu \left(i\gamma_5\right)\partial^\mu\vec{\pi}\cdot\vec{\mathcal{T}}\psi + \text{H.c.} \,, \tag{5.7}$$

where "H.c." indicates the Hermitian conjugate of the previous term.

In Appendix C we show that we require a different Lagrangian interaction to describe interactions between pions, spin-1/2, and spin-3/2 baryons with opposite internal parity, which has a non-relativistic correspondence to a D-wave interaction. For these interactions we introduce the following term [106]:

$$\mathcal{L}^{D}_{\pi B_{13}} = \frac{f_{\pi B_1 B_2}}{m_\pi^2} \bar{\psi}^\mu \gamma_5 \gamma^\nu \partial_\nu \partial_\mu \vec{\pi} \cdot \vec{\mathcal{T}} \psi + \text{H.c.}\,. \tag{5.8}$$

For interactions of pions and baryons with the ρ we use the same minimal substitution gauging procedure as used in Sec. 4.1.1. Upon replacing ordinary derivatives with the covariant derivative we obtain the following Lagrangian interaction terms:

$$\begin{aligned}
\mathcal{L}_{\rho\pi\pi} &= -g_\rho \vec{\rho}^{\,\mu} \cdot (\partial_\mu \vec{\pi} \times \vec{\pi})\ , \\
\mathcal{L}_{\rho\rho\rho} &= -\frac{1}{2} g_\rho \vec{\rho}^{\,\mu\nu} \cdot (\vec{\rho}_\mu \times \vec{\rho}_\nu)\ , \\
\mathcal{L}_{\rho B_{11}} &= -g_\rho \bar{\psi} \gamma^\mu \vec{\rho}_\mu \cdot \vec{\mathcal{T}} \psi\,, \\
\mathcal{L}_{\rho B_{33}} &= g_\rho \bar{\psi}_\mu \gamma^\nu \vec{\rho}_\nu \cdot \vec{\mathcal{T}} - \frac{g_\rho}{3} \bar{\psi} \gamma^\mu \left(\gamma^\mu \vec{\rho}_\nu + \gamma_\nu \vec{\rho}^{\,\mu}\right) \cdot \vec{\mathcal{T}} \psi^\nu + \frac{g_\rho}{3} \bar{\psi}_\mu \gamma^\mu \gamma^\nu \vec{\rho}_\nu \cdot \vec{\mathcal{T}} \gamma_\sigma \psi^\sigma\,, \\
\mathcal{L}_{\pi\rho B_{11}} &= g_\rho \frac{f_{\pi B_1 B_2}}{m_\pi} \bar{\psi} (i\gamma_5) \left(\gamma^\mu \vec{\rho}_\mu \times \vec{\pi}\right) \cdot \vec{\mathcal{T}} \psi\,, \\
\mathcal{L}_{\pi\rho B_{33}} &= g_\rho \frac{f_{\pi B_1 B_2}}{m_\pi} \bar{\psi}_\mu (i\gamma_5) \left(\gamma^\nu \vec{\rho}_\nu \times \vec{\pi}\right) \cdot \vec{\mathcal{T}} \psi^\mu\,, \\
\mathcal{L}_{\pi\rho B_{13}} &= g_\rho \frac{f_{\pi B_1 B_2}}{m_\pi} \bar{\psi}^\mu (i\gamma_5) \left(\vec{\rho}_\mu \times \vec{\pi}\right) \cdot \vec{\mathcal{T}} \psi + \text{H.c.}\,, \\
\mathcal{L}^{D}_{\pi\rho B_{13}} &= g_\rho \frac{f_{\pi B_1 B_2}}{m_\pi^2} \bar{\psi}^\mu \left(i\gamma_5\right) \gamma^\nu \left(\vec{\rho}_\nu \times \partial_\mu \vec{\pi} + \vec{\rho}_\mu \times \partial_\nu \vec{\pi}\right) \cdot \vec{\mathcal{T}} \psi + \text{H.c.}\,,
\end{aligned} \tag{5.9}$$

where $\vec{\rho}_{\mu\nu} = \partial_\mu \vec{\rho}_\nu - \partial_\nu \vec{\rho}_\mu$ is the ρ field strength tensor.

We will also be using interactions with an ω meson. Since the ω is an isosinglet vector meson, we take the $\omega B_1 B_2$ interaction to be similar to the $\rho B_1 B_2$ interaction

but in an isosinglet state [106–108]. This gives the following Lagrangians:

$$\begin{aligned}\mathcal{L}_{\omega B_{11}} &= g_{\omega B_1 B_2}\bar{\psi}(i\gamma_5)\gamma^\mu\omega_\mu\psi\,,\\ \mathcal{L}_{\omega B_{33}} &= g_{\omega B_1 B_2}\bar{\psi}^\mu(i\gamma_5)\omega_\mu\psi + \text{H.c.}\,.\end{aligned} \tag{5.10}$$

There is no $\vec{\mathcal{T}}$ operator in Eq. (5.10) since the ω is an isospin-0 particle and cannot induce transitions between isospin-1/2 and -3/2 states.

The $\pi\rho\omega$ and $\pi\rho\rho\omega$ interactions are identical to those used in Sec. 4.1.1. We use the VMD ρ-γ coupling given in Sec. 3.1.1.

5.2.2 Non-Relativistic Lagrangians

Taking advantage of the large baryon masses, we will be performing an expansion in $|\vec{p}_B|/m_B$ on Dirac and Rarita-Schwinger spinors and propagators, keeping only contributions to 0^{th} order. The reasons for this are threefold. First, the works whose photoemission rates we are supplementing, Refs. [98, 99, 109], used non-relativistic baryonic interaction vertices for the pion cloud effects. To allow for consistent comparisons we should use the same approach. Second, a fully relativistic treatment would require use of the Rarita-Schwinger propagator. Considerable ambiguity exists on its usage for off-shell particles, as it not fully clear how to address the contributions from spin-1/2 states which appear in the off-shell propagator [110, 111]. The third reason is a practical one: A non-relativistic treatment of Dirac spinors dramatically simplifies calculations. The simplifications that result from the non-relativistic treatment of spin-1/2 particles is minor, but treating spin-3/2 particles non-relativistically significantly reduces the amount of work involved in the calculations while still maintaining accuracy at three-momenta up to $q_0 \approx 2$ GeV [112].

The inclusion of a $i\gamma_5$ factor in the relativistic πBB interactions causes differences

in the non-relativistic interactions. We introduce the notation $\mathcal{L}^+$ to indicate the two baryon spinors have the same parity quantum number (whether +1 or -1) and $\mathcal{L}^-$ to indicate they have opposite parity quantum numbers. It is also shown in Appendix C that the individual parity quantum number of each baryon is not relevant to the Lagrangian interaction, only the combination of baryons' parity. For the interaction of two baryons with a pion, schematically displayed in Fig. 5.3, we find

$$\mathcal{L}^+_{\pi B_1 B_2} = \frac{f_{\pi B_1 B_2}}{m_\pi} \chi_1^\dagger \left(\vec{\pi}\cdot\vec{\mathcal{T}}\right)\left(\vec{k}\cdot\vec{\mathcal{S}}\right)\chi_2\,, \tag{5.11}$$

$$\mathcal{L}^-_{\pi B_1 B_2} = \frac{f_{\pi B_1 B_2}}{m_\pi} \chi_1^\dagger \left(\vec{\pi}\cdot\vec{\mathcal{T}}\right)\omega_\pi(k)\,\chi_2\,, \tag{5.12}$$

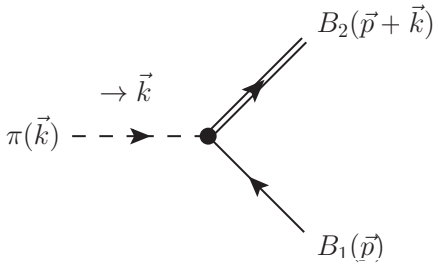

Figure 5.3: Diagrammatic representation of momentum flow of the $\pi B_1 B_2$ vertex given by Eq. (5.12).

The three-momentum of the pion is denoted by $\vec{k}$ and its on-shell energy is $\omega_\pi(k) = \sqrt{m_\pi^2 + \vec{k}^2}$. Here the χ are either two- or four-component spinors in both spin and isospin space, depending on the quantum numbers of the baryons. As mentioned in Sec. 5.2.1, the form of the isospin transition operator $\vec{\mathcal{T}}$ depends on the isospin quantum numbers of the baryons. The spin transition operator $\vec{\mathcal{S}}$ is the spin-space analogue of $\vec{\mathcal{T}}$. We list the notation for the various representations of the

spin and isospin transition operators in Table 5.1, while the explicit matrix elements of all transition operators are given in Appendix A. We note that $\mathcal{L}^-$ describes an S-wave interaction containing no powers of pion momentum, while $\mathcal{L}^+$ is a P-wave interaction containing one power of pion momentum. In principle, we could continue to expand the Dirac spinors to higher orders to obtain higher partial wave terms, but this is at variance with our $\mathcal{O}\left[(\frac{\vec{p}}{m})^0\right]$ expansion. Therefore, we perform our non-relativistic reduction on the relativistic Lagrangian of Eq. (5.8). The non-relativistic spin structure of the D-wave interaction is slightly more complicated than P-wave interactions, and depends on the spin of χ_2, whether 1/2 or 3/2. After the $|\vec{p}_B|/m_B$ expansion (see Appendix C), the resulting interactions are

$$\mathcal{L}^D_{\pi B_1 B_2} = \frac{f_{\pi B_1 B_2}}{m_\pi^2} \begin{cases} \chi_1^\dagger \left(\vec{\pi}\cdot\vec{\mathcal{T}}\right)\left(\vec{k}\cdot\vec{S}\right)\left(\vec{k}\cdot\vec{\sigma}\right)\chi_2\,, & \chi_2 \text{ spin} = \frac{1}{2} \\ \chi_1^\dagger \left(\vec{\pi}\cdot\vec{\mathcal{T}}\right)\left(\vec{k}\cdot\vec{\sigma}\right)\left(\vec{k}\cdot\vec{S}^\dagger\right)\chi_2\,. & \chi_2 \text{ spin} = \frac{3}{2} \end{cases} \tag{5.13}$$

Transition	Spin	Isospin
$1/2 \to 1/2$	$\vec{\sigma}$	$\vec{\tau}$
$1/2 \to 3/2$	$\vec{S}$	$\vec{T}$
$3/2 \to 1/2$	$\vec{S}^\dagger$	$\vec{T}^\dagger$
$3/2 \to 3/2$	$\vec{S}^{(3/2)}$	$\vec{T}^{(3/2)}$

Table 5.1: Representations of spin and isospin transition operators based on the spin/isospin quantum numbers of the initial- and final-state baryons.

The non-relativistic reduction of baryon interactions with the ρ are similarly straightforward. However, as shown in Appendix C, the $\rho B_1 B_2$ interaction requires modification to satisfy a non-relativistic Ward-Takahashi identity (see Refs. [113,114]

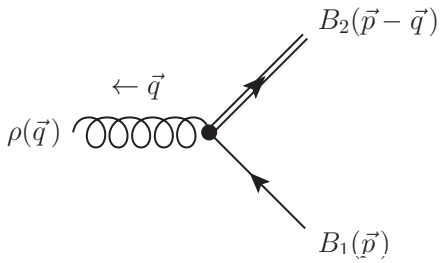

Figure 5.4: Diagrammatic representation of momentum flow of the $\rho B_1 B_2$ vertex given by Eq. (5.14).

for more details). The resulting modified interaction shown in Fig. 5.4 is

$$\mathcal{L}^{+}_{\rho B_1 B_2} = -g_\rho \chi_1^\dagger \rho_\mu \begin{pmatrix} \frac{G_{B_1}^{-1}(p+q) - G_{B_2}^{-1}(p)}{q_0} \\ 0 \end{pmatrix}^\mu \left(\vec{\rho}\cdot\vec{\mathcal{T}}\right) \chi_2 \,, \tag{5.14}$$

where p and q are the baryon and ρ four-momenta, respectively, and G_B is the non-relativistic baryon propagator. We introduce the notation

$$\begin{pmatrix} \mathbb{1} \\ \vec{S} \end{pmatrix}^\mu = \begin{cases} \mathbb{1}\,, & \mu = 0 \\ S_i\,, & \mu = i = 1,2,3\,. \end{cases} \tag{5.15}$$

This object is a four-vector such that contraction with a four-vector p_μ gives

$$\begin{pmatrix} \mathbb{1} \\ \vec{S} \end{pmatrix}^\mu p_\mu = p_0 - \vec{p}\cdot\vec{S}\,. \tag{5.16}$$

We note that in our framework there exists no $\mathcal{L}^{-}_{\rho B_1 B_2}$. This is a result of introducing the ρ as a gauge boson, so that the $\rho B_1 B_2$ interactions generated via gauging the free-field Lagrangians of Eqs. (5.1) and (5.4) result only in interactions between identical

baryons. The non-relativistic baryon contact terms are

$$\mathcal{L}^{+}_{\pi\rho B_1 B_2} = g_\rho \frac{f_{\pi B_1 B_2}}{m_\pi} \chi_1^\dagger \rho_\mu \begin{pmatrix} 0 \\ \vec{\mathcal{S}} \end{pmatrix}^\mu (\vec{\rho} \times \vec{\pi}) \cdot \vec{\mathcal{T}} \, \chi_2 \,, \tag{5.17}$$

$$\mathcal{L}^{-}_{\pi\rho B_1 B_2} = g_\rho \frac{f_{\pi B_1 B_2}}{m_\pi} \chi_1^\dagger \rho_\mu \begin{pmatrix} \mathbb{1} \\ 0 \end{pmatrix}^\mu (\vec{\rho} \times \vec{\pi}) \cdot \vec{\mathcal{T}} \, \chi_2 \,. \tag{5.18}$$

The purely mesonic interactions in Eqs. (5.9) and (4.6) are unaffected by the $|\vec{p}_B|/m_B$ expansion since they have no dependence on spinors.

The non-relativistic versions of Eqs. (5.10) and (4.7) are

$$\begin{aligned} \mathcal{L}^{+}_{\omega B_1 B_2} &= g_{\omega B_1 B_2} \, \chi_1^\dagger \omega_\mu \begin{pmatrix} \mathbb{1} \\ 0 \end{pmatrix}^\mu \chi_2 \,, \\ \mathcal{L}^{-}_{\omega B_1 B_2} &= g_{\omega B_1 B_2} \, \chi_1^\dagger \omega_\mu \begin{pmatrix} 0 \\ \vec{\mathcal{S}} \end{pmatrix}^\mu \chi_2 \,. \end{aligned} \tag{5.19}$$

In principle, these interactions require the same modifications as Eq. (5.14) to satisfy a Ward-Takahashi identity. However, in our analysis we will not be using the $\omega B_1 B_2$ vertex when the omega is an external particle, so that it will not be part of a conserved vector current. Therefore, it does not require the same modification as Eq. (5.14). All processes involving the ω, whether as an external or internal particle, will be coupling via the $\pi\rho\omega$ vertex of Eq. (4.6) with the ρ as an external particle. This vertex is gauge invariant by itself, so that we may use Eq. (5.19) without modification.

Finally, for interactions with photons we use the vector meson dominance $\rho\gamma$ coupling introduced in Eq. (3.4) in Sec. 3.1:

$$\mathcal{L}_{\rho\gamma} = -A^\mu C_\rho m_\rho^2 \rho_\mu^0 \,. \tag{5.20}$$

5.2.3 Hadronic Form Factors

Before we can construct the Born diagrams from Sec. 5.1 via application of Feynman rules, we must account for the finite size of the hadrons involved. As mentioned in Sec. 4.1.2, the inclusion of form factors in scattering process can be a rather involved process. We therefore employ the factorized form factor method from Sec. 4.1.2. For our $\pi B_1 \to \gamma B_2$ photon emission processes, however, we can insert form factors on all $\pi B_2 B_2$ vertices in a fully gauge-invariant manner.

In Ref. [115] it was suggested that the insertion of a monopole πNN form factor, $(\Lambda_\pi^2)/(\Lambda_\pi^2 + \vec{k}^2)$, in nucleon-nucleon scattering diagrams could be diagrammatically visualized as "a particle of mass Λ_π with the same quantum numbers as the π-meson" attaching to the "normal" pion lines; see Figs. 7-9 in that work. Here Λ_π is the value of the form factor cutoff and $\vec{k}$ is the pion's three-momentum. We shall denote this fictitious pion as $\tilde{\pi}$. A rigorous way of using this "heavy pion" method to implement the πNN and $\pi N\Delta$ form factors was introduced in Ref. [109]. There it was shown that, by assigning appropriate Feynman rules for the inclusion of the heavy-pion propagator and pion-heavy-pion vertices, the resulting Feynman diagrams for ρ self-energies generated form factors on all pertinent vertices and also maintained gauge invariance. In Ref. [116] these Feynman rules were implemented in the context of $\pi N \to \rho N$ Born scattering diagrams, as opposed to self-energies. There it was found that the gauge-invariant implementation of the πNN form factor required the inclusion of two t-channel terms: one where the fictitious heavy pion is attached to the external pion line, and one where the heavy pion is attached to the internal pion line. These two diagrams are shown in Fig. 5.5. The remaining contact, s-, and u-channel diagrams have only the external pion to attach the heavy pion, therefore the inclusion of the πNN form factor on those diagrams is straightforward.

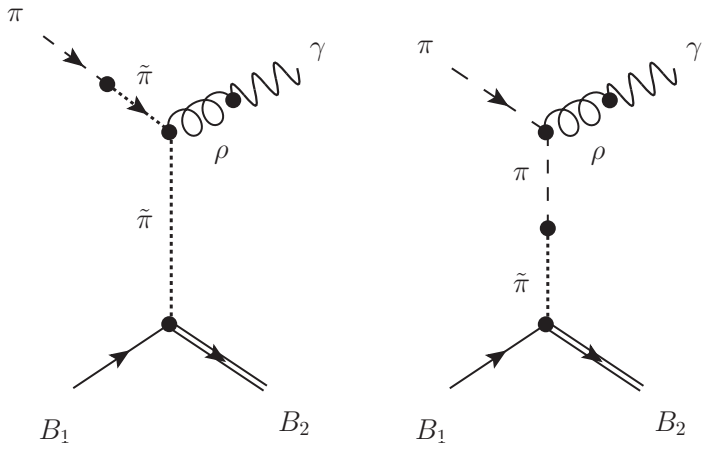

(a) t-channel diagram 1 (b) t-channel diagram 2

Figure 5.5: Two t-channel diagrams that amount to an implementation of $\pi B_1 B_2$ form factors via application of Feynman rules. The long dashed lines indicate "normal" pions while the short dashed lines indicate "heavy" pions.

Since the structure of our $\pi B_1 B_2$ interaction is identical to that of the πNN interaction used in Refs. [109] and [116], we may use the same Feynman rules to implement the $\pi B_1 B_2$ form factor in a gauge-invariant manner. Those rules are:

1. a heavy pion $\tilde{\pi}$ attaches to a normal pion at all possible locations,

2. the heavy pion "propagator" $G_{\tilde{\pi}}$ produces a factor of $-i/(\Lambda_\pi^2 + \vec{k}^2)$, and

3. the pion-heavy pion vertex produces a factor of $i\Lambda_\pi^2$.

The combination of the propagator in item 2 and the vertex in item 3 yields the desired monopole form factor. Item 1 ensures that the resulting combination of diagrams and couplings will be gauge invariant.

As mentioned above, the application of these rules includes a t-channel diagram [116] containing a $\rho\tilde{\pi}\tilde{\pi}$ vertex interaction term where the ρ attaches to two heavy pions, shown in Fig. 5.5. This introduces a complication, as the structure of

this vertex is *a priori* not known. We can, however, use the Ward-Takahashi identity as a means to deduce/construct this vertex. We begin by noting that since the ρ is coupled to a conserved vector current, we demand that the interaction vertex satisfy the Ward-Takahashi identity [113, 114]:

$$q^\mu \tilde{\Gamma}_\mu \stackrel{!}{=} -g_\rho \left(G_{\tilde{\pi}}^{-1}(k-q) - G_{\tilde{\pi}}^{-1}(k) \right) , \tag{5.21}$$

where we have suppressed isospin structure for simplicity. We are not altering the isospin structure of the vertex in any way, so we may temporarily remove it, then reintroduce it after we arrive at our result. Since we know the expression for the heavy pion propagator, we can calculate the difference between the inverse propagators:

$$\begin{aligned} G_{\tilde{\pi}}^{-1}(k-q) - G_{\tilde{\pi}}^{-1}(k) &= \Lambda_\pi^2 + (\vec{k}-\vec{q})^2 - \Lambda_\pi^2 - \vec{k}^2 \,, \\ &= \Lambda_\pi^2 + \vec{k}^2 + \vec{q}^2 - 2\vec{k}\cdot\vec{q} - \Lambda_\pi^2 - \vec{k}^2 \,, \\ &= \vec{q}\cdot(\vec{q} - 2\vec{k}) \,. \end{aligned} \tag{5.22}$$

We may then combine Eqs. (5.21) and (5.22) to find

$$q^\mu \tilde{\Gamma}_\mu \stackrel{!}{=} -g_\rho \vec{q}\cdot(\vec{q} - 2\vec{k}) \,. \tag{5.23}$$

Since the four-momentum of the ρ (which we denote by q) necessarily has a non-zero temporal component (as it is attached to a photon, so $q_0 = |\vec{q}|$), the only possible ρ-heavy pion interaction vertex which satisfies the Ward-Takahashi identity is

$$\tilde{\Gamma}_\mu = -g_\rho \begin{pmatrix} 0 \\ 2\vec{k} - \vec{q} \end{pmatrix}_\mu . \tag{5.24}$$

This vertex is shown schematically in Fig. 5.6. We see that this has the same struc-

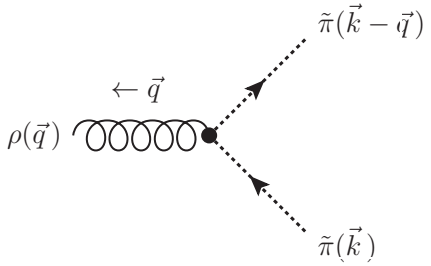

Figure 5.6: Diagrammatic representation of momentum flow of the $\rho\tilde{\pi}\tilde{\pi}$ vertex given by Eq. (5.24).

ture of the "normal" $\rho\pi\pi$ vertex of Eq. (5.9), except that only the spatial components of the four-vector structure figure. This is reasonable since the vertex connects two heavy pion propagators which themselves depend only on the heavy pions' three-momentum. Therefore, satisfaction of the Ward-Takahashi identity demands that the vertex contain no dependence on the temporal component of the pions' four-momentum. Since we have not modified any isospin structure of this new interaction, it is identical to that of the $\rho\pi\pi$ interaction. Having established this vertex, calculation of the matrix elements for S- and P-wave $\pi B_1 \to \gamma B_2$ photon emission processes is straightforward.

The monopole form factor $\Lambda_\pi^2/(\Lambda_\pi^2 + \vec{k}^2)$ is sufficient to ensure convergence in the S- and P-wave $\pi B_1 B_2$ interactions. However, our D-wave interaction contains two powers of pion momentum. There a monopole form factor does not generate sufficiently rapid convergence of the photon emission integral given by Eq. (3.20). Therefore, we introduce an "effective" dipole form factor of the form $\Lambda_\pi^4/(\Lambda_\pi^4 + \vec{k}^4)$. We may then use the same method of introducing the form factor in a gauge-invariant manner, using the following Feynman rules for processes involving a D-wave $\pi B_1 B_2$ interaction:

1. a heavy pion $\tilde{\pi}$ attaches to a normal pion in all possible places,

2. the heavy-pion "propagator" $G_{\tilde{\pi}}$ receives a term of $-i/(\Lambda_\pi^4 + \vec{k}^4)$, and

3. the pion-heavy pion vertex receives a term of $i\Lambda_\pi^4$.

Implementing these rules gives us the same results as for the monopole form factor, but with higher powers of Λ_π and $\vec{k}$. However, since we have altered the propagator of the heavy pion, the above result for the $\rho\tilde{\pi}\tilde{\pi}$ vertex, Eq. (5.23), no longer applies. We must repeat the procedure using the new $1/(\Lambda_\pi^4 + \vec{k}^4)$ propagator to construct a new $\rho\tilde{\pi}\tilde{\pi}$ vertex. The structure of the Ward-Takahashi identity is identical, but the difference in the inverse heavy pion propagators becomes

$$\begin{aligned} G_{\tilde{\pi}}^{-1}(k-q) - G_{\tilde{\pi}}^{-1}(k) &= \Lambda_\pi^4 + (\vec{k}-\vec{q})^4 - \Lambda_\pi^4 - \vec{k}^4\,, \\ &= -4\vec{k}^2(\vec{k}\cdot\vec{q}) + 4(\vec{k}\cdot\vec{q})^2 + 2\vec{k}^2\vec{q}^2 - 4(\vec{k}\cdot\vec{q})\vec{q}^2 + \vec{q}^4 \\ &= \left[-4\vec{k}^2\vec{k} + 4(\vec{k}\cdot\vec{q})\vec{k} + 2\vec{k}^2\vec{q} + \vec{q}^2\vec{q}\right]\cdot\vec{q} - 4(\vec{k}\cdot\vec{q})\vec{q}^2\,. \quad (5.25) \end{aligned}$$

Here we encounter an ambiguity we did not have with the monopole form factor. We need to "factor out" a "$\cdot\vec{q}$" from the above expression in order to identify the vertex, which we have already done to the term in brackets. However, in the second term we may factor out the "$\cdot\vec{q}$" from either the $(\vec{k}\cdot\vec{q})$ or the $\vec{q}^2$ term. We then have two ways to construct the vertex; the Ward-Takahashi identity does not uniquely determine the vertex. Indeed, in an analysis of in-medium Ward and Ward-Takahashi identities, it was noted in Ref. [113] that "...the Ward and Ward-Takahashi identities are useful for checking the consistency of approximations. However, they do not uniquely determine the vertex function at finite momentum transfer. Thus, it is hazardous to extrapolate away from the point of vanishing momentum transfer using only these identities."

The analysis of Ward-Takahashi identities in Ref. [113] involved significantly more

complicated propagators and vertex functions than used in the present work. As shown above, for our simple model we have only two choices for a vertex function using our $1/(\Lambda_\pi^4 + \vec{k}^4)$ propagator[1]. We have used both possible choices for a vertex function to calculate photon emission rates and found that, within the accuracy of this work, there is little difference ($\lesssim 5\%$ for all photon energies) between the resulting rates. Therefore, for our purposes either choice is equally valid; we arbitrarily choose to factor the "$\cdot\vec{q}$" from the $\vec{q}^2$ term in Eq. (5.25). Continuing from that point, we have

$$\begin{aligned} G_{\tilde{\pi}}^{-1}(k-q) - G_{\tilde{\pi}}^{-1}(k) &= \left[-4\vec{k}^2\vec{k} + 4(\vec{k}\cdot\vec{q})\vec{k} + 2\vec{k}^2\vec{q} + \vec{q}^2\vec{q}\right]\cdot\vec{q} - \left[4(\vec{k}\cdot\vec{q})\vec{q}\right]\cdot\vec{q}, \\ &= \left[-4\vec{k}(\vec{k}^2 - \vec{k}\cdot\vec{q}) - \vec{q}(4\vec{k}\cdot\vec{q} - 2\vec{k}^2 - \vec{q}^2)\right]\cdot\vec{q}. \end{aligned} \tag{5.26}$$

Equating this result with the Ward-Takahashi identity of Eq. (5.21), we find a D-wave $\rho\tilde{\pi}\tilde{\pi}$ vertex of

$$\tilde{\Gamma}_\mu^D = -g_\rho \begin{pmatrix} 0 \\ 4\vec{k}(\vec{k}^2 - \vec{k}\cdot\vec{q}) + \vec{q}(4\vec{k}\cdot\vec{q} - 2\vec{k}^2 - \vec{q}^2) \end{pmatrix}_\mu . \tag{5.27}$$

As before, the isospin structure remains unchanged from the "normal" $\rho\pi\pi$ vertex.

We now have defined our $\pi B_1 B_2$ form factor and established a method of implementation that ensures gauge invariance. However, there remain vertices in the $\pi B_1 \to \gamma B_2$ processes which do not have form factors applied to them. Take, for example, the s-channel diagram shown in Fig. 5.1(a). Our above method applies a form factor to the $\pi B_1 B_2$ vertex on the left of the diagram. However, we have not applied a form factor to the $\rho B_2 B_2$ vertex. Similarly, in the t-channel diagram of

[1]It is interesting to note that in the course of this work we have found that any heavy pion propagator of the form $1/(\Lambda_\pi^{2n} + \vec{k}^{2n})$ for $n = 1, 2, 3, ...$ gives exactly n possible choices for constructing a ρ-heavy pion vertex that satisfies the Ward-Takahashi identity.

Fig. 5.1(b), the $\rho\pi\pi$ vertex at the top of the diagram also lacks a form factor. In order to fully account for finite-size effects, we now employ the method from Sec. 4.1.2. We identify the dominant diagram, which is the t-channel pion exchange. We then apply a factorized form factor using an average pion exchange momentum. However, we have already incorporated the $\pi B_1 B_2$ vertex. Therefore, we use a modified version of Eq. (4.13) where we include only the $\rho\pi\pi$ form factor in the averaging procedure. Therefore, to the overall scattering scattering process we apply a dipole $\rho\pi\pi$ form factor of

$$FF_{\rho\pi\pi}(\bar{t}) = \left(\frac{2\Lambda^2_{\rho\pi\pi}}{2\Lambda^2_{\rho\pi\pi} - \bar{t}}\right)^2 , \tag{5.28}$$

where we evaluate $\bar{t}$ via the expression

$$\left(\frac{1}{m^2_{pi} - \bar{t}}\right)^2 \left(\frac{2\Lambda^2_{\rho\pi\pi}}{2\Lambda^2_{\rho\pi\pi} - \bar{t}}\right)^4 = -\frac{1}{4q_0^2}\int_0^{-4q_0^2} dt \left(\frac{1}{m^2_\pi - t}\right)^2 \left(\frac{2\Lambda^2_{\rho\pi\pi}}{2\Lambda^2_{\rho\pi\pi} - t}\right)^4 . \tag{5.29}$$

We use $\Lambda_{\rho\pi\pi} = 1$ GeV in accordance with Sec. 4. This averaged form factor is then applied to the overall amplitude as in Sec. 4.1.2;

$$\overline{|M|^2} = \overline{|M_{\text{point}}|^2} FF(\bar{t})^4 . \tag{5.30}$$

This method accounts for the form factor effects that are not incorporated with the heavy-pion technique. This is the final ingredient for form factor implementation in $\pi B_1 \to \gamma B_2$ processes.

5.2.4 Novel ω Processes

Due to the relatively large $\pi\rho\omega$ coupling, we consider two other processes, shown in Fig. 5.7, both involving the ω meson. The process shown in Fig. 5.7 (a) involves

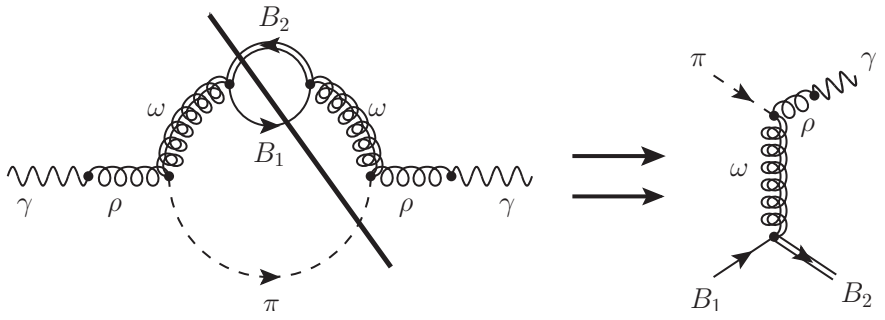

(a) Incoming π

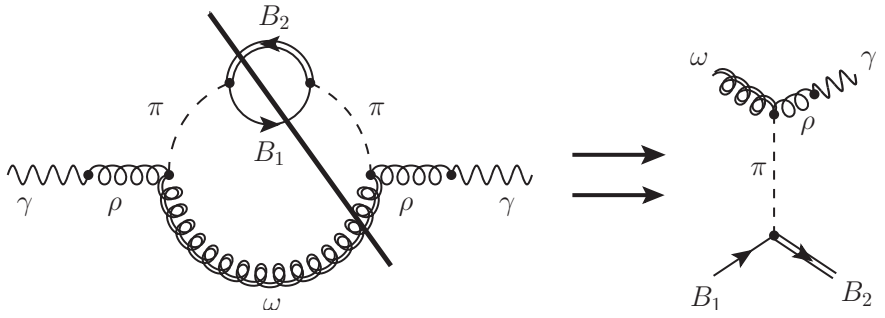

(b) Incoming ω

Figure 5.7: Cuts to the $\pi\omega$ cloud contribution to the ρ spectral function which yield Born scattering diagrams with an incoming pion (top) or with an incoming ω (bottom).

the $\omega B_1 B_2$ vertex of Eq. (5.19), where the ω is an exchange particle. For this vertex, we use the standard monopole form factor $\Lambda^2/(\Lambda^2+\vec{k}^2)$ with $\vec{k}$ being the momentum of the ω. The second process, shown in Fig. 5.7 (b), involves the ω as an external particle, attaching to the $\pi\rho\omega$ vertex of Eq. (4.6). As this is a purely mesonic vertex, we use a dipole form factor of $[2\Lambda^2/(2\Lambda^2-t^2)]^2$. Due to the gauge invariance of the $\pi\rho\omega$ vertex which is in both processes, we need only consider the t-channel diagrams. This allows a straightforward implementation of form factors on both vertices without the need to resort to a factorized form factor.

5.2.5 Parameter Evaluation

The large number of vertices involved in these photoemission processes leave us with a similarly large number of parameters. The purely mesonic parameters we will be using have already been evaluated in Sec. 4. We still need to evaluate the following quantities:

- the coupling constant $f_{\pi B_1 B_2}$ for each possible $\pi B_1 B_2$ vertex, where B_1 and B_2 are any of the baryons under consideration,
- the cutoff $\Lambda_{\pi B_1 B_2}$ for each $\pi B_1 B_2$ vertex form factor,
- the coupling constant $g_{\omega B_1 B_2}$ for each possible $\omega B_1 B_2$ vertex, and
- the cutoff $\Lambda_{\omega B_1 B_2}$ for each $\omega B_1 B_2$ vertex form factor.

We will use data from the Particle Data Group [9] on $B_1 \to \pi B_2$ decays to calculate the $f_{\pi B_1 B_2}$ coupling constants. The data used to calculate decays are given in Appendix D. We neglect all $\pi B_1 \to \gamma B_2$ processes which contain couplings that cannot be calculated due to lack of available decay data. The coupling constants are found by applying Feynman rules to $B_1 \to \pi B_2$ decay processes, then inserting the resulting amplitude into the standard two-particle decay formula. In the rest frame of B_1, this is

$$\Gamma_{B_1 \to \pi B_2} = \frac{p_{CM}}{8\pi m_{B_1}^2} \overline{|M|^2}\, FF(p_{CM})^2 \,, \tag{5.31}$$

where $\Gamma_{B_1 \to \pi B_2}$ is the partial width for the decay process, p_{CM} is the magnitude of the center-of-mass three-momentum of each daughter particle, and $FF(p_{CM})$ is the form factor for the $\pi B_1 B_2$ vertex. $\overline{|M|^2}$ is the initial-state averaged and final-state summed squared matrix amplitude (detailed in Appendix A). This amplitude contains the (squared) coupling we wish to evaluate. The center-of-mass momentum

can be calculated straightforwardly by applying conservation of four-momentum to the invariant mass of the parent particle. Working in the rest frame of the parent particle ($\vec{p}_\pi = -\vec{p}_{B_2}$), we can evaluate the squared four-momentum of the on-shell decay particle:

$$\begin{aligned} q^2 = m_{B_1}^2 &= (p_\pi + p_{B_2})^2 \\ &= p_\pi^2 + p_{B_2}^2 + 2\omega_\pi(p_{CM})E_{B_2}(p_{CM}) - 2\vec{p}_\pi \cdot \vec{p}_{B_2} \\ &= m_\pi^2 + m_{B_2}^2 + 2\sqrt{m_\pi^2 + \vec{p}_{CM}^2}\sqrt{m_{B_2}^2 + \vec{p}_{CM}^2} + 2\vec{p}_{CM}^2 \,, \end{aligned} \tag{5.32}$$

which, after minor algebra, yields

$$p_{CM} = \frac{1}{2m_{B_1}}\sqrt{m_{B_1}^2 - (m_\pi - m_{B_2})^2}\sqrt{m_{B_1}^2 - (m_\pi + m_{B_2})^2} \,. \tag{5.33}$$

The particle properties (masses, widths, decay momenta, etc.) used to find the $\pi B_1 B_2$ couplings are given in Appendix D.

Resonances heavier than the $\Delta(1232)$ have considerable uncertainty in both their total widths and in their branching ratios, both of which are needed to evaluate the $\pi B_1 B_2$ couplings. To account for this uncertainty, we introduce an uncertainty parameter $0.6 \leq y \leq 1.4$ which multiplies the partial width in Eq. (5.31), so that $\Gamma_{B_1 \to \pi B_2} \to y\Gamma_{B_1 \to \pi B_2}$. Additionally, we use the same form factor cutoff for all resonances other than the nucleon and Δ, so that we have only three cutoffs for $\pi B_1 B_2$ interactions: $\Lambda_{\pi NN}$, $\Lambda_{\pi N\Delta}$, and $\Lambda_{\pi BB}$.

This method of calculating couplings is appropriate when the decay products have zero or relatively small width, i.e., they are stable particles. However, if the daughter baryon has a non-negligible width, treating it as a stable particle may no longer be justified. We can then no longer use a fixed-mass approximation for the

daughter baryon's spectral distribution, and rather should integrate over its invariant mass. The extension of Eq. (5.31) is then [104]

$$\Gamma_{B_1\to\pi B_2} = \int dq\, q\, \frac{p_{CM}(q)}{8\pi m_{B_1}^2}\, \overline{|M(q)|^2}\, FF(q)^2\, \rho_{B_2}(q)\,, \tag{5.34}$$

where q^2 is the variable mass of the daughter baryon B_2, and $\rho_{B_2}(q)$ is its spectral function. When B_2 is treated in this manner we imply the replacement $m_{B_2} \to q$ in the expression for p_{CM}. For simplicity, we will model $\rho_{B_2}(q)$ using a Breit-Wigner resonance with an energy-dependent width:

$$\rho_{B_2}(q) = -\frac{1}{\pi}\mathrm{Im}\, D_{B_2}(q) = \frac{1}{\pi}\frac{q\Gamma(q)}{\left(q^2 - m_{B_2}^2\right)^2 + q^2\Gamma(q)^2}\,. \tag{5.35}$$

The width of B_2 is generated by the decay process $B_2 \to \pi N$. This gives us the lower bound for the integration over q in Eq. (5.34), $q_{min} = m_N + m_\pi$. The upper bound for q is given by the amount of energy available for B_2, $q_{max} = m_{B_1} - m_\pi$. These limits also give us a criterion for when we need to use Eq. (5.34) over Eq. (5.31). If the integration range of q covers a sufficient amount of the width of the spectral function, we may approximate ρ_{B_2} with a delta function. If not, then we must integrate over the kinematically available regions of the spectral function. More quantitatively, we must integrate over the spectral function if

$$m_{B_1} - (m_{B_2} + m_\pi) < \frac{\Gamma_{B_2}}{2}\,. \tag{5.36}$$

In practice, only one of our couplings requires this treatment, for the $\Delta(1600) \to \pi N(1440)$ decay. The $N(1440)$ has a width of 350 MeV, and $m_{\Delta(1600)} - (m_{N(1440)} + m_\pi) = 20$ MeV, which necessitates the usage of Eq. (5.34). The calculation of the $\pi N(1440)\Delta(1600)$ coupling with a sharp $N(1440)$ mass using Eq. (5.31) gives

$f_{\pi N(1440)\Delta(1600)} = 8.4$, which turns out to be a gross overestimate. The calculation using Eq. (5.34) and a finite $N(1440)$ width gives $f_{\pi N(1440)\Delta(1600)} = 4.9$.

We may calculate the $g_{\omega B_1 B_2}$ couplings in the same manner as the $f_{\pi B_1 B_2}$ couplings. We note that the ω is an isoscalar particle, so it can couple only to baryons with identical isospin; there are no $\omega N\Delta$ couplings. Additionally, since the ω is not easily reconstructed from its dominant 3π decay, direct data on $B_1 \to \omega B_2$ decays is greatly lacking. The 2016 PDG has data only on decays of the N(1875) and N(1900) to ωN states. However, it was found in Ref. [117] that one can use helicity amplitudes of $N^* \to \gamma N$ decays together with the vector meson dominance model to indirectly estimate $\omega N N^*$ couplings. This also allows us to calculate couplings that occur below the ω production threshold. The couplings are found by equating Eq. (5.31) with the expression for the partial width of a radiative decay in terms of helicity amplitudes, given by [9]

$$\Gamma_{N^* \to \gamma N} = \frac{\vec{p}_{CM}^{\,2}}{\pi} \frac{2m_N}{(2J+1)m_{N^*}} \left(|A_{1/2}|^2 + |A_{3/2}|^2 \right) , \tag{5.37}$$

where J is the spin of the parent particle. We note that $A_{3/2} = 0$ for radiative decays of spin-1/2 resonances. It was shown in Ref. [117] that by taking the appropriate combinations of proton and neutron helicity amplitudes, one can isolate the contributions from the isoscalar (ω) and isovector (ρ) channels. These combinations are

$$A_i^s = \frac{1}{2}(A_i^p + A_i^n), \quad A_i^v = \frac{1}{2}(A_i^p - A_i^n) , \tag{5.38}$$

where s and v indicate the isoscalar and isovector combinations, respectively, and i is 1/2 or 3/2. Using the isoscalar combination of helicity amplitudes then allows us to solve for $g_{\omega N N^*}$. Details of the calculations of the $\omega N N^*$ couplings are given in

Appendix A.

The final step in quantifying the $\pi B_1 B_2$ and $\omega N N^*$ couplings requires to establish values for the form factor cutoffs $\Lambda_{\pi NN}$, $\Lambda_{\pi N\Delta}$, $\Lambda_{\pi BB}$, and $\Lambda_{\omega NN^*}$. Information on the $\pi B_1 B_2$ cutoffs can be inferred by fitting phase shift data for elastic πN scattering. However, there are several constraints on parameter choices we must observe.

5.2.5.1 Constraints from Experimental Data and Previous Works

Previous calculations of the in-medium ρ spectral function [94, 98, 99, 104, 109], which serve as our benchmark, found that the πNN form factor cutoff, $\Lambda_{\pi NN}$, could be no larger than $\approx$ 500 MeV in order to remain consistent with proton photoabsorption data. Larger values yielded non-resonant background cross sections that exceeded experimental data, as shown in Fig 5.8. Furthermore, calculation of the $\pi^- p \to \rho^0 n$ cross section using the same vertices employed here [116] found that consistency with experimental data demanded that $\Lambda_{\pi NN}$ be around 310 MeV with a coupling of $f_{\pi NN} = 1$. We therefore take this cutoff value as fixed and not a free parameter. We allow for a 10% variation in the value of the πNN coupling.

A second constraint applies to the $\pi N\Delta$ form factor cutoff. The works we are comparing to use a cutoff of $\Lambda_{\pi N\Delta} = \Lambda_{\pi NN} = 310$ MeV. This value is constrained by the 2π production contribution to the total proton photoabsorption cross section. The pioneering works which evaluated $\Lambda_{\pi N\Delta}$ via fits to P_{33} phase shift data found excellent agreement with a value of 360 MeV [118–120]. We therefore allow our cutoff to vary up to this value. Additionally, we allow the values of $\Lambda_{\pi BB}$ to vary from 310 MeV (to match the πNN cutoff) up to a value of 1500 MeV, which is a typical size for form factor cutoffs in the Bonn potential model [107].

We are also constrained by our choices for the ωNN coupling and form factor. The process $\gamma N \to \pi N$ via ω t-channel exchange also contributes to the photoab-

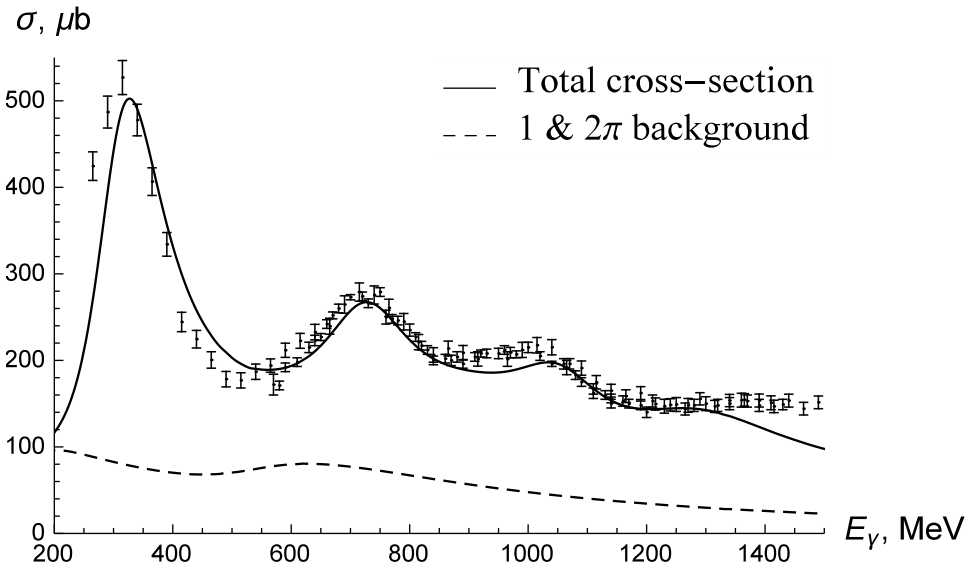

Figure 5.8: Proton photoabsorption cross section calculations [5] with $\Lambda_{\pi NN} = 310$ MeV (solid line) and 1 and 2π production background (dashed line). Data are from Refs. [6, 7]

sorption cross section on the proton. Since this process was not included in the fits using the in-medium ρ spectral function, we add the ω t-channel photoabsorption cross section to the overall result. Our choice of coupling and form factor should not raise the total cross section above the experimental data. The resonance couplings of ωN^* are similarly constrained by the cross sections of $\gamma N \to \omega N^*$ photoproduction processes.

5.2.5.2 Final Parameter Values

To evaluate the remaining parameters $f_{\pi NN}$, $\Lambda_{\pi N\Delta}$, and $\Lambda_{\pi BB}$[2], we will fit the phase shifts for elastic $\pi N \to \pi N$ scattering in the P_{11} (spin-1/2, isospin-1/2) and P_{33} (spin-3/2, isospin-3/2) channels. We neglect the S-wave channel since these involve t-channel diagrams with the exchange of ρ mesons. These diagrams are not in the

[2]We have explored rates from a $\pi\Delta(1232)\Delta(1232)$ coupling using a constituent quark model estimate [121] of $f_{\Delta\Delta} = 1/5 f_{\pi NN}$ and found the resulting rates to be negligible.

P-wave calculations since we do not use a P-wave ρBB interaction. Since we are not using the ρBB form factor in our photoemission rate calculations, calculation of the S-wave phase shifts would involve introducing an extra parameter, $\Lambda_{\rho BB}$, that would not enter into our final calculations for photon rates. The P_{13} and P_{31} channels are neglected due to the relatively small size of their phase shift, $\delta \lesssim 5^\circ$.

The P-wave phase shifts are relatively easily calculated using the K-matrix formalism [122]. The relativistically improved K-matrix (RIKM) model of Oset, Toki, and Weise [96, 123] provides a particularly straightforward way to do so. It is composed of Born diagrams using non-relativistic interactions identical to ours. Energy denominators for the s- and u-channels are then treated relativistically as shown below; see Sec. 2.5.3 of Ref. [96] for details. This relativistic treatment also involves moving beyond the static approximation where nucleon momenta are neglected, i.e., center-of-mass momentum is used instead of simply the momentum of the incoming pion.

Calculation of the phase shift and K-matrix proceeds as follows. First, the unitarity condition on elastic scattering requires that all S-matrix elements vanish save for those where the quantum numbers of the initial and final states are identical [124].

The relation between the S-matrix of a given partial wave and isospin channel α and the corresponding phase shift δ_α reads:

$$S_\alpha = e^{2i\delta_\alpha} \,. \tag{5.39}$$

For P-waves ($l = 1$), the relation between the S-matrix and the K-matrix is [96]

$$S_\alpha = \frac{1 + ikK_\alpha}{1 - ikK_\alpha} \,, \tag{5.40}$$

where k is the magnitude of the center-of-mass three-momentum. Noting that for elastic scattering the phase shift is purely real, we can equate the above expressions to find

$$K_\alpha = \frac{1}{k}\tan\delta_\alpha\,. \tag{5.41}$$

The relativistically improved K-matrix for a given partial wave and isospin channel α is given by[3]

$$K_\alpha = \frac{1}{4\pi}\frac{m_N}{\sqrt{s}}\kappa_\alpha\,, \tag{5.42}$$

where m_N is the nucleon mass, $s = (E_N + \omega_\pi)^2$, where $E_N = \sqrt{m_N^2 + \vec{k}^2}$ and $\omega_\pi = \sqrt{m_\pi^2 + \vec{k}^2}$. The factor $m_N/\sqrt{s}$ is a relativistic flux factor which enters as a result of working in the center-of-mass frame. Each quantity κ_α is constructed out of the s- and u-channel Born scattering terms for a given spin and isospin channel. To illustrate how these quantities are constructed, we will construct the κ_{11} (spin- and isospin-1/2 channel) matrix elements using nucleon and delta resonances. The Born scattering κ-matrix elements $\langle\pi_b(k')|\kappa|\pi_a(k)\rangle = \kappa_N + \kappa_\Delta$ are

$$\begin{aligned}
\kappa_N &= \frac{f_{\pi NN}^2}{m_\pi^2}\left(\frac{\Lambda_{\pi NN}^2}{\Lambda_{\pi NN}^2 + \vec{k}^2}\right)^2\left[\frac{(\vec{k}'\cdot\vec{\sigma})(\vec{k}\cdot\vec{\sigma})}{m_N^2 - s}\tau_b\tau_a + \frac{(\vec{k}\cdot\vec{\sigma})(\vec{k}'\cdot\vec{\sigma})}{m_N^2 - u}\tau_a\tau_b\right]\,,\\
\kappa_\Delta &= \frac{f_{\pi N\Delta}^2}{m_\pi^2}\left(\frac{\Lambda_{\pi N\Delta}^2}{\Lambda_{\pi N\Delta}^2 + \vec{k}^2}\right)^2\left[\frac{(\vec{k}'\cdot\vec{S})(\vec{k}\cdot\vec{S}^\dagger)}{m_\Delta^2 - s}T_bT_a + \frac{(\vec{k}\cdot\vec{S})(\vec{k}'\cdot\vec{S}^\dagger)}{m_\Delta^2 - u}T_aT_b\right]\,.
\end{aligned} \tag{5.43}$$

We must now find the spin- and isospin-1/2 projections of these matrices. This can

[3]The factor $1/4\pi$ is a result of the relation between the scattering amplitude and the transition matrix, see Appendix 8 in Ref. [96].

be done using the projection operators [96]

$$\begin{aligned}
\left\langle \pi_b \left| \hat{P}_{\frac{1}{2}} \right| \pi_a \right\rangle &= \delta_{ab} - \tfrac{1}{3}\tau_b\tau_a \,, \\
\left\langle \pi_b \left| \hat{P}_{\frac{3}{2}} \right| \pi_a \right\rangle &= \tfrac{1}{3}\tau_b\tau_a \,, \\
\left\langle \pi_j \left| \hat{Q}_{\frac{1}{2}} \right| \pi_i \right\rangle &= \delta_{ij} - \tfrac{1}{3}\sigma_i\sigma_j \,, \\
\left\langle \pi_j \left| \hat{Q}_{\frac{3}{2}} \right| \pi_i \right\rangle &= \tfrac{1}{3}\sigma_j\sigma_i \,.
\end{aligned} \tag{5.44}$$

We can invert these expressions to find

$$\begin{aligned}
\tau_b\tau_a &= \left\langle \pi_b \left| 3\hat{P}_{\frac{1}{2}} \right| \pi_a \right\rangle \\
\tau_a\tau_b &= \left\langle \pi_b \left| \left(2\hat{P}_{\frac{3}{2}} - \hat{P}_{\frac{1}{2}} \right) \right| \pi_a \right\rangle \\
T_b T_a^\dagger &= \left\langle \pi_b \left| \hat{P}_{\frac{3}{2}} \right| \pi_a \right\rangle \\
T_a T_b^\dagger &= \left\langle \pi_b \left| \left(\tfrac{4}{3}\hat{P}_{\frac{1}{2}} + \tfrac{1}{3}\hat{P}_{\frac{1}{2}} \right) \right| \pi_a \right\rangle \,.
\end{aligned} \tag{5.45}$$

Identical expressions for spin are given by replacing τ with σ, T_a with S_a, $\hat{P}$ with $\hat{Q}$, and changing from isospin to spin indices. We can now eliminate the spin and isospin matrices in Eq. (5.43) in favor of the projection operators from Eq. (5.45). This allows us to identify the contributions to each spin and isospin channel. The P_{11} channel terms will be those which contain the projector combination $\hat{P}_{\frac{1}{2}}\hat{Q}_{\frac{1}{2}}$. Those combinations are

$$\begin{aligned}
\kappa_N &= \frac{2m_N\vec{k}^2}{3}\frac{f_{\pi NN}^2}{m_\pi^2}\left(\frac{\Lambda_{\pi NN}^2}{\Lambda_{\pi NN}^2+\vec{k}^2}\right)^2\left(\frac{9}{s-m_N^2}+\frac{1}{u-m_N^2}\right) \,, \\
\kappa_\Delta &= \frac{2m_\Delta\vec{k}^2}{3}\frac{f_{\pi N\Delta}^2}{m_\pi^2}\left(\frac{\Lambda_{\pi N\Delta}^2}{\Lambda_{\pi N\Delta}^2+\vec{k}^2}\right)^2\frac{16}{9}\frac{1}{u-m_\Delta^2} \,.
\end{aligned} \tag{5.46}$$

Construction of the κ matrices for other resonances and for other channels is done in

an identical manner by constructing the relevant Born diagrams and evaluating the projections into the needed spin and isospin channel. The original RIKM model included s- and u-channel exchanges of the nucleon, delta, and the $N(1440)$ resonance. We include all P-wave nucleon and delta resonances in our list of particles (see Appendix D), namely the $N(1440)$, $N(1710)$, $N(1720)$, $N(1900)$, $\Delta(1232)$, $\Delta(1600)$, and $\Delta(1910)$.

We may now use the RIKM model to evaluate our parameters $\Lambda_{\pi N\Delta}$, $\Lambda_{\pi BB}$, and $f_{\pi NN}$. We match our phase shifts to the data fits from Ref [8]. We fit center-of-mass momenta from 0 to 300 MeV. In principle, we should limit our analysis to the π production threshold of $k_{\rm cm} \approx 215$ MeV. After this point the phase shift acquires an imaginary part, indicating the onset of inelasticity in the scattering channel. However, we have verified that there is a negligible difference in the resulting parameter fits when fitting phase shifts up to 215 MeV versus a maximum value of 300 MeV. The parametrizations of the P_{11} and P_{33} phase shift data are shown in Fig. 5.9. We note that the phase shift is much larger in the P_{33} channel than in the P_{11} channel. This difference is important to our fits.

As an aid to fit our parameters to the phase shifts, we seek to minimize the integrated difference between our K-matrix phase shift and the data fit from Ref [8]. We define this difference to be

$$D = \int_0^{k_{\rm max}} dk \left\{ \left[\delta_{11}^{data}(k) - \delta_{11}^{RIKM}(k)\right]^2 + \left[\delta_{33}^{data}(k) - \delta_{33}^{RIKM}(k)\right]^2 \right\} , \qquad (5.47)$$

where k is the magnitude of the center-of-mass momentum, δ^{data} is the phase shift fit from Ref. [8], and δ^{RIKM} is our phase shift calculated using the RIKM model. In Fig. 5.10 we display the results for the fits that result from optimizing the parameters for just one channel at a time. We see that the parameter combination which provides

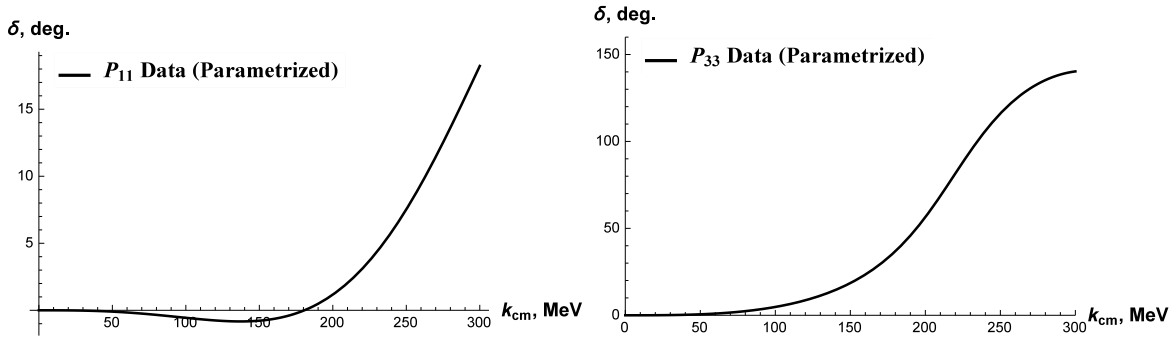

(a) P_{11} channel (b) P_{33} channel

Figure 5.9: Fits to phase shift data in the P_{11} (left panel) and P_{33} (right panel) channels from Ref. [8].

an optimal fit in one channel results in a rather poor fit in the other channel. This suggests that we need to find a suitable balance of parameter values which adequately satisfies both channels. We show the simultaneous fit of both channels given by Eq. (5.47) in Fig. 5.11 (a) and (b). This displays why it is important to recognize the vertical axis scale difference in the P_{11} and P_{33} plots. While both channels have been evaluated on an equal basis, since the P_{33} channel phase shift varies from 0 to $\approx 150^\circ$ while the P_{11} channel phase shift varies from 0 to $\approx 20^\circ$, it appears that the P_{11} channel has a worse fit than the P_{33} channel. To illustrate this effect, we have plotted both channels' phase shifts in Fig. 5.11(b).

Fig. 5.10 (a) displays a problem with our fit which should be addressed. Our fit does not display the attractive negative phase shift in the P_{11} channel at momenta smaller than ≈ 180 MeV which is evident in the data. We can remedy this issue by giving a greater weight to the P_{11} channel in Eq. (5.47). If we weight the P_{11} channel a factor 10 more than the P_{33} channel, the only parameter that changes is $\Lambda_{\pi B_1 B_2}$, which increases from 520 MeV to 920 MeV. This results in the fits shown in

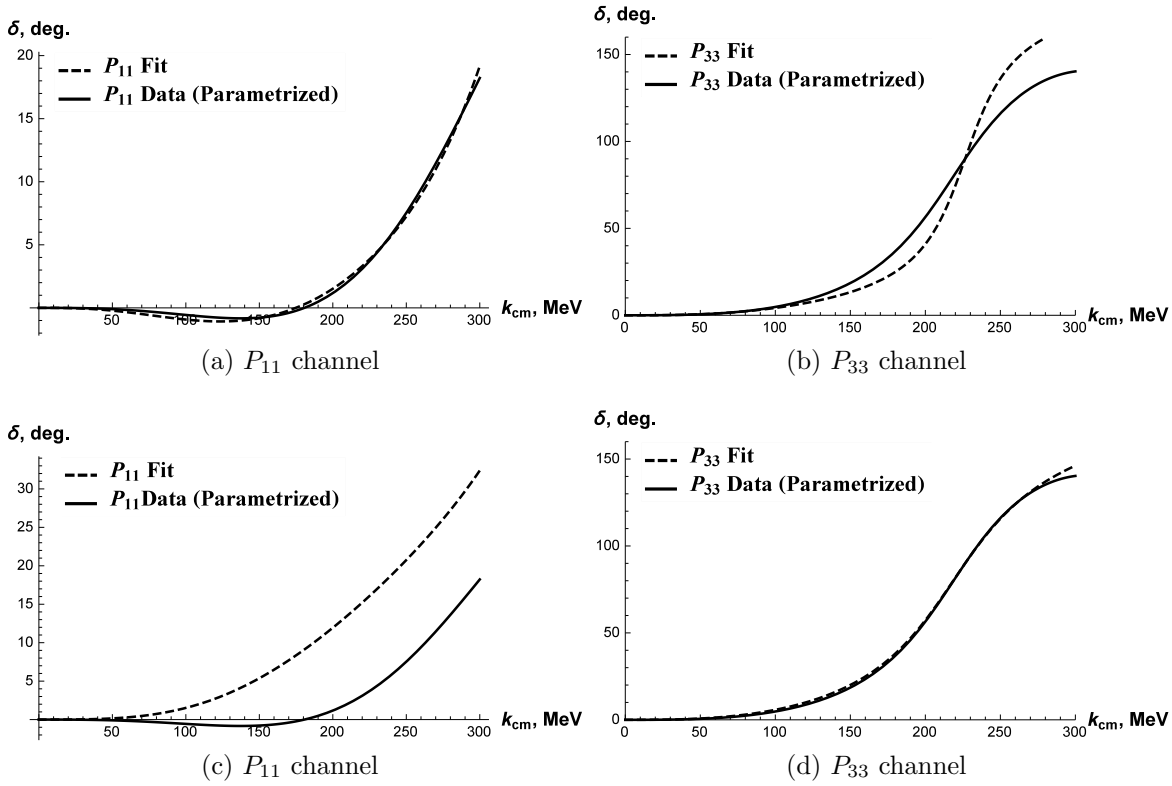

(a) P_{11} channel (b) P_{33} channel

(c) P_{11} channel (d) P_{33} channel

Figure 5.10: Phase shifts with parameters fit to P_{11} data only (top row) and with parameters fit to P_{33} data only (bottom row).

Figs. 5.10 (c) and (d). This shows that we achieve the wanted attraction in the P_{11} channel at the cost of the fit in the P_{11} channel. We shall use the parameters from the fit shown in Fig. 5.11 (c) and (d) for our calculations, i.e., $\Lambda_{\pi B_1 B_2} = 920$ MeV. However, since couplings and form factors enter into the rates as $f^2 F F^2$, changing the form factor cutoff causes a compensatory effect on the couplings. We have found that the resulting seesaw effect yields a negligible difference in our rates when using a value of $\Lambda_{\pi B_1 B_2} = 520$.

To evaluate the ωNN coupling and form factor cutoff, we calculate the contribution to the $\gamma p \to \pi N$ cross section from an ω t-channel exchange. This process

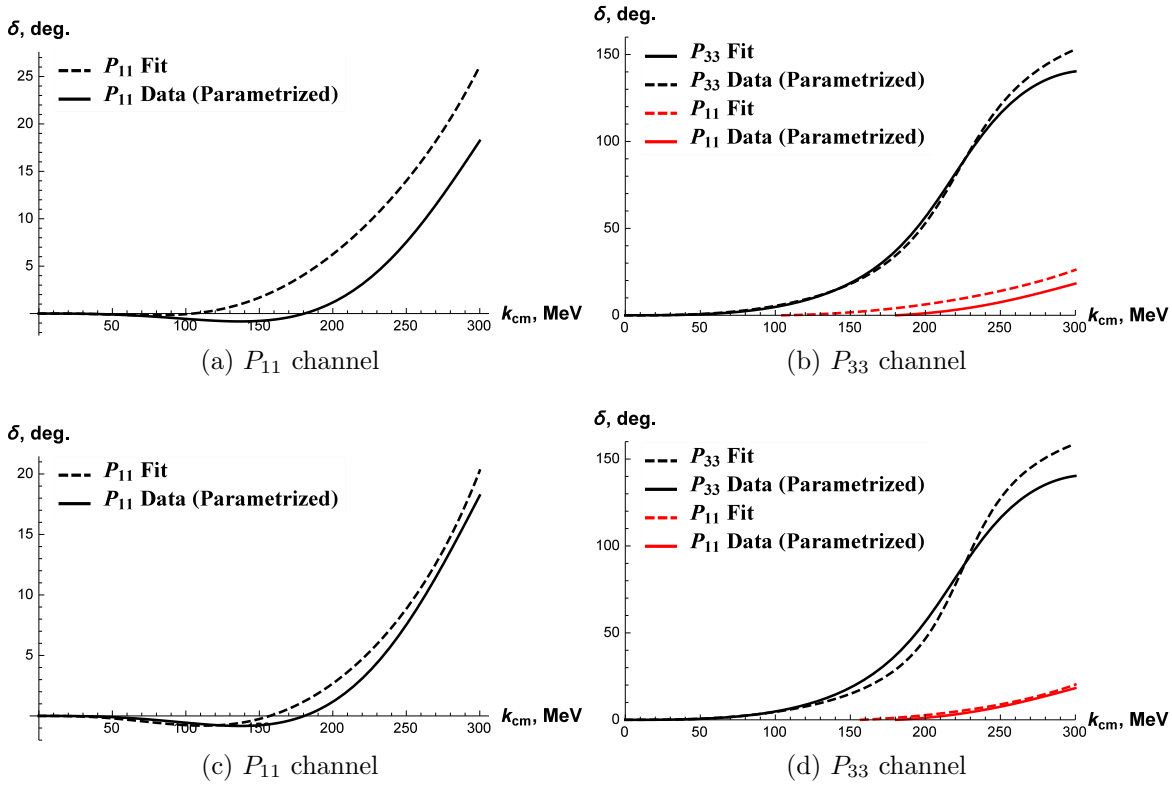

(a) P_{11} channel (b) P_{33} channel

(c) P_{11} channel (d) P_{33} channel

Figure 5.11: Phase shifts with parameters simultaneously fit to both channels (top row), and phase shifts with parameters fit to both channels with weighting toward the P_{11} channel (bottom row).

contains the coupling $g_{\omega NN}$ and the form factor cutoff $\Lambda_{\omega NN}$, which allows us to evaluate both parameters. The resulting photoabsorption cross section is added to the total proton photoabsorption cross section calculated using the low-density limit of the ρ-meson spectral function from Ref. [5]. We choose a conservative value [107] of $g_{\omega NN} = 11$. We then find the maximal value of $\Lambda_{\omega NN}$ that yields a total cross section compatible with proton photoabsorption data.

The results for $\Lambda_{\omega NN} = 500$ MeV and 750 MeV are shown in Fig 5.12. Here we see that the total photoabsorption cross section using the 500 MeV cutoff is at

	P_{11} Only Fit	P_{33} Only Fit	Simultaneous Fit	Weighted Fit
$f_{\pi NN}$	1.1	0.9	1.1	1.1
y	0.69	0.6	0.6	0.6
$\Lambda_{\pi N\Delta}$	310	360	360	360
$\Lambda_{\pi BB}$	1360	410	520	920

Table 5.2: Parameter combinations for partial wave channel fits.

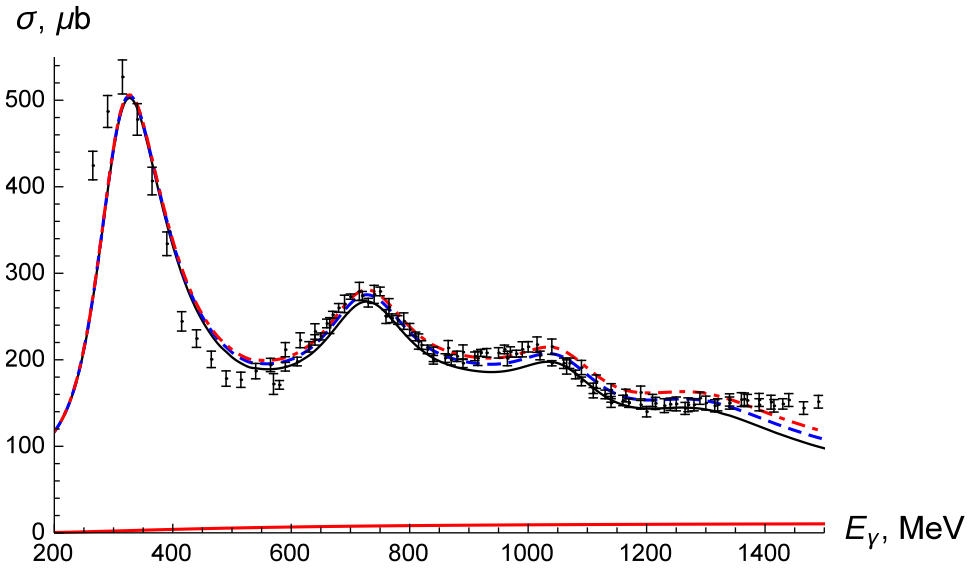

Figure 5.12: Proton photoabsorption cross section calculations excluding ω t-channel exchange [5] (solid black line), including the t-channel exchange with $\Lambda_{\omega NN} = 500$ MeV (dashed blue line), and with $\Lambda_{\omega NN} = 750$ MeV (dot-dashed red line). The lower solid red line is the isolated ω t-channel contribution with $\Lambda_{\omega NN} = 500$ MeV. Data are from Refs. [6, 7].

the higher end of the error bars in the 1100–1300 MeV photon energy range, and is compatible with the data for other energies. The 750 MeV cutoff sightly exceeds the data in the 1100–1300 MeV photon energy range. Therefore, we choose $\Lambda_{\omega NN} = 500$ MeV. For simplicity, we also assume this value for all ωNN^* form factor cutoffs. Fig 5.12 also shows the individual contribution to the photoabsorption cross section

from the ω t-channel exchange alone to demonstrate its relatively slow growth as a function of photon energy. The t-channel exchange contribution reaches half its maximum value of ≈ 11 μb at a photon energy of $E_\gamma \approx 500$ MeV, and reaches its maxinal value at $E_\gamma \approx 2000$ MeV. This suggests that contributions from processes of $\gamma p \to \pi N^*$ via ω t-channel exchange do not become appreciable until photon energies reach several hundred MeV higher than the πN^* production threshold[4]. The lowest-lying resonance we consider in this process is the $N(1440)$, which has a πN^* production threshold of ≈ 860 MeV. Therefore, contributions to resonance production processes via proton photoabsorption that are mediated by an ω t-channel exchange are negligible to the energy range considered in Fig. 5.12. In principle, we could also use the process $\gamma p \to \omega p$ to constrain the form factor cutoff. However, the ωp production threshold is ≈ 1100 MeV, so it too is negligible in the photon energy range considered here.

This completes our evaluation of free parameters in our photoemission model. The resulting coupling constants are collected in Appendix D. We may proceed to calculations of thermal photon emission rates.

5.3 Photon Emission from $\pi\pi$ Cloud

Here we present our photon emission rates which correspond to modifications of the pion cloud of the ρ meson. In order to examine the impact of each process individually, we first display rates for a temperature of 150 MeV and zero baryon chemical potential, where we multiply the resulting rates by a factor 2 to account for the effect of anti-baryons. We arrange our rates by partial wave channel, i.e., whether the $\pi B_1 B_2$ interaction is an S-, P-, or D-wave. Our S-wave results are shown in Fig. 5.13. We immediately see a trend where, in the photon energy range

[4]The $\pi\Delta$ production threshold is irrelevant since the ω is an isospin-0 state and cannot excite the nucleon's isospin state.

of 0.2–0.5 GeV, processes involving more massive baryons in the initial state have relatively large photon emission rates (exothermic processes). We also see that photon rates from processes involving more massive baryons in the final state (endothermic processes) are heavily suppressed in this low energy range. This is due to the phase space favoring a highly energetic final state when the initial state contains a large amount of invariant mass. These same processes also dominate at photon energies above ≈ 1 GeV for the same reason.

Fig. 5.13 also shows an interesting trend where the high-q_0 behavior of the rates seems to be dominated by the final-state baryon. Take for example the processes $\pi N(1535) \rightarrow \gamma N(940)$ and $\pi N(1650) \rightarrow \gamma N(940)$ shown in Fig. 5.13 (a). The $N(1535)$ and $N(1650)$ share the same quantum numbers, so their spin/isospin degeneracy factors are identical. Their couplings are also approximately equal, so the only difference in their rates should be from their differing masses. The rates for these two processes are essentially degenerate for $q_0 \gtrsim 2.0$ GeV. This can be explained very roughly as follows. When typical momenta in the scattering processes are small, then the thermal factor $f(E_1)f(E_2)[1 - f(E_3)]$ is dominated by the mass of the particles.

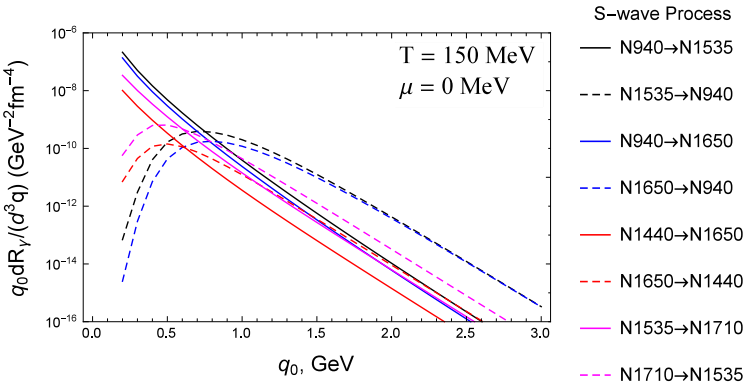

(a) S-wave Nucleons

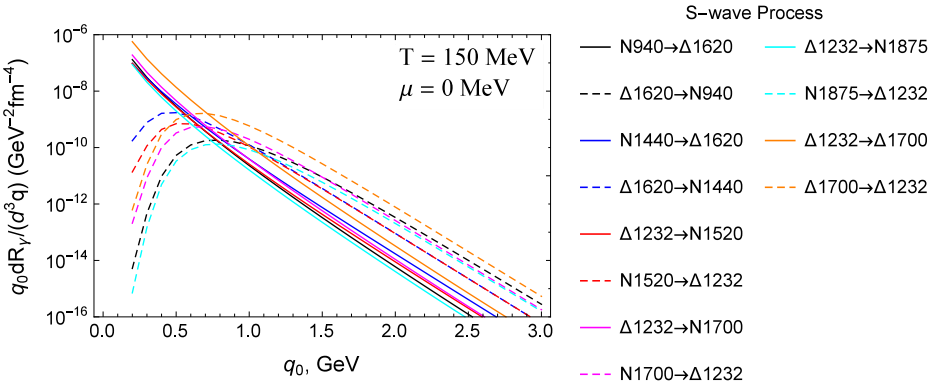

(b) S-wave Deltas

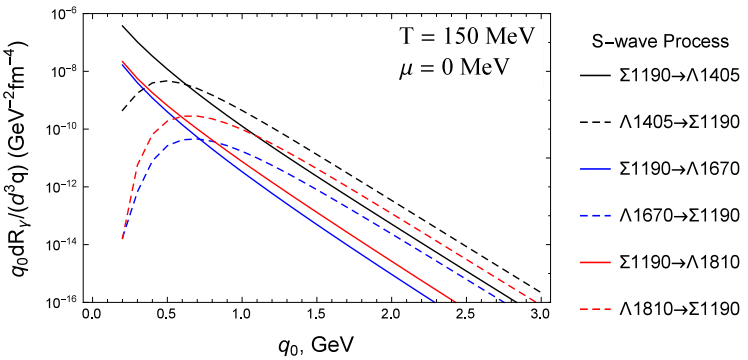

(c) S-wave Hyperons

Figure 5.13: S-wave photon production processes.

This also corresponds to the lower end of photon energies, which is where we observe the rates differing as a result of the ≈ 100 MeV mass difference of the $N(1535)$ and $N(1650)$. However, then typical momenta are high, the energies $E = \sqrt{m^2 + p^2}$ in the thermal factors are driven by the momenta. At this point the mass differences are "washed out" by the momenta, and the thermal factors will be driven by purely momentum effects.

To check this hypothesis, we can examine a processes with a mass close to the $N(1535)$ or $N(1650)$, but with different quantum numbers, and thus different degeneracy. In Fig. 5.13 (b) we have the $\pi\Delta(1620) \to \gamma N(940)$ process. The combined spin/isospin factor[5] for this process is 16/3, while for the $N(1650)$ process the spin/isospin factor is 8. Since the masses are approximately equal, we expect that, for high q_0, the $\Delta(1620)$ process should be smaller by a factor of 2/3. Inspection of the plots reveals this to be the case; at $q_0 = 3$ GeV, the $\Delta(1620)$ rate has a value of (ignoring units) $6.2\,\mathrm{x}\,10^{-15}$, while the $N(1650)$ rate has a value of $9.3\,\mathrm{x}\,10^{-15}$.

Additionally, Fig. 5.13 (c) shows the contribution from S-wave hyperon interactions, which have been mostly ignored in previous works. While these processes have smaller isospin degeneracies than non-strange baryons, in the phenomenological region of interest around $q_0 \approx 1$ GeV, we see they have a significant contribution compared to the nucleons and Δs. Much of this is due to the non-negligible size of their coupling constants, as shown in Table D.5 in App. D.

We now proceed to the P-wave processes, shown in Figs. 5.14 and 5.15. We first note the greater number of P-wave processes as compared to S-wave processes. This alone suggests the P-wave interaction may have a greater contribution to the overall rates. We also find that the size of the P-wave rates in general are greater than

[5]We note that the spin/isospin factor is NOT equal to the particle degeneracy; see Sec. A for details.

the S-wave. Inspecting the individual plots, Fig. 5.14 (a) shows that the $\pi N \to \gamma N$ process is quite large, as expected. However, the $\pi N(1440) \to \gamma N$ process begins to exceed it at $q_0 \approx 1$ GeV. This has several reasons. While the $\pi NN(1440)$ coupling is half that of the πNN, the increased amount of mass in the initial state has an extra 500 MeV available to be injected into the final state. However, this is mitigated by the increased thermal penalty for that mass. More importantly, while the πNN form factor cutoff is constrained to be 310 MeV, we recall the cutoff value for our $\pi B_1 B_2$ form factors is 920 MeV. This harder form factor generates less suppression than in the $\pi N \to \gamma N$ process.

Figs. 5.14 (b) displays an expected result: the $N \leftrightarrow \Delta$ processes dominate. This is mainly due to the large $\pi N\Delta$ coupling and relatively small masses of the particles, which gives these processes a generous phase space. Figs. 5.15 (a) shows a significant unexpected result, namely that of the size of the rates from the $N(1440) \leftrightarrow \Delta(1600)$ processes, using the coupling we calculated in Sec. 5.2.5 by using the $N(1440)$ spectral function. We found that the $\pi N(1440)\Delta(1600)$ coupling has a relatively large value of $f_{\pi N(1440)\Delta(1600)} = 4.9$, which is 60% larger than the $\pi N\Delta$ coupling. Since couplings enter into the rates squared, this gives a relative increased of a factor ≈ 2.5 over the $N \leftrightarrow \Delta$ processes. While this is somewhat mitigated by the thermal suppression from larger masses, this is a novel result that, to the author's knowledge, has not before been encountered in the area of thermal photon emission. A similar result is seen in the processes involving $f_{\pi\Delta N(1440)} = 1.785$. Additionally, the $\Delta \leftrightarrow \Delta(1600)$ and $\Delta \leftrightarrow N(1720)$ processes are sizeable as a result of the large spin/isospin factors resulting from spin- and/or isospin-3/2 particles in both the initial and final states. Finally, we see that the contributions from P-wave hyperons are smaller than the nucleons and Δs, but are not negligible.

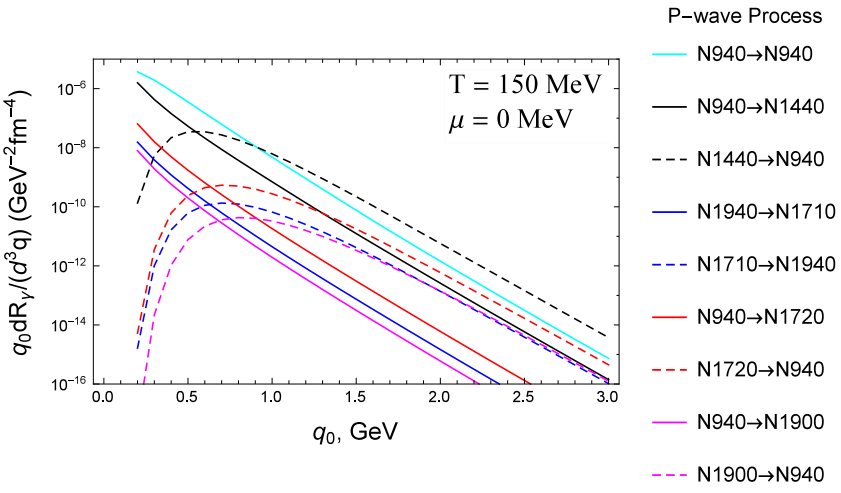

(a) P-wave Nucleons

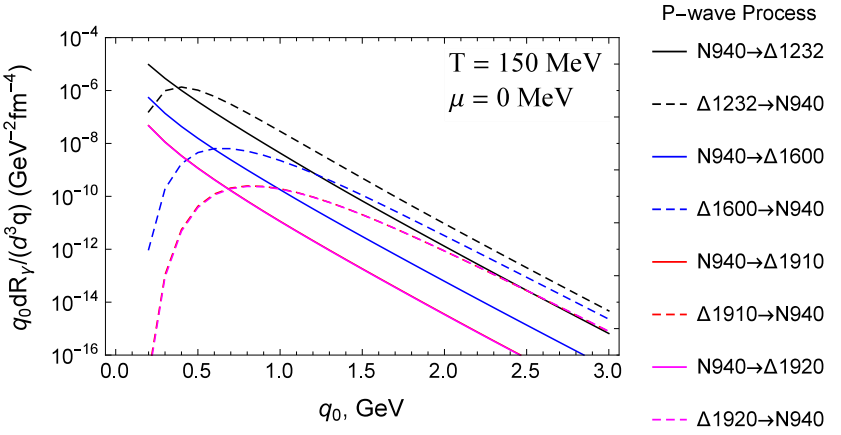

(b) P-wave Deltas+N940

Figure 5.14: First table of P-wave photon production processes.

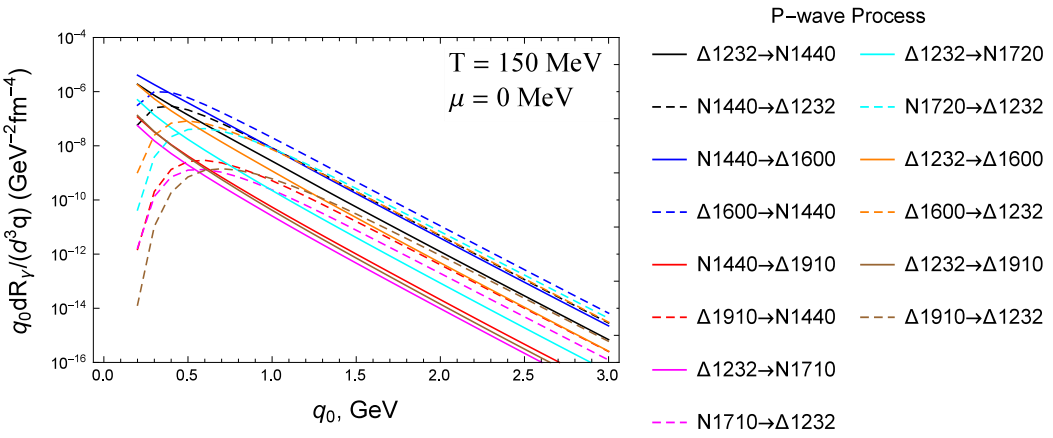

(a) P-wave Deltas and Nucleon Resonances

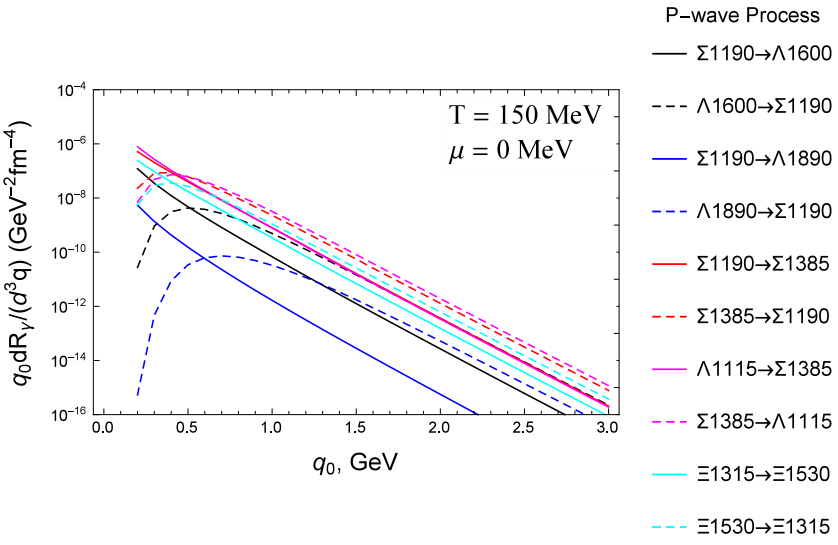

(b) P-wave Hyperons

Figure 5.15: Second table of P-wave photon production processes.

Our final contribution from the $\pi\pi$ cloud comes from D-wave processes, shown in Fig. 5.17. We first see that the contribution from the D-wave hyperons is smaller than from the nucleons or Δs by more than two orders of magnitude, and are thereby negligible. Therefore, we will neglect their contribution to the overall rates from this point on. Secondly, for $q_0 > 1$ GeV, we see that the size of the D-wave nucleon and Δ rates are comparable to the P-wave rates. This is somewhat to be expected, since both P- and D-wave interactions involve non-zero powers of momenta, albeit with different form factors.

The total pion cloud contributions are collected by partial wave and shown in Fig. 5.17. We compare the rates to those from the in-medium ρ spectral function mentioned in Sec. 5.1 and parametrized in Ref. [4]. The ratio between our total pion cloud rates and the ρ spectral function is also shown in Fig. 5.17. At close to the pseudo-critical temperature of $T = 150$ MeV and at vanishing baryon chemical potential, our pion cloud rates are $\approx 17\%$ of the ρ spectral function at $q_0 = 1.0$ GeV. This suggests that, at zero density, the photon rates from the ρ spectral function are dominated by meson effects and radiative decays of baryon resonances.

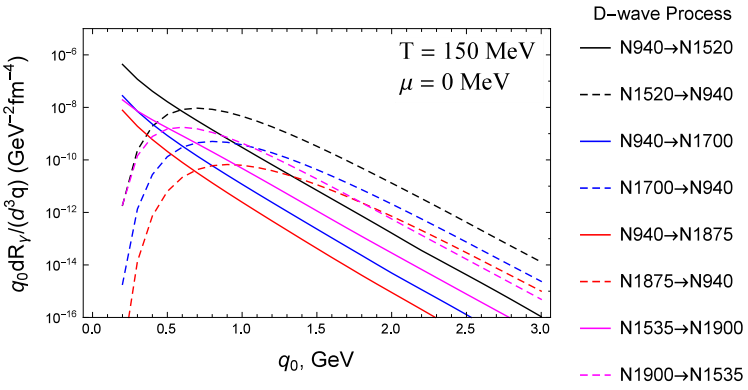

(a) D-wave Nucleons

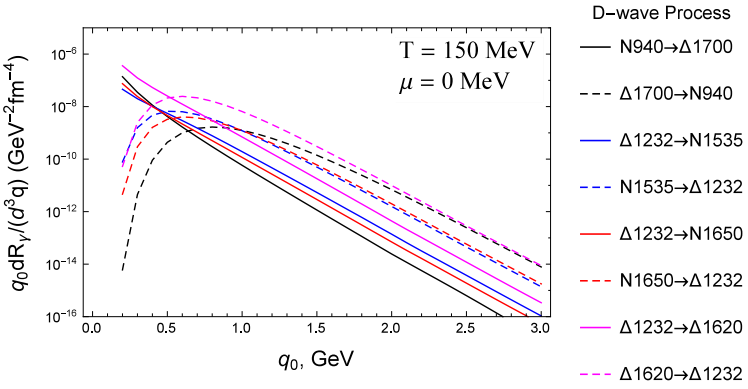

(b) D-wave Deltas

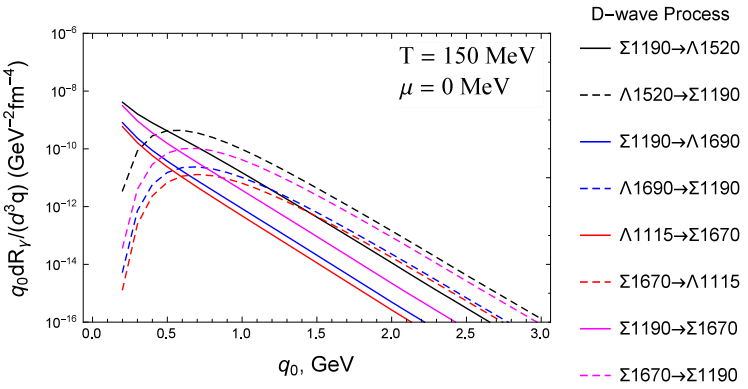

(c) D-wave Hyperons

Figure 5.16: D-wave photon production processes.

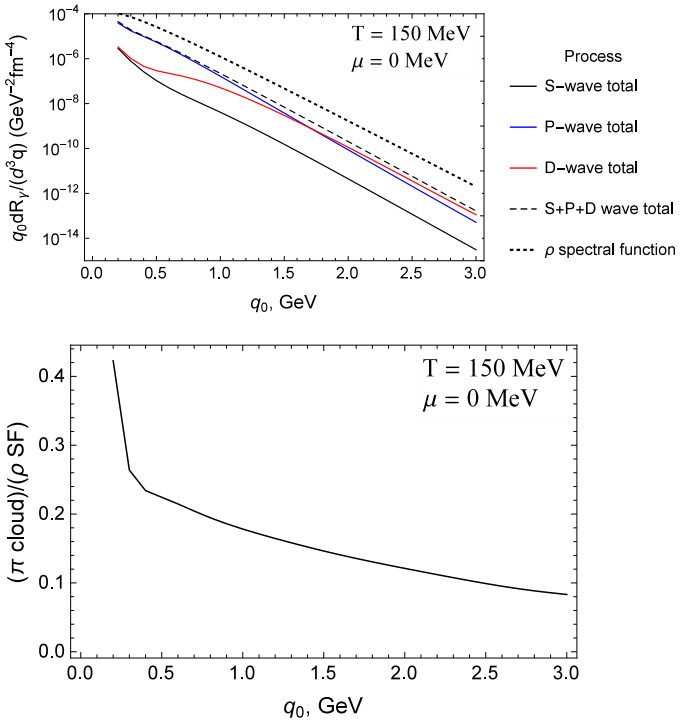

Figure 5.17: Thermal photon rates from $\pi\pi$ cloud modifications (top) and ratio of $\pi\pi$ cloud rates to rates from ρ spectral function (bottom).

5.4 Photon Emission from $\pi\omega$ Cloud

We now move on to contributions from the $\pi\omega$ cloud of the ρ meson. As mentioned above, save for $\omega N \to \gamma N$, these processes are novel contributions to thermal photons rates.

5.4.1 Incoming π

Processes involving an incoming pion together with an ω t-channel exchange correspond to cuts of the $\pi\omega$ cloud of the ρ spectral function as shown at the beginning of this chapter in Fig. 5.2 (a). Since the emitted photon is attached to the $\pi\rho\omega$ vertex, this process is gauge invariant by itself, without the need to consider any other diagrams. These processes all involve an $\omega N N^*$ vertex. In the present work

we only have values for these couplings for 9 N^* resonances, so the baryon spectrum we have is not as complete as for πNN^* coupling. The resulting rates for the ω t-channel exchanges are shown in Fig. 5.18. We immediately see the effect of the different sizes of the ωNN^* coupling constants on the rates. Since the couplings enter into the rates squared, the process including the coupling $g_{\omega NN} = 11$ dwarfs all other processes, whose couplings are all less than 3. Since these rates are all several orders of magnitude smaller than the other baryonic contributions, we will neglect them and keep only the result from the $\pi N \to \gamma N$ ω t-channel process.

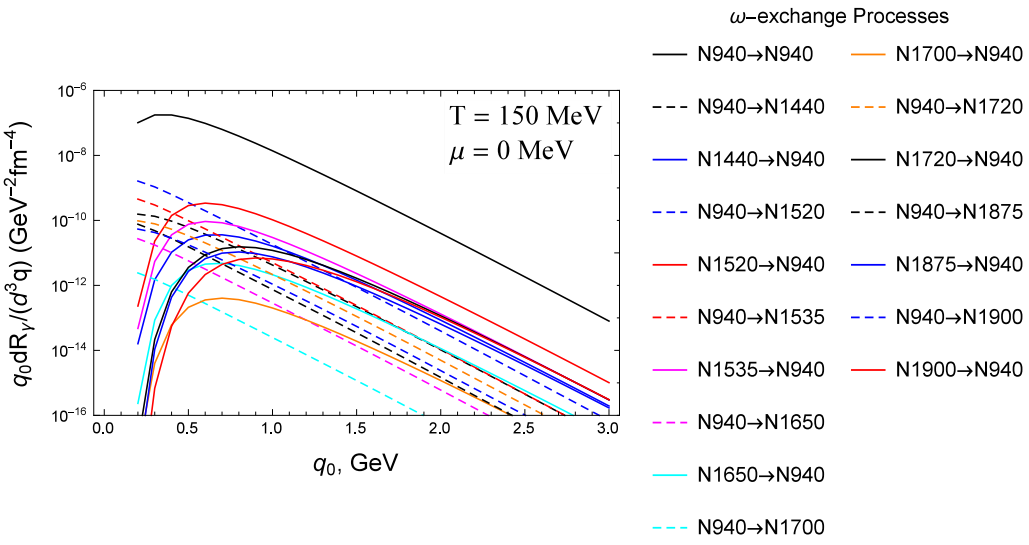

Figure 5.18: Thermal photon emission rates from processes involving t-channel ω exchange.

5.4.2 Incoming ω

We now move on to the second contribution from the $\pi\omega$ cloud, shown in Fig. 5.2 (b). This cut to the $\pi\omega$ cloud of the ρ spectral function corresponds to a scattering process of $\omega B_1 \to \gamma B_2$ via a t-channel pion exchange. As with the above processes

involving a t-channel ω exchange, this process involves photon emission from the $\pi\rho\omega$ vertex, and is thus gauge invariant by itself without the need for other diagrams. This process is topologically similar to the processes generated by the $\pi\pi$ cloud and only involves swapping the $\rho\pi\pi$ vertex for the $\pi\rho\omega$ vertex. This yields a new set of processes, all involving the same combinations of baryons as considered in Sec. 5.3. While these new processes are more suppressed by the ω mass in the exchange propagator, they also receive a significant boost from the large size of the $\pi\rho\omega$ coupling constant. We therefore anticipate their contribution to the overall photon rate to be appreciable.

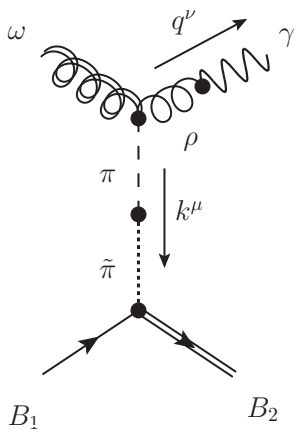

Figure 5.19: Feynman diagram of photon emission processes involving ω mesons as external particles.

Before we move on to the rates, let us first reexamine the Feynman diagram for this process, shown in Fig. 5.19. This process has the same topological configuration as the u-channel process in Fig. 4.2 from Sec. 4. Recall that process was the one where the exchanged pion could go on shell, which double-counted the ω radiative decay. This same problem shows itself in Fig. 5.19. If the incoming baryon is less

massive than the outgoing baryon by at least the pion mass, the exchanged pion can go on shell. We then have two separate processes, an $\omega \to \pi^0\gamma$ radiative decay, and a $B_1 \to \pi B_2$ absorption, all involving on-shell particles. However, we recall that thermal field theory gave us the solution to this problem, which involved excluding the Landau cut of the ρ self-energy. We shall use that solution here; we apply the same kinematic restriction of $E_\omega < q_0$ to the KT integration range. As before, his precludes the possibility of the exchange pion going on-shell.

Since we again have a considerable number of processes, we will only plot the rates of several of the processes with the lightest external baryons, then analyze the total. These are displayed in Fig. 5.20. We first note the effect of the kinematic restriction of $E_\omega < q_0$. This removes the low-q_0 range from the $\omega N \to \gamma\Delta$ process, causing it to have no contribution for photon energies less than 1 GeV. This is the same behavior displayed by the kinematic restriction (or equivalently, the Landau cut) in Fig. 4.5 of Sec. 4. Second, we note the sizes of the individual processes. For comparison, we have also plotted the process $\pi N \to \gamma N$ as calculated in Sec. 5.3. We see that in the phenomenologically relevant range near $q_0 \approx 1$ GeV, the $\omega N \to \gamma N$ process is not far below the $\pi N \to \gamma N$, suggesting its possible impact on the overall rates. This is due to the large size of the $\pi\rho\omega$ coupling constant overcoming the increased phase space suppression from the ω as an external particle as compared to the pion. Third, we see that at energies above $q_0 \approx 1$ GeV, the incoming ω processes rapidly gain strength, as expected from an exothermic process. This indicates that the total rate from the external ω processes may be significant at high photon energies.

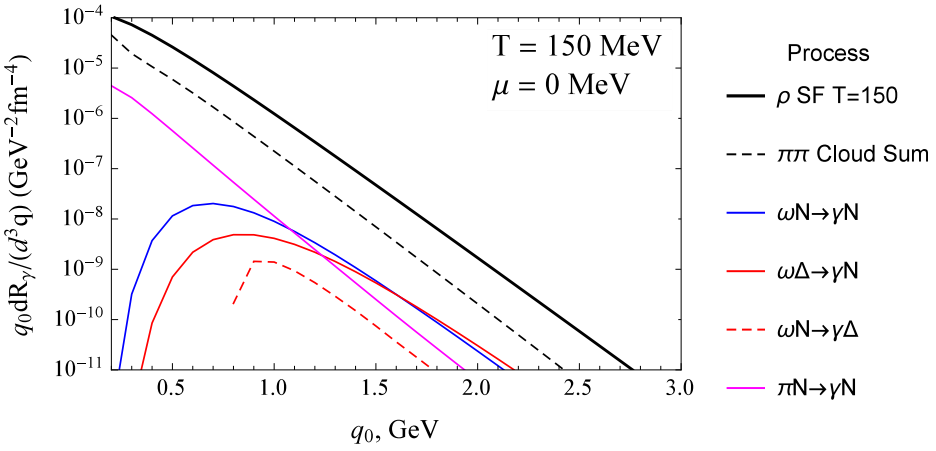

Figure 5.20: Thermal photon rates from processes involving an external ω particle.

5.5 Results and Comparison to Existing Rates

We now analyze our total rates from both the $\pi\omega$ cloud and the $\pi\pi$ cloud. We compare these rates to the in-medium ρ spectral function in Fig. 5.21. As anticipated earlier, the effect of the $\pi\omega$ cloud processes is quite evident at photon energies $q_0 \gtrsim 1.0$ GeV. At $q_0 = 1.0$ GeV the inclusion of $\pi\omega$ cloud effects lifts the total from 17% with just the $\pi\pi$ cloud to 23%. This effect increases with photon energy: at $q_0 = 2.0$ GeV, we have 12% $\rightarrow$ 30%, and at $q_0 = 3.0$ GeV, we have 8% $\rightarrow$ 31%. Therefore, for photon energies over 1 GeV, the effect of the $\pi\omega$ cloud is substantial.

In addition, we can estimate the size of the contribution of our $\pi\pi$ cloud calculations with those of the ρ spectral function. In Ref. [84], the left-hand panel of Fig. 3 separates out the individual contributions to the spectra function at $T = 150$ MeV and $\mu_B = 340$ MeV. At a photon energy of $q_0 = 1.0$ GeV, we take the difference of the value of the full spectral function and the spectral function with no baryons. This gives us the baryonic contribution, and the value is ≈ 1 x 10^{-6} fm^{-4} GeV^{-2}. This is approximately split evenly between pion cloud effects and direct ρBB interaction

effects [5]. Therefore the estimated contribution from the pion cloud is 5 x 10^{-7}. By direct calculation of our pion cloud, we find the rate at the same temperature, density, and photon energy to be 9.76 x 10^{-7}. This indicates that at $q_0 = 1.0$ GeV we have found a 100% enhancement of pion cloud rates, which is a 50% enhancement of baryonic rates, resulting in a 25% enhancement of the overall photon rate of the ρ spectral function.

We now examine our results to the ρ spectra function at chemical freezeout conditions of $T = 160$ MeV and $\mu_B = 240$ MeV. This is shown in Fig. 5.22. We see that the increase in baryon chemical potential has substantially increased the relative effects of the baryons in the ρ spectral function. Additionally, the process $\pi N \to \gamma N$ with an ω t-channel exchange has increased relative to the total rates.

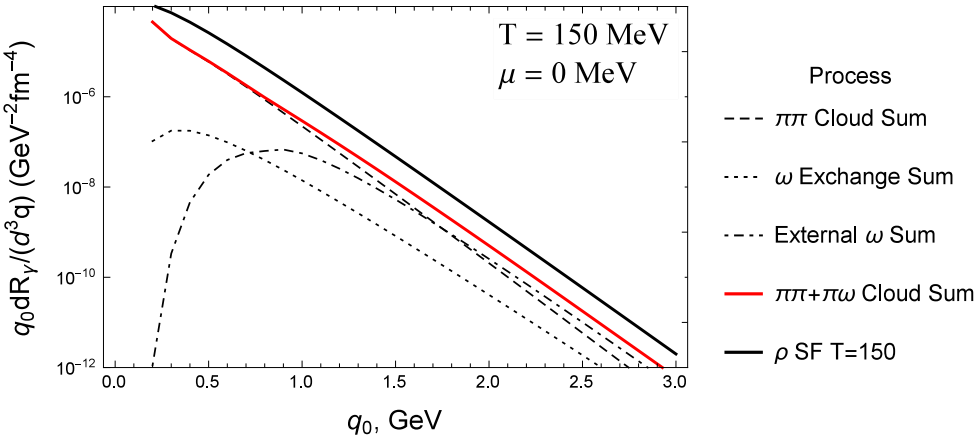

(a) $\pi\pi$+$\pi\omega$ Cloud Rates

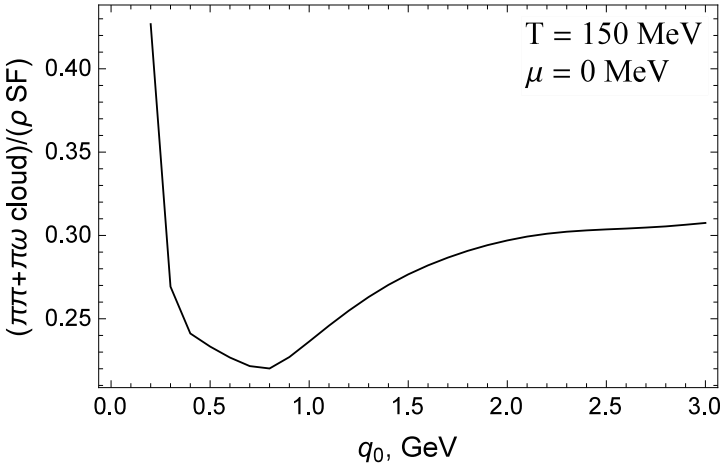

(b) Ratio of $\pi\pi$+$\pi\omega$ Cloud Rates to ρ Spectral Function Rates

Figure 5.21: Total thermal photon rates from the $\pi\pi$ cloud, the $\pi\omega$ cloud, and their sum as compared to rates from the in-medium ρ spectral function (top). Ratio of rates from both $\pi\pi$ and $\pi\omega$ cloud to rates from the in-medium ρ spectral function (bottom).

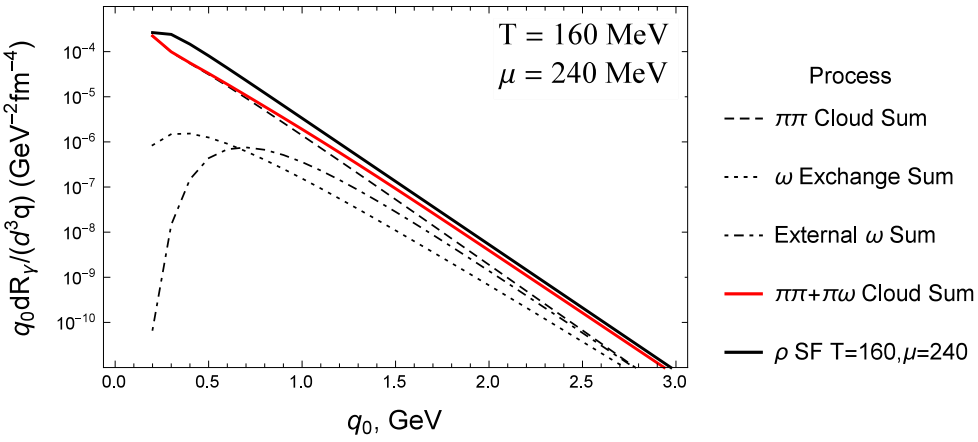

(a) $\pi\pi$+$\pi\omega$ Cloud Rates

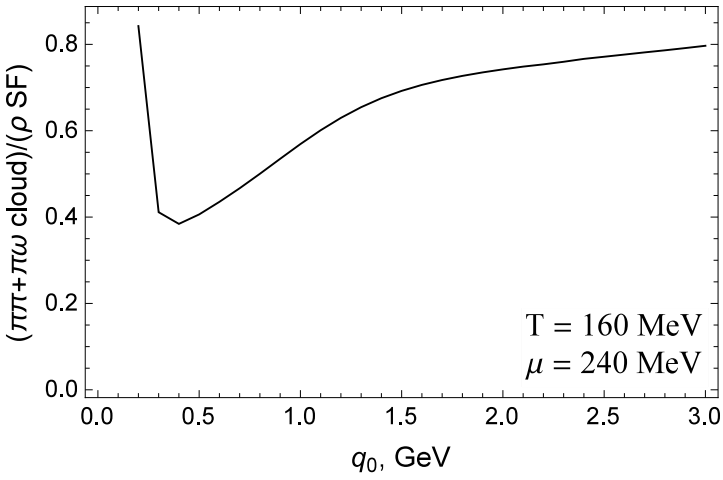

(b) Ratio of $\pi\pi$+$\pi\omega$ Cloud Rates to ρ Spectral Function Rates

Figure 5.22: Total thermal photon rates from the $\pi\pi$ cloud, the $\pi\omega$ cloud, and their sum as compared to rates from the in-medium ρ spectral function (top). Ratio of rates from both $\pi\pi$ and $\pi\omega$ cloud to rates from the in-medium ρ spectral function (bottom).

5.6 Discussion and Summary

In this chapter we have revisited the thermal photon rate calculation from an in-medium ρ spectral function by using relativistic kinetic theory. We have checked the previously-estimated effects from baryon interactions in the $\pi\pi$ cloud by explicit calculation and found it to be a slight underestimate. In addition, we identified a novel source of thermal photons in the form of interactions with an ω meson, both as a t-channel exchange particle and as an external particle in $\omega B_1 \to \gamma B_2$ scattering processes. The contributions to photon rates from these new processes turned out to be non-negligible for photon energies of $q_0 \gtrsim 1.0$ GeV, even exceeding the contributions from the $\pi\pi$ cloud at high photon energies. These novel processes are substantial enough to warrant their inclusion in further calculations of thermal photon spectra and elliptic flow.

6. CONCLUSION AND OUTLOOK

In this work, we have explored the properties of QCD matter at finite temperature and densities. We first examined the behavior of the spectral distributions of the isovector-vector and isovector-axial-vector spectral functions at low temperatures ($T \lesssim m_\pi$) and zero density by using the finite-temperature QCD and Weinberg-type sum rules. By implementing a strict leading-order-in-temperature expansion and approximating the thermal medium as a dilute pion gas, we found that, while the WSRs were analytically satisfied, the QCDSRs were analytically violated by a finite pion mass. We then numerically measured the size of this violation and found it to be small for temperatures less than the pion mass. Above this temperature, the QCD sum rule violation grows to the extent that it can no longer be considered satisfied, probably indicating the breakdown of the thermal medium model. Further improvements on this analysis could include more elaborate spectral function models which go beyond simple chiral mixing, as well as incorporating finite-density effects. In fact, work in this direction has already been carried out in Ref. [125], where it was found that the scenario of a ρ meson which broadened and "melted" away with increasing temperature and density was compatible with the restoration of chiral symmetry.

We then revisited thermal photon emission rates from a hadronic source, beginning with a system composed of π, ρ, and ω mesons. These rates were anticipated to be non-negligible due to both the large size of the $\pi\rho\omega$ coupling constant and due to the relatively small particle masses involved. In the process of calculating these rates using relativistic kinetic theory, we encountered a problem wherein a non-integrable singularity occurs, which also implies a double-counting of a previously-considered

contribution, that of the $\omega \to \pi^0\gamma$ radiative decay. We resolved this problem by turning to an alternative framework for the calculation of photon rates, that of thermal field theory. Within this framework, we were able not only to identify a criterion to avoid double-counting, but also to verify the equivalence of both calculation frameworks. After accounting for finite-size effects, we found the photo-emission rates from the $\pi\rho\omega$ system to be significant compared to existing total hadronic emission rates.

Finally, we calculated the photo-emission rates from baryonic contributions. We constructed a microscopic framework consisting of a non-relativistic expansion of phenomenological Lagrangians and accounted for finite-size effects by implementing form factors in a gauge-invariant manner. The parameters were evaluated by using resonance decay branchings, proton photoabsorption cross sections, and elastic πN scattering phase shift data. We compared these rates to the corresponding ones given by the $\pi\pi$ cloud of an in-medium ρ spectral function. We found that the newly-calculated contributions increase previous estimates from the ρ spectral function, especially with rising baryon chemical potential. The implementation of these new contributions into the ρ spectral function is thus an important future task. Additionally, we identified another novel source of photons equivalent to a $\pi\omega$ cloud modification of the ρ spectral function. These rates were found to be non-negligible as well, again benefitting from the large $\pi\rho\omega$ coupling constant.

These thermal photon rate calculations both improve the accuracy of the current state-of-the-art calculations, and augment them by adding previously unaccounted-for rates. These rates should be included in any further calculations of thermal photon spectra and v_2, and as such, should help to alleviate the "photon puzzle."

REFERENCES

[1] P. M. Hohler and R. Rapp. Sum rule analysis of vector and axial-vector spectral functions with excited states in vacuum. *Nucl. Phys.*, A892:58–72, 2012.

[2] N. P. M. Holt, P. M. Hohler, and R. Rapp. Quantitative sum rule analysis of low-temperature spectral functions. *Phys. Rev.*, D87:076010, 2013.

[3] W. Liu and R. Rapp. Low-energy thermal photons from meson-meson bremsstrahlung. *Nucl. Phys.*, A796:101–121, 2007.

[4] M. Heffernan, P. Hohler, and R. Rapp. Universal parametrization of thermal photon rates in hadronic matter. *Phys. Rev.*, C91(2):027902, 2015.

[5] R. Rapp. private communication, 2016.

[6] T. A. Armstrong et al. Total hadronic cross-section of gamma rays in hydrogen in the energy range 0.265-GeV to 4.215-GeV. *Phys. Rev.*, D5:1640–1652, 1972.

[7] O. Bartalini et al. Measurement of the total photoabsorption cross section on a proton in the energy range 600-MeV - 1500-MeV at the GRAAL. *Phys. Atom. Nucl.*, 71:75–82, 2008.

[8] R. L. Workman, R. A. Arndt, W. J. Briscoe, M. W. Paris, and I. I. Strakovsky. Parameterization dependence of T matrix poles and eigenphases from a fit to πN elastic scattering data. *Phys. Rev.*, C86:035202, 2012.

[9] K. A. Olive et al. Review of particle physics. *Chin. Phys.*, C38:090001, 2014.

[10] Georges Aad et al. Observation of a new particle in the search for the Standard Model Higgs boson with the ATLAS detector at the LHC. *Phys. Lett.*, B716:1–29, 2012.

[11] Serguei Chatrchyan et al. Observation of a new boson at a mass of 125 GeV with the CMS experiment at the LHC. *Phys. Lett.*, B716:30–61, 2012.

[12] D. J. Gross and F. Wilczek. Asymptotically free gauge theories. 1. *Phys. Rev.*, D8:3633–3652, 1973.

[13] H. D. Politzer. Reliable perturbative results for strong interactions? *Phys. Rev. Lett.*, 30:1346–1349, 1973.

[14] E. V. Shuryak. The QCD vacuum, hadrons and the superdense matter. *World Sci. Lect. Notes Phys.*, 71:1–618, 2004. [World Sci. Lect. Notes Phys.8,1(1988)].

[15] R. Rapp, J. Wambach, and H. van Hees. The chiral restoration transition of QCD and low mass dileptons. *Landolt-Bornstein*, 23:134, 2010.

[16] S. Borsanyi et al. Is there still any Tc mystery in lattice QCD? Results with physical masses in the continuum limit III. *JHEP*, 09:073, 2010.

[17] A. at al. Bazavov. The chiral and deconfinement aspects of the QCD transition. *Phys. Rev.*, D85:054503, 2012.

[18] M. A. Shifman, A. I. Vainshtein, and V. I. Zakharov. QCD and resonance physics. Theoretical foundations. *Nucl. Phys.*, B147:385–447, 1979.

[19] M. A. Shifman, A. I. Vainshtein, and V. I. Zakharov. QCD and resonance physics: Applications. *Nucl. Phys.*, B147:448–518, 1979.

[20] S. Weinberg. Precise relations between the spectra of vector and axial vector mesons. *Phys. Rev. Lett.*, 18:507–509, 1967.

[21] T. Das, V. S. Mathur, and S. Okubo. Low-energy theorem in the radiative decays of charged pions. *Phys. Rev. Lett.*, 19:859–861, 1967.

[22] J. I. Kapusta and E. V. Shuryak. Weinberg type sum rules at zero and finite temperature. *Phys. Rev.*, D49:4694–4704, 1994.

[23] P. Gerber and H. Leutwyler. Hadrons below the chiral phase transition. *Nucl. Phys.*, B321:387, 1989.

[24] M. Dey, V. L. Eletsky, and B. L. Ioffe. Mixing of vector and axial mesons at finite temperature: an Indication towards chiral symmetry restoration. *Phys. Lett.*, B252:620–624, 1990.

[25] J. V. Steele, H. Yamagishi, and I. Zahed. Dilepton and photon emission rates from a hadronic gas. *Phys. Lett.*, B384:255–262, 1996.

[26] G. Chanfray, J. Delorme, and M. Ericson. Chiral symmetry restoration and parity mixing. *Nucl. Phys.*, A637:421–432, 1998.

[27] B. Krippa. Chiral symmetry and mixing of axial and vector correlators in matter. *Phys. Lett.*, B427:13–18, 1998.

[28] T. Hatsuda and S. H. Lee. QCD sum rules for vector mesons in nuclear medium. *Phys. Rev.*, C46:34–38, 1992.

[29] T. Hatsuda, Y. Koike, and S. H. Lee. Finite temperature QCD sum rules reexamined: rho, omega and A1 mesons. *Nucl. Phys.*, B394:221–266, 1993.

[30] F. Klingl, N. Kaiser, and W. Weise. Current correlation functions, QCD sum rules and vector mesons in baryonic matter. *Nucl. Phys.*, A624:527–563, 1997.

[31] S. Leupold, W. Peters, and U. Mosel. What QCD sum rules tell about the rho meson. *Nucl. Phys.*, A628:311–324, 1998.

[32] S. Leupold and U. Mosel. QCD sum rules for vector mesons in nuclear medium. *Phys. Rev.*, C58:2939–2957, 1998.

[33] Y. Kwon, M. Procura, and W. Weise. QCD sum rules for rho mesons in vacuum and in-medium, re-examined. *Phys. Rev.*, C78:055203, 2008.

[34] Y. Kwon, C. Sasaki, and W. Weise. Vector mesons at finite temperature and QCD sum rules. *Phys. Rev.*, C81:065203, 2010.

[35] S. Leupold. QCD sum rule analysis for light vector and axial - vector mesons in vacuum and nuclear matter. *Phys. Rev.*, C64:015202, 2001.

[36] P.M. Hohler. private communication, 2012.

[37] R. Barate et al. Measurement of the spectral functions of axial - vector hadronic tau decays and determination of alpha(S)(M**2(tau)). *Eur. Phys. J.*, C4:409–431, 1998.

[38] K. Ackerstaff et al. Measurement of the strong coupling constant alpha(s) and the vector and axial vector spectral functions in hadronic tau decays. *Eur. Phys. J.*, C7:571–593, 1999.

[39] B. L. Ioffe. Chiral effective theory of strong interactions. *Phys. Usp.*, 44:1211–1227, 2001.

[40] S. Weinberg. *The quantum theory of fields. Vol. 2: Modern applications*. Cambridge University Press, 1995.

[41] U. Mosel. *Fields, symmetries, and quarks*. McGraw-Hill, 1989.

[42] M. A. Shifman. Quark hadron duality. In *Proceedings, 8th International Symposium on Heavy Flavor Physics (Heavy Flavors 8)*, 2000.

[43] K. G. Wilson. Nonlagrangian models of current algebra. *Phys. Rev.*, 179:1499–1512, 1969.

[44] K. G. Wilson. The renormalization group and strong interactions. *Phys. Rev.*, D3:1818, 1971.

[45] K. G. Wilson and J. B. Kogut. The renormalization group and the epsilon expansion. *Phys. Rept.*, 12:75–200, 1974.

[46] T. D. Cohen, R. J. Furnstahl, D. K. Griegel, and X. Jin. QCD sum rules and applications to nuclear physics. *Prog. Part. Nucl. Phys.*, 35:221–298, 1995.

[47] S. N. Nikolaev and A. V. Radyushkin. Vacuum corrections to QCD charmonium sum rules: Basic formalism and O (G^3) results. *Nucl. Phys.*, B213:285, 1983.

[48] D. B. Leinweber. QCD sum rules for skeptics. *Annals Phys.*, 254:328–396, 1997.

[49] B. L. Ioffe and K. N. Zyablyuk. Gluon condensate in charmonium sum rules with three loop corrections. *Eur. Phys. J.*, C27:229–241, 2003.

[50] J. J. Sakurai. *Currents and mesons*. The University of Chicago Press, 1969.

[51] H. Leutwyler and Andrei V. Smilga. Nucleons at finite temperature. *Nucl. Phys.*, B342:302–316, 1990.

[52] V. L. Eletsky. Correlator of nucleon currents at finite temperature. *Phys. Lett.*, B245:229–232, 1990.

[53] S. Zschocke, O. P. Pavlenko, and B. Kampfer. Evaluation of QCD sum rules for light vector mesons at finite density and temperature. *Eur. Phys. J.*, A15:529–537, 2002.

[54] S. Zschocke, B. Kampfer, O. P. Pavlenko, and G. Wolf. Evaluation of QCD sum rules for HADES. In *Proceedings, 40th International Winter Meeting on Nuclear Physics (Bormio 2002)*, 2002.

[55] R. L. Jaffe and M. Soldate. Twist four in the QCD analysis of leptoproduction. *Phys. Lett.*, B105:467–472, 1981.

[56] R. L. Jaffe and M. Soldate. Twist four in electroproduction: Canonical operators and coefficient functions. *Phys. Rev.*, D26:49–68, 1982.

[57] D. B. Leinweber. QCD sum rule analysis of spin orbit splitting in baryons. *Annals Phys.*, 198:203, 1990.

[58] D. B. Leinweber. Testing QCD sum rule techniques on the lattice. *Phys. Rev.*, D51:6369–6382, 1995.

[59] V. L. Eletsky. Four quark condensates at T not = 0. *Phys. Lett.*, B299:111–114, 1993.

[60] M. Gell-Mann, R. J. Oakes, and B. Renner. Behavior of current divergences under SU(3) x SU(3). *Phys. Rev.*, 175:2195–2199, 1968.

[61] R. F. Dashen. Chiral SU(3) x SU(3) as a symmetry of the strong interactions. *Phys. Rev.*, 183:1245–1260, 1969.

[62] R. Rapp. Dilepton spectroscopy of QCD matter at collider energies. *Adv. High Energy Phys.*, 2013:148253, 2013.

[63] H. van Hees, C. Gale, and R. Rapp. Thermal photons and collective flow at the relativistic heavy-ion collider. *Phys. Rev.*, C84:054906, 2011.

[64] H. van Hees, M. He, and R. Rapp. Pseudo-critical enhancement of thermal photons in relativistic heavy-ion collisions? *Nucl. Phys.*, A933:256–271, 2015.

[65] A. Adare et al. Enhanced production of direct photons in Au+Au collisions at $\sqrt{s_{NN}} = 200$ GeV and implications for the initial temperature. *Phys. Rev. Lett.*, 104:132301, 2010.

[66] A. Adare et al. Observation of direct-photon collective flow in $\sqrt{s_{NN}} = 200$ GeV Au+Au collisions. *Phys. Rev. Lett.*, 109:122302, 2012.

[67] M. Wilde. Measurement of direct photons in pp and Pb-Pb collisions with ALICE. *Nucl. Phys.*, A904-905:573c–576c, 2013.

[68] D. Lohner. Measurement of direct-photon elliptic flow in Pb-Pb collisions at $\sqrt{s_{NN}} = 2.76$ TeV. *J. Phys. Conf. Ser.*, 446:012028, 2013.

[69] C. Yang. Direct photon production in Au + Au collisions at $\sqrt{s_{NN}} = 200$ GeV at STAR. *Nucl. Phys.*, A931:691–695, 2014.

[70] J. Adam et al. Direct photon production in Pb-Pb collisions at $\sqrt{s_{\rm NN}} = 2.76$ TeV. *Phys. Lett.*, B754:235–248, 2016.

[71] B. Sahlmueller. Direct photon measurement in Pb-Pb collisions at $\sqrt{s_{\rm NN}} = 2.76$ TeV with ALICE. In *25th International Conference on Ultra-Relativistic Nucleus-Nucleus Collisions (Quark Matter 2015) Kobe, Japan, September 27-October 3, 2015*, 2015.

[72] F. Liu, T. Hirano, K. Werner, and Y. Zhu. Elliptic flow of thermal photons in Au + Au collisions at s(NN)**(1/2) = 200-GeV. *Phys. Rev.*, C80:034905, 2009.

[73] M. Dion, J. Paquet, B. Schenke, C. Young, S. Jeon, and C. Gale. Viscous photons in relativistic heavy ion collisions. *Phys. Rev.*, C84:064901, 2011.

[74] O. Linnyk, W. Cassing, and E. L. Bratkovskaya. Centrality dependence of the direct photon yield and elliptic flow in heavy-ion collisions at $\sqrt{s_{NN}} = 200$ GeV. *Phys. Rev.*, C89(3):034908, 2014.

[75] A. Bzdak and V. Skokov. Anisotropy of photon production: initial eccentricity or magnetic field. *Phys. Rev. Lett.*, 110(19):192301, 2013.

[76] A. Monnai. Thermal photon v_2 with slow quark chemical equilibration. *Phys. Rev.*, C90(2):021901, 2014.

[77] C. at al. Gale. Production and elliptic flow of dileptons and photons in a matrix model of the quark-gluon plasma. *Phys. Rev. Lett.*, 114:072301, 2015.

[78] L. McLerran and B. Schenke. A tale of tails: photon rates and flow in ultra-relativistic heavy ion collisions. *Nucl. Phys.*, A946:158–170, 2016.

[79] J.-F. Paquet, C. Shen, G. S. Denicol, M. Luzum, B. Schenke, S. Jeon, and C. Gale. Production of photons in relativistic heavy-ion collisions. *Phys. Rev.*, C93(4):044906, 2016.

[80] A. Ayala, J. D. Castano-Yepes, C. A. Dominguez, and L. A. Hernandez. Thermal photon production from gluon fusion induced by magnetic fields in relativistic heavy-ion collisions. 2016.

[81] R. Rapp. Theory of soft electromagnetic emission in heavy-ion collisions. *Acta Phys. Polon.*, B42:2823–2852, 2011.

[82] S. Endres, H. van Hees, and M. Bleicher. Photon and dilepton production at the Facility for Anti-Proton and Ion Research and the beam energy scan program at the Relativistic Heavy-Ion Collider using coarse-grained microscopic transport simulations. *Phys. Rev.*, C93:054901, 2016.

[83] Jan-e Alam, Pradip Roy, and Sourav Sarkar. Thermal radiation from baryons and mesons. *Phys. Rev.*, C68:031901, 2003.

[84] S. Turbide, R. Rapp, and C. Gale. Hadronic production of thermal photons. *Phys. Rev.*, C69:014903, 2004.

[85] J. J. Sakurai. Theory of strong interactions. *Annals Phys.*, 11:1–48, 1960.

[86] M. Gell-Mann and F. Zachariasen. Form-factors and vector mesons. *Phys. Rev.*, 124:953–964, 1961.

[87] N. M. Kroll, T. D. Lee, and B. Zumino. Neutral vector mesons and the hadronic electromagnetic current. *Phys. Rev.*, 157:1376–1399, 1967.

[88] S. Turbide. *Electromagnetic radiation from matter under extreme conditions*. PhD thesis, McGill U., 2006.

[89] J. I. Kapusta and C. Gale. *Finite-temperature field theory: Principles and applications*. Cambridge University Press, 2011.

[90] C. Gale. Photon Production in Hot and Dense Strongly Interacting Matter. *Landolt-Bornstein*, 23:445, 2010.

[91] F. Halzen and A. D. Martin. *Quarks and leptons: An introductory course in modern particle physics*. 1984.

[92] J. Wess and B. Zumino. Consequences of anomalous Ward identities. *Phys. Lett.*, B37:95, 1971.

[93] E. Witten. Current algebra, baryons, and quark confinement. *Nucl. Phys.*, B223:433–444, 1983.

[94] R. Rapp and C. Gale. Rho properties in a hot meson gas. *Phys. Rev.*, C60:024903, 1999.

[95] Chen-Ning Y. and R. L. Mills. Conservation of isotopic spin and isotopic gauge invariance. *Phys. Rev.*, 96:191–195, 1954.

[96] T. E. O. Ericson and W. Weise. *Pions and Nuclei*. Clarendon Press, Oxford, UK, 1988.

[97] J. I. Kapusta, P. Lichard, and D. Seibert. High-energy photons from quark-gluon plasma versus hot hadronic gas. *Phys. Rev.*, D44:2774–2788, 1991. [Erratum: Phys. Rev.D47,4171(1993)].

[98] R. Rapp and J. Wambach. Low mass dileptons at the CERN SPS: Evidence for chiral restoration? *Eur. Phys. J.*, A6:415–420, 1999.

[99] M. Urban, M. Buballa, R. Rapp, and J. Wambach. Modifications of the rho meson from the virtual pion cloud in hot and dense matter. *Nucl. Phys.*, A673:357–374, 2000.

[100] J. Cleymans, K. Redlich, and D. K. Srivastava. Thermal particle and photon production in pb + pb collisions with transverse flow. *Phys. Rev.*, C55:1431–1442, 1997.

[101] P. Huovinen, P. V. Ruuskanen, and S. S. Rasanen. Photon emission in heavy ion collisions at the CERN SPS. *Phys. Lett.*, B535:109–116, 2002.

[102] James V. Steele, Hidenaga Yamagishi, and Ismail Zahed. Dilepton and photon emission rates from a hadronic gas. II. *Phys. Rev.*, D56:5605–5617, 1997.

[103] O. Linnyk, E. L. Bratkovskaya, and W. Cassing. Effective QCD and transport description of dilepton and photon production in heavy-ion collisions and elementary processes. *Prog. Part. Nucl. Phys.*, 87:50–115, 2016.

[104] R. Rapp, G. Chanfray, and J. Wambach. Rho meson propagation and dilepton enhancement in hot hadronic matter. *Nucl. Phys.*, A617:472–495, 1997.

[105] W. Rarita and J. Schwinger. On a theory of particles with half integral spin. *Phys. Rev.*, 60:61, 1941.

[106] A. M. Gasparyan, J. Haidenbauer, C. Hanhart, and J. Speth. Pion nucleon scattering in a meson exchange model. *Phys. Rev.*, C68:045207, 2003.

[107] R. Machleidt. The Meson theory of nuclear forces and nuclear structure. *Adv. Nucl. Phys.*, 19:189–376, 1989.

[108] Agnieszka Bieniek, Anna Baran, and Wojciech Broniowski. $\omega \to \pi^0\gamma^*$, $\rho \to \pi\gamma^*$, and $\pi^0 \to \gamma\gamma^*$ decays in nuclear medium. *Phys. Lett.*, B526:329–334, 2002.

[109] M. Urban, M. Buballa, R. Rapp, and J. Wambach. Momentum dependence of the pion cloud for rho mesons in nuclear matter. *Nucl. Phys.*, A641:433–460, 1998.

[110] G. Velo and D. Zwanziger. Noncausality and other defects of interaction lagrangians for particles with spin one and higher. *Phys. Rev.*, 188:2218–2222, 1969.

[111] M. Benmerrouche, R. M. Davidson, and N. C. Mukhopadhyay. Problems of describing spin 3/2 baryon resonances in the effective lagrangian theory. *Phys. Rev.*, C39:2339–2348, 1989.

[112] F. Riek, R. Rapp, T. S. H. Lee, and Y. Oh. Medium Effects in rho-Meson Photoproduction. *Phys. Lett.*, B677:116–120, 2009.

[113] M. Herrmann, B. L. Friman, and W. Norenberg. Properties of rho mesons in nuclear matter. *Nucl. Phys.*, A560:411–436, 1993.

[114] M. Herrmann. Eigenschaten des ρ-mesons in dichter kernmaterie. Dissertation (doktorarbeit), Technischen Hochschule Darmstadt, Germany, 1992. GSI-Report 92-10.

[115] J. F. Mathiot. What do we learn from deuteron electrodisintegration near threshold and thermal np capture? *Nucl. Phys.*, A412:201–227, 1984.

[116] T. Roth. Die reaktion $\pi N \to \rho N$ und der πN-formfaktor. Master's thesis (diplomarbeit), Technische Universitat Darmstadt, Germany, 1999.

[117] M. Post and U. Mosel. Coupling of baryon resonances to the N omega channel. *Nucl. Phys.*, A688:808–822, 2001.

[118] F. Lenz and E. J. Moniz. Propagation in Nonlocal Optical Potentials. *Phys. Rev.*, C12:909–914, 1975.

[119] R. M. Woloshyn, E. J. Moniz, and R. Aaron. Relativistic Three-Body Calculation of pi d Scattering. *Phys. Rev.*, C13:286–298, 1976.

[120] E. J. Moniz and A. Sevgen. Pauli blocking in the nuclear medium piN transition matrix. *Phys. Rev.*, C24:224–230, 1981.

[121] G. E. Brown and W. Weise. Pion scattering and isobars in nuclei. *Phys. Rept.*, 22:279–337, 1975.

[122] S. U. Chung, J. Brose, R. Hackmann, E. Klempt, S. Spanier, and C. Strassburger. Partial wave analysis in K matrix formalism. *Annalen Phys.*, 4:404–430, 1995.

[123] E. Oset, H. Toki, and W. Weise. Pionic modes of excitation in nuclei. *Phys. Rept.*, 83:281–380, 1982.

[124] S. Weinberg. *The quantum theory of fields. Vol. 1: Foundations.* Cambridge University Press, 1995.

[125] P. M. Hohler and R. Rapp. Is ρ-meson melting compatible with chiral restoration? *Phys. Lett.*, B731:103–109, 2014.

[126] M. Urban. Impulsabhängigkeit des ρ-meson-propagators in kalter kernmaterie. Master's thesis (diplomarbeit), Technische Hochschule Darmstadt, Germany, 1997.

APPENDIX A

BORN MATRIX ELEMENTS

In this appendix we list the matrix elements for our photon-producing processes. We use the following notation:

- e_a/e_a^* is an isospin polarization vector (in Cartesian space) for an incoming/outgoing isovector particle,
- $\epsilon_\mu/\epsilon_\mu^*$ is a spin polarization vector (in Minkowski space) for an incoming/outgoing vector particle,
- ϕ_i is the spinor in isospin space of the i^{th} baryon, and is 2-dimensional for isospin-1/2 baryons (nucleons) and 4-dimensional for isospin-3/2 particles (deltas),
- χ_i is a baryon spinor in spin space of the i^{th} baryon, and is 2-dimensional for spin-1/2 baryons and 4-dimensional for spin-3/2 particles,
- $\vec{\mathcal{T}}$ is the isospin transition operator between ϕ_1 and ϕ_2 with Cartesian components $\mathcal{T}_a$, and is given in Table A.1,
- $\vec{\mathcal{S}}$ is the spin transition operator between χ_1 and χ_2, and is given in Table A.1,

The matrix elements for the spin and isospin transition operators are given below.

The form factors $\Gamma_\pi(\vec{k})$ and $\Gamma_\pi^D(\vec{k})$ are given by

$$\Gamma_\pi(\vec{k}) = \frac{\Lambda^2}{\Lambda^2 + \vec{k}^2}\,,$$
$$\Gamma_\pi^D(\vec{k}) = \frac{\Lambda^4}{\Lambda^4 + \vec{k}^4}\,. \tag{A.1}$$

Transition	Spin	Isospin
$1/2 \to 1/2$	$\vec{\sigma}$	$\vec{\tau}$
$1/2 \to 3/2$	$\vec{S}$	$\vec{T}$
$3/2 \to 1/2$	$\vec{S}^{\dagger}$	$\vec{T}^{\dagger}$
$3/2 \to 3/2$	$\vec{S}^{(3/2)}$	$\vec{T}^{(3/2)}$

Table A.1: Representations of spin and isospin transition operators based on the spin/isospin quantum numbers of the initial- and final-state baryons.

The D-wave vertex vector $\vec{V}^{D}$ is

$$\vec{V}^{D} = 4\vec{k}(\vec{k}^2 - \vec{k}\cdot\vec{q}) + \vec{q}(4\vec{k}\cdot\vec{q} - 2\vec{k}^2 - \vec{q}^2)\,. \tag{A.2}$$

Photon-Producing Baryonic Processes

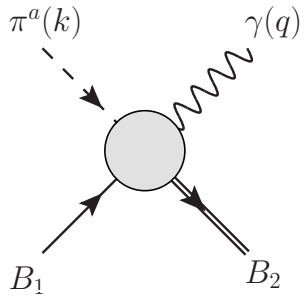

Figure A.1: Schematic diagram of the photon-producing process $\pi B_1 \to \gamma B_2$.

- S-wave:

$$M^S = ig_\rho C_\rho \frac{f_{\pi B_1 B_2}}{m_\pi} \left[\phi_2^\dagger \left(\epsilon_{3ba}\mathcal{T}_b\right)\phi_1\right] e_a \\ \chi_2^\dagger \left\{ \Gamma_\pi(\vec{k}) \begin{pmatrix} 1 - \frac{\omega_k}{q_0} \\ \frac{(\omega_k - q_0)(2\vec{k}-\vec{q})}{(\vec{k}-\vec{q})^2+\Lambda^2} \end{pmatrix}^\mu - \Gamma_\pi(\vec{k}-\vec{q}) \frac{(\omega_k - q_0)(2k-q)^\mu}{t-m_\pi^2} \right\} \chi_1 \, \epsilon_\mu^* \tag{A.3}$$

- P-wave:

$$M^P = ig_\rho C_\rho \frac{f_{\pi B_1 B_2}}{m_\pi} \left[\phi_2^\dagger \left(\epsilon_{3ba}\mathcal{T}_b\right)\phi_1\right] e_a \\ \chi_2^\dagger \left\{ \Gamma_\pi(\vec{k}) \begin{pmatrix} -\frac{\vec{k}\cdot\vec{\mathcal{S}}}{q_0} \\ \frac{(\vec{k}-\vec{q})\cdot\vec{\mathcal{S}}\,(2\vec{k}-\vec{q})}{(\vec{k}-\vec{q})^2+\Lambda^2} - \vec{\mathcal{S}} \end{pmatrix}^\mu - \Gamma_\pi(\vec{k}-\vec{q}) \frac{(\vec{k}-\vec{q})\cdot\vec{\mathcal{S}}\,(2k-q)^\mu}{t-m_\pi^2} \right\} \chi_1 \, \epsilon_\mu^* \tag{A.4}$$

- D-wave:

$$M^D = ig_\rho C_\rho \frac{f_{\pi B_1 B_2}}{m_\pi^2} \left[\phi_2^\dagger \left(\epsilon_{3ba}\mathcal{T}_b\right)\phi_1\right] e_a \\ \chi_2^\dagger \left\{ \Gamma_\pi^D(\vec{k}) \begin{pmatrix} -(\vec{k}\cdot\vec{S})(\vec{k}\cdot\vec{\sigma})\frac{1}{q_0} \\ \frac{(\vec{k}-\vec{q})\cdot\vec{S}\,(\vec{k}-\vec{q})\cdot\vec{\sigma}\,\vec{V}^D}{(\vec{k}-\vec{q})^4+\Lambda^4} - \vec{S}(\vec{k}-\vec{q})\cdot\vec{\sigma} - (\vec{k}\cdot\vec{S})\vec{\sigma} \end{pmatrix}^\mu \\ - \Gamma_\pi^D(\vec{k}-\vec{q}) \frac{(\vec{k}-\vec{q})\cdot\vec{S}\,(\vec{k}-\vec{q})\cdot\vec{\sigma}\,(2k-q)^\mu}{t-m_\pi^2} \right\} \chi_1 \, \epsilon_\mu^* \tag{A.5}$$

The D-wave matrix element written above is for a spin-1/2 to spin-3/2 baryon transition. For a spin-3/2 to spin-1/2 transition, one must make the replacement $\vec{S} \to \vec{S}^\dagger$ and the reverse the order of the $\vec{S}$ and $\vec{\sigma}$ matrices, such that

$$(\vec{k}\cdot\vec{S})(\vec{k}\cdot\vec{\sigma}) \to (\vec{k}\cdot\vec{\sigma})(\vec{k}\cdot\vec{S}^\dagger)\,. \tag{A.6}$$

- ω t-channel exchange

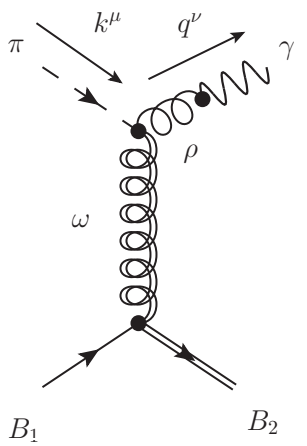

Figure A.2: Photon-producing ω t-channel exchange process.

Mention that only ωNN counts– others are tremendously suppressed.

$$M^{+}_{\omega\ \mathrm{t-chan}} = i\left(g_{\omega NN^*} g_{\pi\rho\omega} C_\rho\right)\left[\phi_2^\dagger\,\delta_{a3}\,\phi_1\right]\ e_a\left[\chi_2^\dagger \begin{pmatrix}\omega_0\\ 0\end{pmatrix}^\mu \chi_1\right]\left(\frac{2\Lambda^2_{\pi\rho\omega}}{2\Lambda^2_{\pi\rho\omega}-t}\right)^2 \left(\frac{\Lambda^2_{\omega BB}}{\Lambda^2_{\omega BB}+(\vec{k}-\vec{q})^2}\right)\left(\frac{-g_{\mu\nu}-\frac{(k-q)_\mu(k-q)_\nu}{m^2_\omega}}{t-m^2_\omega}\right)\epsilon^{\alpha\beta\lambda\nu}\,q_\alpha\,\varepsilon^*_\beta\,(k-q)_\lambda \quad \text{(A.7)}$$

$$M^{-}_{\omega\ \mathrm{t-chan}} = i\left(g_{\omega NN^*} g_{\pi\rho\omega} C_\rho\right)\left[\phi_2^\dagger\,\delta_{a3}\,\phi_1\right]\ e_a\left[\chi_2^\dagger \begin{pmatrix}0\\ \vec{\omega}\cdot\vec{\mathcal{S}}\end{pmatrix}^\mu \chi_1\right]\left(\frac{2\Lambda^2_{\pi\rho\omega}}{2\Lambda^2_{\pi\rho\omega}-t}\right)^2 \left(\frac{\Lambda^2_{\omega BB}}{\Lambda^2_{\omega BB}+(\vec{k}-\vec{q})^2}\right)\left(\frac{-g_{\mu\nu}-\frac{(k-q)_\mu(k-q)_\nu}{m^2_\omega}}{t-m^2_\omega}\right)\epsilon^{\alpha\beta\lambda\nu}\,q_\alpha\,\varepsilon^*_\beta\,(k-q)_\lambda \quad \text{(A.8)}$$

- Incoming ω

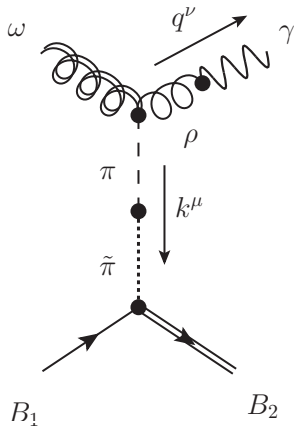

Figure A.3: Photon-producing $\omega B_1 \to \gamma B_2$ π t-channel exchange process.

$$M^S_{\omega\ \mathrm{inc}} = -i\left(g_{\pi\rho\omega}\frac{f_{\pi B_1 B_2}}{m_\pi}C_\rho\right)\left[\phi_2^\dagger\,\delta_{3b}\mathcal{T}_b\,\phi_1\right]\left[\chi_2^\dagger(\omega_k)\chi_1\right]\left(\frac{2\Lambda^2_{\pi\rho\omega}}{2\Lambda^2_{\pi\rho\omega}-t}\right)^2$$
$$\left(\frac{\Lambda^2_{\pi B_1 B_2}}{\Lambda^2_{\pi B_1 B_2}+\vec{k}^2}\right)\left(\frac{1}{t-m_\pi^2}\right)\epsilon^{\alpha\beta\lambda\nu}\,q_\alpha\,\varepsilon_\beta\,(k+q)_\lambda\,\varepsilon^*_\nu \tag{A.9}$$

$$M^P_{\omega\ \mathrm{inc}} = -i\left(g_{\pi\rho\omega}\frac{f_{\pi B_1 B_2}}{m_\pi}C_\rho\right)\left[\phi_2^\dagger\,\delta_{3b}\mathcal{T}_b\,\phi_1\right]\left[\chi_2^\dagger(\vec{k}\cdot\vec{\mathcal{S}})\chi_1\right]\left(\frac{2\Lambda^2_{\pi\rho\omega}}{2\Lambda^2_{\pi\rho\omega}-t}\right)^2$$
$$\left(\frac{\Lambda^2_{\pi B_1 B_2}}{\Lambda^2_{\pi B_1 B_2}+\vec{k}^2}\right)\left(\frac{1}{t-m_\pi^2}\right)\epsilon^{\alpha\beta\lambda\nu}\,q_\alpha\,\varepsilon_\beta\,(k+q)_\lambda\,\varepsilon^*_\nu \tag{A.10}$$

$$M^D_{\omega\ \mathrm{inc}} = -i\left(g_{\pi\rho\omega}\frac{f_{\pi B_1 B_2}}{m_\pi^2}C_\rho\right)\left[\phi_2^\dagger\,\delta_{3b}\mathcal{T}_b\,\phi_1\right]\left[\chi_2^\dagger(\vec{k}\cdot\vec{S})(\vec{k}\cdot\vec{\sigma})\chi_1\right]\left(\frac{2\Lambda^2_{\pi\rho\omega}}{2\Lambda^2_{\pi\rho\omega}-t}\right)^2$$
$$\left(\frac{\Lambda^4_{\pi B_1 B_2}}{\Lambda^4_{\pi B_1 B_2}+\vec{k}^4}\right)\left(\frac{1}{t-m_\pi^2}\right)\epsilon^{\alpha\beta\lambda\nu}\,q_\alpha\,\varepsilon_\beta\,(k+q)_\lambda\,\varepsilon^*_\nu \tag{A.11}$$

• $\pi\rho \to \gamma\omega$

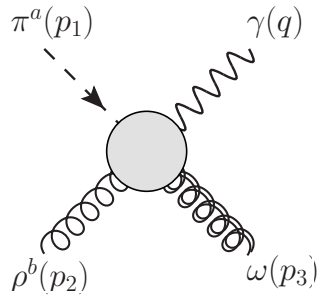

Figure A.4: Diagram showing four-momenta labels and isospin indices for the process $\pi\rho \to \gamma\omega$.

$$M_s = -\frac{g_{\pi\rho\omega}g_\rho C_\rho}{s-m_\pi^2}(2p_1-p_2)_\delta q^\mu p_3^\alpha\,\epsilon_{\mu\gamma\alpha\beta}\,\varepsilon^\delta(p_2)\varepsilon^{*\gamma}(q)\varepsilon^{*\beta}(p_3)\,\epsilon^{3ab}e_a e_b \quad \text{(A.12)}$$

$$M_t = -\frac{g_{\pi\rho\omega}g_\rho C_\rho}{t-m_\pi^2}(2p_1-q)_\gamma p_2^\mu p_3^\alpha\,\epsilon_{\mu\delta\alpha\beta}\,\varepsilon^\delta(p_2)\varepsilon^{*\gamma}(q)\varepsilon^{*\beta}(p_3)\,\epsilon^{3ab}e_a e_b \quad \text{(A.13)}$$

$$\begin{aligned} M_u = &-\frac{g_{\pi\rho\omega}g_\rho C_\rho}{t-m_\rho^2}(p_2-q)^\mu p_3^\alpha\left(-g^{\nu\lambda}+\frac{(p_2-q)^\nu(p_2-q)^\lambda}{m_\rho^2}\right)\\ &\left[-g_{\delta\gamma}(p_2+q)_\lambda - g_{\gamma\lambda}(p_2-2q)^\delta + g_{\delta\lambda}(2p_2-q)_\gamma\right]\\ &\epsilon_{\mu\nu\alpha\beta}\,\varepsilon^\delta(p_2)\varepsilon^{*\gamma}(q)\varepsilon^{*\beta}(p_3)\,\epsilon^{3ab}e_a e_b \end{aligned} \quad \text{(A.14)}$$

$$M_c = -g_{\pi\rho\omega}g_\rho C_\rho p_3^\alpha\,\epsilon_{\gamma\delta\alpha\beta}\,\varepsilon^\delta(p_2)\varepsilon^{*\gamma}(q)\varepsilon^{*\beta}(p_3)\,\epsilon^{3ab}e_a e_b \quad \text{(A.15)}$$

• $\pi\omega \to \gamma\rho$

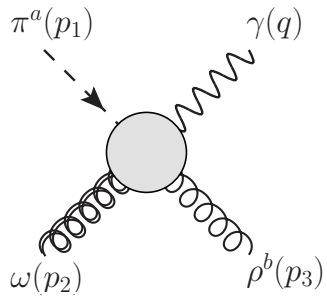

Figure A.5: Diagram showing four-momenta labels and isospin indices for the process $\pi\omega \to \gamma\rho$.

$$
\begin{aligned}
M_s &= -\frac{g_{\pi\rho\omega} g_\rho C_\rho}{s - m_\rho^2} p_1^\mu p_2^\alpha \left(-g^{\nu\lambda} + \frac{(q+p_3)^\nu (q+p_3)^\lambda}{m_\rho^2} \right) \\
&\quad [g_{\lambda\delta}(q+2p_3)_\gamma - g_{\lambda\gamma}(2q+p_3)_\delta + g_{\gamma\delta}(q-p_3)_\lambda] \\
&\quad \epsilon_{\mu\nu\alpha\beta}\, \varepsilon^\beta(p_2) \varepsilon^{*\gamma}(q) \varepsilon^{*\delta}(p_3) \epsilon^{3ab} e_a e_b^* \qquad \text{(A.16)} \\
M_t &= \frac{g_{\pi\rho\omega} g_\rho C_\rho}{t - m_\pi^2} (p_1 - q)^\mu p_2^\alpha (2p_1 - q)_\gamma \\
&\quad \epsilon_{\mu\delta\alpha\beta}\, \varepsilon^\beta(p_2) \varepsilon^{*\gamma}(q) \varepsilon^{*\delta}(p_3)\, \epsilon^{3ab} e_a e_b^* \qquad \text{(A.17)} \\
M_u &= \frac{g_{\pi\rho\omega} g_\rho C_\rho}{u - m_\pi^2} (p_2 - q)^\mu p_2^\alpha (p_1 - p_2 + q)_\delta \\
&\quad \epsilon_{\mu\gamma\alpha\beta}\, \varepsilon^\beta(p_2) \varepsilon^{*\gamma}(q) \varepsilon^{*\delta}(p_3)\, \epsilon^{3ab} e_a e_b^* \qquad \text{(A.18)} \\
M_c &= g_{\pi\rho\omega} g_\rho C_\rho p_2^\alpha\, \epsilon_{\delta\gamma\alpha\beta}\, \varepsilon^\beta(p_2) \varepsilon^{*\gamma}(q) \varepsilon^{*\delta}(p_3)\, \epsilon^{3ab} e_a e_b^* \qquad \text{(A.19)}
\end{aligned}
$$

- $\rho\omega \to \gamma\pi$

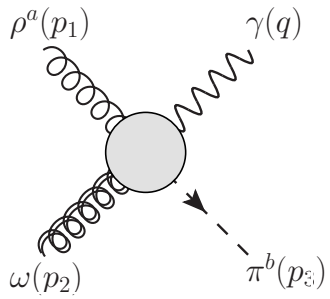

Figure A.6: Diagram showing four-momenta labels and isospin indices for the process $\rho\omega \to \gamma\omega$.

$$
\begin{aligned}
M_s &= \frac{g_{\pi\rho\omega} g_\rho C_\rho}{s - m_\pi^2} p_1^\mu p_2^\alpha (q + 2p_3)_\gamma \, \epsilon_{\mu\delta\alpha\beta} \, \varepsilon^\delta(p_1) \varepsilon^\beta(p_2) \varepsilon^{*\gamma}(q) \, \epsilon^{3ab} e_a e_b^* && \text{(A.20)} \\
M_t &= -\frac{g_{\pi\rho\omega} g_\rho C_\rho}{t - m_\rho^2} (p_1 - q)^\mu p_2^\alpha \left(-g^{\nu\lambda} + \frac{(p_1 - q)^\nu (p_1 - q)^\lambda}{m_\rho^2} \right) \\
&\quad [-g_{\delta\gamma}(p_1 + q)_\lambda - g_{\gamma\lambda}(p_1 - 2q)_\delta + g_{\delta\lambda}(2p_1 - q)_\gamma] \\
&\quad \epsilon_{\mu\nu\alpha\beta} \, \varepsilon^\delta(p_1) \varepsilon^\beta(p_2) \varepsilon^{*\gamma}(q) \, \epsilon^{3ab} e_a e_b^* && \text{(A.21)} \\
M_u &= \frac{g_{\pi\rho\omega} g_\rho C_\rho}{u - m_\pi^2} p_3^\mu p_2^\alpha (p_2 - q + p_3)_\delta \, \epsilon_{\mu\gamma\alpha\beta} \, \varepsilon^\delta(p_1) \varepsilon^\beta(p_2) \varepsilon^{*\gamma}(q) \, \epsilon^{3ab} e_a e_b^* && \text{(A.22)} \\
M_c &= g_{\pi\rho\omega} g_\rho C_\rho p_2^\alpha \, \epsilon_{\delta\gamma\alpha\beta} \, \varepsilon^\delta(p_1) \varepsilon^\beta(p_2) \varepsilon^{*\gamma}(q) \, \epsilon^{3ab} e_a e_b^* && \text{(A.23)}
\end{aligned}
$$

1→ 2 Particle Decay Matrices

Here the isospin factor is $IF = \mathrm{Tr}[\mathcal{T}^2]$, and is 6 for $I = \frac{1}{2}$, 4 for $I = 1$, and 15 for $I = \frac{3}{2}$. The spin factor is $SF = \mathrm{Tr}[\mathcal{S}_a \mathcal{S}_b]$ and is 2 for a $\frac{1}{2} \leftrightarrow \frac{1}{2}$ transition, $\frac{4}{3}$ for a $\frac{1}{2} \leftrightarrow \frac{3}{2}$ transition, and 5 for a $\frac{3}{2} \leftrightarrow \frac{3}{2}$ transition.

- $B_1 \to \pi B_2$ S-wave

$$
|M|^2 = 4 \frac{f_\pi^2}{m_\pi^2} m_{B_1} m_{B_2} \mathcal{N} \, IF \, \omega_k^2 \qquad \text{(A.24)}
$$

Here $\mathcal{N}$ is the number of spin states of the decay particle.

- $B_1 \to \pi B_2$ P-wave

$$|M|^2 = 4\frac{f_\pi^2}{m_\pi^2} m_{B_1} m_{B_2} SF\, IF\, \vec{k}^2 \tag{A.25}$$

- $B_1 \to \pi B_2$ D-wave

$$|M|^2 = 4\frac{f_\pi^2}{m_\pi^4} m_{B_1} m_{B_2} SF\, IF\, \vec{k}^4 \tag{A.26}$$

- $N^* \to \omega N$

$$|M|^2 = 8 g_{\omega N N^*} m_N m_{N^*} SF \tag{A.27}$$

This expression is for when both nucleons are parity plus. If the decay particle is parity minus, replace SF with $\mathcal{N}$.

- $N^* \to \omega N$ Helicity Amplitude

$$|M|^2 = 8 g_{\omega N N^*} C_\omega^2 m_N m_{N^*} SF \tag{A.28}$$

Here $C_\omega = 0.0177$ is the electromagnetic coupling of the ω to the photon, calculated from the $\omega \to e^+e^-$ decay. This calculation is identical to the $\rho \to e^+e^-$ given below.

- $\rho \to \pi\pi$

$$|M|^2 = \frac{4}{3} g_\rho^2 \left[(p_{CM}\omega_\pi(p_{CM}) + p_{CM}^2) - m_\pi^2 \right] \tag{A.29}$$

- $\rho \to e^+e^-$

$$|M|^2 = \frac{8\pi}{3} m_\rho^3 C_\rho^2 \alpha_{\mathrm{EM}} \tag{A.30}$$

- $\omega \to \pi^0\gamma$

$$|M|^2 = \frac{2}{3} g_{\pi\rho\omega}^2 C_\rho^2 \left(p_{CM}\omega_\pi(p_{CM}) + p_{CM}^2 \right)^2 \tag{A.31}$$

$SU(2)$ Transition Operator Matrices

Note: Since the mathematical formalism of spin and isospin are carbon-copies of one another, we refer to spin below. All conclusions and results are identical for isospin, necessitating merely a change in notation. In typical physics fashion, we also abuse notation and refer to both the symmetry group and associated Lie algebra as $SU(2)$.

For each process involving a transition between total spin states of $\frac{n-1}{2} \leftrightarrow \frac{n-1}{2}$, where n is an integer, the spin transition operators are the n-dimensional generators of $SU(2)$. The generators of the $SU(2)$ algebra in any dimension are defined to be

$$[T_a, T_b] = i\epsilon_{abc} T_c \,, \quad a, b, c = 1, 2, 3 \,, \tag{A.32}$$

where ϵ_{abc} is the (three-dimensional) Levi-Civita symbol. This symbol is defined by $\epsilon_{123} = +1$ and is equal to zero if any indices are equal, equal to $+1$ under any even permutation of indices, and -1 under any odd permutation of indices.

Note that in this work we use the normalization of $[S_a, S_b] = i\epsilon_{abc} S_c$.

• $\frac{1}{2} \to \frac{1}{2}$ In the above normalization, the $\frac{1}{2} \to \frac{1}{2}$ transition operators are just Pauli matrices with a factor of $1/\sqrt{2}$.

$$S_1^{(1/2)} = \frac{1}{\sqrt{2}} \begin{pmatrix} 0 & 1 \\ 1 & 0 \end{pmatrix} \,, \quad S_2^{(1/2)} = \frac{i}{\sqrt{2}} \begin{pmatrix} 0 & -1 \\ 1 & 0 \end{pmatrix} \,, \quad S_3^{(1/2)} = \frac{1}{\sqrt{2}} \begin{pmatrix} 1 & 0 \\ 0 & -1 \end{pmatrix} \tag{A.33}$$

- $\frac{1}{2} \to \frac{3}{2}$ The $\frac{1}{2} \to \frac{3}{2}$ transition operators are:

$$S_1 = \frac{1}{\sqrt{2}} \begin{pmatrix} -1 & 0 \\ 0 & -\frac{1}{\sqrt{3}} \\ \frac{1}{\sqrt{3}} & 0 \\ 0 & 1 \end{pmatrix}, \quad S_2 = \frac{i}{\sqrt{2}} \begin{pmatrix} 1 & 0 \\ 0 & \frac{1}{\sqrt{3}} \\ \frac{1}{\sqrt{3}} & 0 \\ 0 & 1 \end{pmatrix}, \quad S_3 = \begin{pmatrix} 0 & 0 \\ \sqrt{\frac{2}{3}} & 0 \\ 0 & \sqrt{\frac{2}{3}} \\ 0 & 0 \end{pmatrix}. \tag{A.34}$$

- $\frac{3}{2} \to \frac{1}{2}$ Here we find the reason for the notation $S^\dagger$: these matrices are simply the Hermitian conjugate of the $\frac{1}{2} \to \frac{3}{2}$ transition operators. Thus:

$$S_1^\dagger = \frac{1}{\sqrt{2}} \begin{pmatrix} -1 & 0 & \frac{1}{\sqrt{3}} & 0 \\ 0 & -\frac{1}{\sqrt{3}} & 0 & 1 \end{pmatrix}, \quad S_2^\dagger = -\frac{i}{\sqrt{2}} \begin{pmatrix} 1 & 0 & \frac{1}{\sqrt{3}} & 0 \\ 0 & \frac{1}{\sqrt{3}} & 0 & 1 \end{pmatrix}$$
$$S_3^\dagger = \frac{1}{\sqrt{2}} \begin{pmatrix} 0 & \sqrt{\frac{2}{3}} & 0 & 0 \\ 0 & 0 & \sqrt{\frac{2}{3}} & 0 \end{pmatrix} \tag{A.35}$$

- $\frac{3}{2} \to \frac{3}{2}$

$$S_1^{(3/2)} = \begin{pmatrix} 0 & \frac{\sqrt{3}}{2} & 0 & 0 \\ \frac{\sqrt{3}}{2} & 0 & 1 & 0 \\ 0 & 1 & 0 & \frac{\sqrt{3}}{2} \\ 0 & 0 & \frac{\sqrt{3}}{2} & 0 \end{pmatrix}, \quad S_2^{(3/2)} = -i \begin{pmatrix} 0 & \frac{\sqrt{3}}{2} & 0 & 0 \\ -\frac{\sqrt{3}}{2} & 0 & 1 & 0 \\ 0 & -1 & 0 & \frac{\sqrt{3}}{2} \\ 0 & 0 & -\frac{\sqrt{3}}{2} & 0 \end{pmatrix}$$
$$S_3^{(3/2)} = \frac{1}{2} \begin{pmatrix} 3 & 0 & 0 & 0 \\ 0 & 1 & 0 & 0 \\ 0 & 0 & -1 & 0 \\ 0 & 0 & 0 & -3 \end{pmatrix} \tag{A.36}$$

APPENDIX B

$\pi\rho\omega$ SYSTEM PHOTOEMISSION RATE PARAMETRIZATIONS

In this appendix, we present parametrizations of the photo-emission rates for each process in the $\pi\rho\omega$ system, along with plots of comparisons of parametrizations to calculated rates. We have verified the accuracy of the parametrizations to within 10% for temperature and photon energy ranges of $100\,\mathrm{MeV} \leq T \leq 180\,\mathrm{MeV}$ and $0.2\,\mathrm{GeV} \leq q_0 \leq 5.0\,\mathrm{GeV}$, except for the lowest photon energies of the $\rho\omega \to \gamma\pi$ process, whose overall contribution in that photon energy range is negligible. Form factor effects are included in all rate parametrizations.

- $\underline{\pi\rho \to \gamma\omega}$

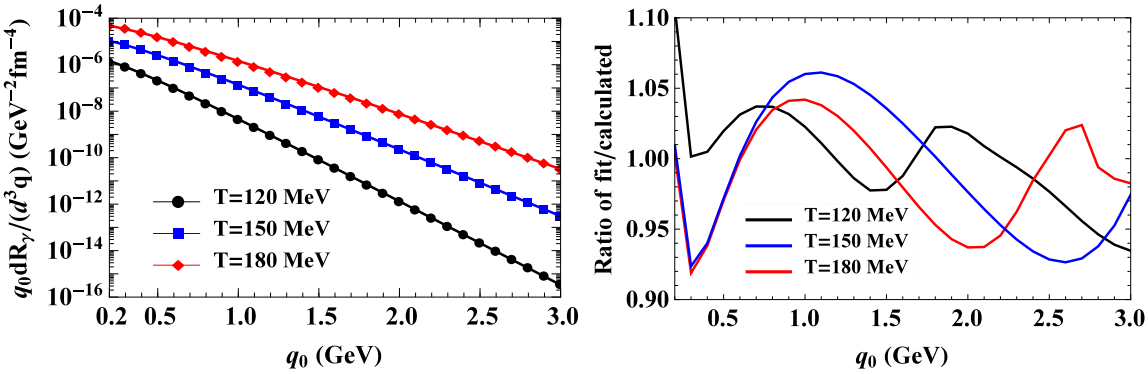

Figure B.1: Left panel: Calculated thermal photo-emission rates from the $\pi\rho \to \gamma\omega$ process (symbols) compared to the parametrized rates (lines). Right panel: Ratio of parametrized rates to calculated rates.

$$
\begin{aligned}
q_0\frac{dR_{\pi\rho\to\gamma\omega}}{d^3q} &= \exp\left[a_1 q_0 + a_2 + a_3 q_0^{a_4} + a_5(q_0+a_6)^{a_7}\right]\ \left[\mathrm{fm}^{-4}\,\mathrm{GeV}^{-2}\right]\ , \qquad \text{(B.1)}\\
a_1(T) &= -35.8991 + 460.425\,T - 2592.04\,T^2 + 5342.32\,T^3\ ,\\
a_2(T) &= -41.9725 + 601.952\,T - 3587.8\,T^2 + 7604.97\,T^3\ ,\\
a_3(T) &= 0.740436 - 16.7159\,T + 133.526\,T^2 - 347.589\,T^3\ ,\\
a_4(T) &= 2.00611 - 3.79343\,T + 29.3101\,T^2 - 72.8725\,T^3\ , \qquad \text{(B.2)}\\
a_5(T) &= -8.33046 + 121.091\,T - 801.676\,T^2 + 1712.16\,T^3\ ,\\
a_6(T) &= 17.9029 - 388.5\,T + 2779.03\,T^2 - 6448.4\,T^3\ ,\\
a_7(T) &= -15.622 + 340.651\,T - 2483.18\,T^2 + 5870.61\,T^3\ .
\end{aligned}
$$

- $\underline{\pi\omega \to \gamma\rho}$

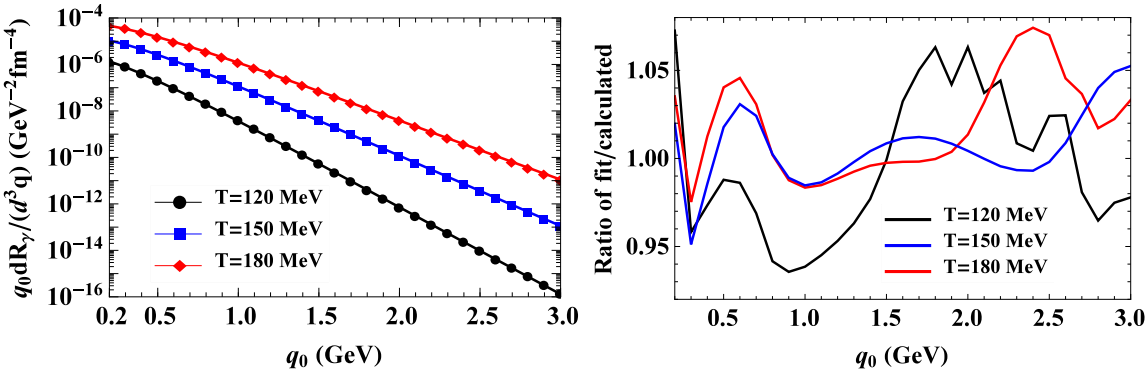

Figure B.2: Left panel: Calculated thermal photo-emission rates from the $\pi\omega \to \gamma\rho$ process (symbols) compared to the parametrized rates (lines). Right panel: Ratio of parametrized rates to calculated rates.

$$
\begin{aligned}
q_0 \frac{dR_{\pi\omega\to\gamma\rho}}{d^3q} &= \exp\left[a_1 q_0 + a_2 + a_3 q_0^{a_4} + a_5 (q_0 + a_6)^{a_7}\right] \left[\mathrm{fm}^{-4}\,\mathrm{GeV}^{-2}\right] \ , \quad \text{(B.3)} \\
a_1(T) &= -29.4663 + 291.356\,T - 1301.27\,T^2 + 2102.12\,T^3 \ , \\
a_2(T) &= -45.081 + 688.929\,T - 4150.15\,T^2 + 8890.76\,T^3 \ , \\
a_3(T) &= -0.260076 + 8.92875\,T - 60.868\,T^2 + 136.57\,T^3 \ , \\
a_4(T) &= 2.2663 - 8.30596\,T + 49.3342\,T^2 - 90.8501\,T^3 \ , \quad \text{(B.4)} \\
a_5(T) &= 10.2955 - 317.077\,T + 2412.15\,T^2 - 6020.9\,T^3 \ , \\
a_6(T) &= 3.12251 - 47.5277\,T + 222.61\,T^2 - 241.9\,T^3 \ , \\
a_7(T) &= -3.39045 + 56.5927\,T - 336.97\,T^2 + 622.756\,T^3 \ .
\end{aligned}
$$

- $\underline{\rho\omega \to \gamma\pi}$

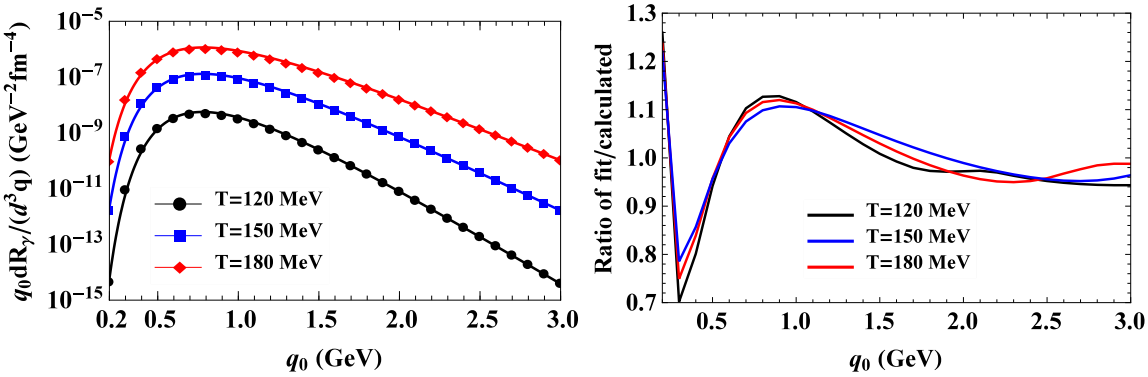

Figure B.3: Left panel: Calculated thermal photo-emission rates from the $\rho\omega \to \gamma\pi$ process (symbols) compared to the parametrized rates (lines). Right panel: Ratio of parametrized rates to calculated rates.

$$q_0 \frac{dR_{\rho\omega\to\gamma\pi}}{d^3q} = \exp\left[a_1 q_0 + a_2 + \frac{a_3}{(q_0+0.2)} + \frac{a_4}{(q_0+0.2)^2}\right] \left[\mathrm{fm}^{-4}\,\mathrm{GeV}^{-2}\right] \quad , \tag{B.5}$$

$$\begin{aligned} a_1(T) &= -29.6866 + 331.769\,T - 1618.66\,T^2 + 2918.53\,T^3 \ , \\ a_2(T) &= -15.3332 + 90.2225\,T - 300.185\,T^2 + 428.386\,T^3 \ , \\ a_3(T) &= -7.35061 + 109.288\,T - 630.396\,T^2 + 1227.69\,T^3 \ , \\ a_4(T) &= -10.6044 + 109.1\,T - 500.718\,T^2 + 872.951\,T^3 \ . \end{aligned} \tag{B.6}$$

APPENDIX C

NON-RELATIVISTIC REDUCTION OF SPINORS

In this appendix we present our method of non-relativistic reduction of Dirac and Rarita-Schwinger spinors. Note we use the Dirac spinor normalization of $\bar{\psi}\psi = 2m$.

The basic motivation is simple. For a given Lagrangian interaction, we simply drop any spinor components which are of order $\vec{p}/m$ or higher. A four-component Dirac spinor has the form

$$\psi(\vec{p}, s) = \sqrt{E(\vec{p}) + m} \begin{pmatrix} \chi(s) \\ \frac{\vec{\sigma}\cdot\vec{p}}{E+m}\chi(s) \end{pmatrix} , \tag{C.1}$$

where $E = \sqrt{\vec{p}^2 + m^2}$ and the numerical prefactor is for normalization purposes. The χ are two-component spinors representing the spin state of the particle, such that

$$\chi(+\frac{1}{2}) = \begin{pmatrix} 1 \\ 0 \end{pmatrix} \quad \chi(-\frac{1}{2}) = \begin{pmatrix} 0 \\ 1 \end{pmatrix} . \tag{C.2}$$

To obtain the non-relativistic reduction of the Dirac spinor, we omit its lower two components. We then have the simple reduction of

$$\psi(\vec{p}, s) \to \begin{pmatrix} \chi(s) \\ 0 \end{pmatrix} , \tag{C.3}$$

where each component of this 1x2 matrix is, in turn, a 1x2 matrix.

For spin-3/2 particles, we must evaluate the reduction of Rarita-Schwinger spinors. These are constructed out of Dirac spinors with spin $s = \frac{1}{2}$, Lorentz polarization vector with spin $l = 1$, and $\frac{1}{2} \otimes 1 = \frac{3}{2} = j$ Clebsch-Gordan coefficients, such that

[96, 105, 126]

$$\psi^{\mu}(\vec{p}, m_j) = \sum_{m_l=-1}^{1} \sum_{m_s=-1/2}^{1/2} \left(1, m_l; \frac{1}{2}, m_s | \frac{3}{2}, m_j\right) u(\vec{p}, m_s) e^{\mu}(\vec{p}, m_l)\,, \tag{C.4}$$

where the m_i are the z-components of the respective spin. In the particle's rest frame, the Lorentz polarization vector has components in a spherical basis $\hat{e}_\lambda$ of

$$\vec{e}_{\lambda=+1} = -\frac{1}{\sqrt{2}} \begin{pmatrix} 1 \\ i \\ 0 \end{pmatrix}, \quad \vec{e}_{\lambda=-1} = \frac{1}{\sqrt{2}} \begin{pmatrix} 1 \\ -i \\ 0 \end{pmatrix}, \quad \vec{e}_{\lambda=0} = \begin{pmatrix} 0 \\ 0 \\ 1 \end{pmatrix}. \tag{C.5}$$

The general polarization four-vector e_μ is found by boosting the three-vector into a general Lorentz frame [96]:

$$e^{\mu}(p, \lambda) = \left(\hat{e}_\lambda \cdot \frac{\vec{p}}{m}, \hat{e}_\lambda + \frac{\vec{p}(\hat{e}_\lambda \cdot \vec{p})}{m(p_0 + m)}\right). \tag{C.6}$$

Note that in the $|\vec{p}|/m$ expansion, this vector becomes

$$e^{\mu}(\vec{p}, \lambda) = (0, \hat{e}_\lambda)^{\mu} + \mathcal{O}(\frac{|\vec{p}|}{m})\,. \tag{C.7}$$

We now introduce the total spin-3/2 spinors

$$\chi^{(3/2)}(\frac{3}{2}) = \begin{pmatrix} 1 \\ 0 \\ 0 \\ 0 \end{pmatrix}, \; \chi^{(3/2)}(\frac{1}{2}) = \begin{pmatrix} 0 \\ 1 \\ 0 \\ 0 \end{pmatrix}, \; \chi^{(3/2)}(-\frac{1}{2}) = \begin{pmatrix} 0 \\ 0 \\ 1 \\ 0 \end{pmatrix}, \; \chi^{(3/2)}(-\frac{3}{2}) = \begin{pmatrix} 0 \\ 0 \\ 0 \\ 1 \end{pmatrix}. \tag{C.8}$$

By performing the non-relativistic reduction on the Lorentz polarization vector and

the Dirac spinor in Eq. (C.4), and by introducing the expression for the components of the transition operator $\vec{S}$

$$\vec{S} = \sum_{m_j, m_l, m_s} \left(1, m_l; \frac{1}{2}, m_s | \frac{3}{2}, m_j\right) \chi^{(3/2)}(m_j) \chi^{\dagger}(m_s) \vec{e}^{*}(m_l)\,, \tag{C.9}$$

we have the simple result of

$$u^0(\vec{p}, m_j) \to 0, \quad u^i(\vec{p}, m_j) \to \begin{pmatrix} S_i^{\dagger} \chi^{(3/2)}(m_j) \\ 0 \end{pmatrix}. \tag{C.10}$$

To see how these spinor reductions simplify interactions, let us examine the P-wave πNN interaction given in Sec. 5.2.1. Let us examine only the spin structure of this interaction; we shall address isospin below. We have

$$\mathcal{L}_{\pi NN} = \frac{f_{\pi B_1 B_2}}{m_\pi} \bar{\psi} (i\gamma_5) \gamma^\mu \partial_\mu \pi \psi \to \frac{f_{\pi B_1 B_2}}{m_\pi} \chi^{\dagger} (\gamma_5) \gamma^\mu k_\mu \chi\,. \tag{C.11}$$

We now write the Dirac matrices in the form (recall we work in the Dirac basis)

$$\gamma_0 = \begin{pmatrix} \mathbb{1}^{(2)} & 0 \\ 0 & -\mathbb{1}^{(2)} \end{pmatrix}, \quad \vec{\gamma} = \begin{pmatrix} 0 & \vec{\sigma} \\ -\vec{\sigma} & 0 \end{pmatrix}, \quad \gamma_5 = \begin{pmatrix} 0 & \mathbb{1}^{(2)} \\ \mathbb{1}^{(2)} & 0 \end{pmatrix}, \tag{C.12}$$

where $\mathbb{1}^{(2)}$ represents a the 2x2 identity matrix and $\vec{\sigma}$ is the Pauli matrix vector. Now

we write out the four-product between the momentum k and the gamma matrices:

$$\begin{aligned}\mathcal{L}_{\pi NN} &= \frac{f_{\pi B_1 B_2}}{m_\pi}\begin{pmatrix} \chi^\dagger & 0 \end{pmatrix}\begin{pmatrix} 0 & \mathbb{1}^{(2)} \\ \mathbb{1}^{(2)} & 0 \end{pmatrix}\begin{pmatrix} k_0 & -\vec{k}\cdot\vec{\sigma} \\ \vec{k}\cdot\vec{\sigma} & -k_0 \end{pmatrix}\begin{pmatrix} \chi \\ 0 \end{pmatrix} \\ &= \frac{f_{\pi B_1 B_2}}{m_\pi}\begin{pmatrix} \chi^\dagger & 0 \end{pmatrix}\begin{pmatrix} \vec{k}\cdot\vec{\sigma} & -k_0 \\ k_0 & -\vec{k}\cdot\vec{\sigma} \end{pmatrix}\begin{pmatrix} \chi \\ 0 \end{pmatrix} \\ &= \frac{f_{\pi B_1 B_2}}{m_\pi}\chi^\dagger\left(\vec{k}\cdot\vec{\sigma}\right)\chi\,. \end{aligned} \tag{C.13}$$

This is the origin of the spin structure of our P-wave πNN vertex. Note that since we did not alter the isospin structure of this interaction, it remains as it was in the relativistic Lagrangian. Now let us examine the interaction between π, N, and N^*, where the latter has a negative parity. In this case, we remove the γ_5 from the Lagrangian. This gives

$$\begin{pmatrix} \chi^\dagger & 0 \end{pmatrix}\begin{pmatrix} k_0 & -\vec{k}\cdot\vec{\sigma} \\ \vec{k}\cdot\vec{\sigma} & -k_0 \end{pmatrix}\begin{pmatrix} \chi \\ 0 \end{pmatrix} = \chi^\dagger\left(k_0\right)\chi\,. \tag{C.14}$$

This is our S-wave interaction. Before we examine the D-wave interaction, let us look at the reduction of the $\pi\Delta\Delta$ interaction given by Eq. (5.6). Again suppressing isospin, we have

$$\mathcal{L}_{\pi\Delta\Delta} = \frac{f_{\pi\Delta\Delta}}{m_\pi}\bar{\psi}_\mu\left(i\gamma_5\right)\gamma^\nu\partial_\nu\pi\psi^\mu\,. \tag{C.15}$$

Inserting the above reductions for the Rarita-Schwinger spinors, we have

$$\begin{aligned}
\mathcal{L}_{\pi\Delta\Delta} &= \frac{f_{\pi\Delta\Delta}}{m_\pi} \begin{pmatrix} S_i^\dagger \chi^{(3/2)} \\ 0 \end{pmatrix}^\dagger \begin{pmatrix} 0 & \mathbb{1}^{(2)} \\ \mathbb{1}^{(2)} & 0 \end{pmatrix} \begin{pmatrix} k_0 & -\vec{k}\cdot\vec{\sigma} \\ \vec{k}\cdot\vec{\sigma} & -k_0 \end{pmatrix} \begin{pmatrix} S_i^\dagger \chi^{(3/2)} \\ 0 \end{pmatrix} \\
&= \frac{f_{\pi\Delta\Delta}}{m_\pi} \begin{pmatrix} \chi^{\dagger(3/2)} S_i & 0 \end{pmatrix} \begin{pmatrix} \vec{k}\cdot\vec{\sigma} & -k_0 \\ k_0 & -\vec{k}\cdot\vec{\sigma} \end{pmatrix} \begin{pmatrix} S_i^\dagger \chi^{(3/2)\dagger} \\ 0 \end{pmatrix} \\
&= \frac{f_{\pi\Delta\Delta}}{m_\pi} \chi^{\dagger(3/2)} \left(S_i \sigma_j S_i^\dagger k_j \right) \chi^{(3/2)} \,. \qquad \text{(C.16)}
\end{aligned}$$

However, one can show by direct calculation that

$$\sum_i S_i \sigma_j S_i^\dagger = S_j^{(3/2)} \qquad \text{(C.17)}$$

. We then have a non-relativistic $\pi\Delta\Delta$ interaction of

$$\mathcal{L}_{\pi\Delta\Delta} = \frac{f_{\pi\Delta\Delta}}{m_\pi} \chi^{\dagger(3/2)} \left(\vec{k}\cdot\vec{S}^{(3/2)} \right) \chi^{(3/2)} \,. \qquad \text{(C.18)}$$

Now that the reduction of Rarita-Schwinger spinors has been established, we can move on to a D-wave interaction, which occurs in a $\pi B_1 B_2$ interaction when the baryons have opposite parity, one baryon is spin-1/2, and the other baryon is spin-3/2. As mentioned in Sec. 5.2.1, we encounter an issue with this interaction when using a simple derivative coupling. Let us demonstrate by performing the non-relativistic reduction. First, the relativistic D-wave interaction is, neglecting the coupling constant and isospin

$$\mathcal{L} = \bar{\psi}^\mu \gamma_5 \partial_\mu \pi \psi \,. \qquad \text{(C.19)}$$

Now we insert the non-relativistic spinors and carry out the matrix multiplication:

$$\begin{aligned}\mathcal{L} &= \begin{pmatrix} \chi^{\dagger(3/2)} S_i & 0 \end{pmatrix} \begin{pmatrix} 0 & \mathbb{1}^{(2)} \\ \mathbb{1}^{(2)} & 0 \end{pmatrix} k_i \begin{pmatrix} \chi \\ 0 \end{pmatrix} \\ &= \begin{pmatrix} \chi^{\dagger(3/2)} S_i & 0 \end{pmatrix} k_i \begin{pmatrix} 0 \\ \chi \end{pmatrix} \\ &= 0\,. \end{aligned} \tag{C.20}$$

The lack of a γ_μ matrix causes the γ_5 matrix to "flip" one of the spinors, causing the product to vanish. This is the reason for our D-wave ansatz of [106]

$$\mathcal{L}^D = \bar{\psi}^\mu \gamma_5 \gamma^\nu \partial_\nu \partial_\mu \pi \psi\,. \tag{C.21}$$

Let us examine the non-relativistic reduction of this interaction. Inserting the non-relativistic spinors, we have

$$\begin{aligned}\mathcal{L}^D &= \begin{pmatrix} \chi^{\dagger(3/2)} S_i & 0 \end{pmatrix} \begin{pmatrix} 0 & \mathbb{1}^{(2)} \\ \mathbb{1}^{(2)} & 0 \end{pmatrix} \begin{pmatrix} k_0 & -\vec{k}\cdot\vec{\sigma} \\ \vec{k}\cdot\vec{\sigma} & -k_0 \end{pmatrix} k_i \begin{pmatrix} \chi \\ 0 \end{pmatrix} \\ &= \begin{pmatrix} \chi^{\dagger(3/2)} & 0 \end{pmatrix} \vec{k}\cdot\vec{S} \begin{pmatrix} \vec{k}\cdot\vec{\sigma} & -k_0 \\ k_0 & -\vec{k}\cdot\vec{\sigma} \end{pmatrix} \begin{pmatrix} \chi \\ 0 \end{pmatrix} \\ &= \chi^{\dagger(3/2)} \left[(\vec{k}\cdot\vec{S})(\vec{k}\cdot\vec{\sigma}) \right] \chi \end{aligned} \tag{C.22}$$

This is our non-relativistic D-wave interaction.

We also simplify the baryonic propagators by neglecting antiparticle contributions, but keeping relativistic kinematics in the denominator. We do so by separating

the two propagator poles via partial fraction decomposition:

$$G_B(p) = \frac{\sum\limits_{\text{spin}} \bar{\psi}\psi}{p^2 - m_B^2 + i\epsilon} = \frac{\sum\limits_{\text{spin}} \bar{\psi}\psi}{2\omega_B(\vec{p})} \left(\frac{1}{p_0 - \omega_B(\vec{p}) + i\epsilon} - \frac{1}{p_0 + \omega_B(\vec{p}) - i\epsilon} \right)$$
$$\rightarrow \frac{\sum\limits_{\text{spin}} \bar{\chi}\chi}{2\omega_B(\vec{p})} \frac{1}{p_0 - \omega_B(\vec{p}) + i\epsilon} = \frac{1}{p_0 - \omega_B(\vec{p}) + i\epsilon}\,, \tag{C.23}$$

where $\omega_B(\vec{p}) = \sqrt{\vec{p}^2 + m_B^2}$ is the on-shell energy of the baryon. The final simplification is a result of our spinor normalization of $\sum\limits_{\text{spin}} \bar{\chi}\chi = 2m_B$.

Since we now have our non-relativistic baryon propagators, the reduction of baryon interactions with the ρ is straightforward, giving

$$\mathcal{L}^{+}_{\rho BB} = -g_\rho \chi^\dagger \rho_\mu \begin{pmatrix} \mathbb{1} \\ 0 \end{pmatrix}^\mu (\vec{\rho} \cdot \vec{\mathcal{T}})\, \chi\,. \tag{C.24}$$

However, there is a problem with this non-relativistic ρBB interaction. As mentioned in Sec. 5.2.2, the fully relativistic ρBB vertex, Γ_μ, satisfies a Ward-Takahashi identity [113, 114]. The Lorentz structure of this identity is

$$q^\mu \Gamma_\mu(p,q) = -ig_\rho \left(\tilde{G}_B^{-1}(p+q) - \tilde{G}_B^{-1}(p) \right)\,, \tag{C.25}$$

where p and q are the four-momenta of the baryon and ρ, respectively, and $\tilde{G}_B$ is the baryon's fully relativistic fermionic propagator. However, if we use our non-relativistic propagators and ρBB vertex in this identity, we find (suppressing isospin)

$$\begin{aligned} q^\mu \Gamma_\mu(p,q) &= -ig_\rho \left(G_B^{-1}(p+q) - G_B^{-1}(p) \right) \\ -ig_\rho q_0 &= -ig_\rho \left[q_0 + \omega_B(p+q) - \omega_B(p) \right] \\ &= -ig_\rho q_0 + \mathcal{O}\left(\frac{|\vec{q}|}{m_B} \right)\,. \end{aligned} \tag{C.26}$$

Thus the Ward-Takahashi identity is not fulfilled, indicating a breakdown of gauge invariance. However, since the non-relativistic vertex is only calculated to order $(\frac{|\vec{q}|}{m_B})^0$, we can add in a term of order $(\frac{|\vec{q}|}{m_B})^1$ without affecting the accuracy of our reductions. Therefore, we can simply add in a term to the non-relativistic vertex which causes it to fulfill the Ward-Takahashi identity. The new vertex is then

$$\Gamma_\mu(p,q) = \begin{pmatrix} -ig_\rho \frac{G_B^{-1}(p+q) - G_B^{-1}(p)}{q_0} \\ 0 \end{pmatrix}_\mu . \tag{C.27}$$

APPENDIX D

LIST OF PARTICLE PROPERTIES

Particle	Mass (MeV)	J^P	I
$\pi^{\pm}$	139.6	0^-	1
π^0	135.0	0^-	1
ρ	775	1^+	1
ω	783	1^+	0
N	939	$\frac{1}{2}^+$	$\frac{1}{2}$
$N(1440)$	1440	$\frac{1}{2}^+$	$\frac{1}{2}$
$N(1520)$	1520	$\frac{3}{2}^-$	$\frac{1}{2}$
$N(1535)$	1535	$\frac{1}{2}^-$	$\frac{1}{2}$
$N(1650)$	1650	$\frac{1}{2}^-$	$\frac{1}{2}$
$N(1700)$	1700	$\frac{3}{2}^-$	$\frac{1}{2}$
$N(1710)$	1710	$\frac{1}{2}^+$	$\frac{1}{2}$
$N(1720)$	1720	$\frac{3}{2}^+$	$\frac{1}{2}$
$N(1875)$	1875	$\frac{3}{2}^-$	$\frac{1}{2}$
$N(1900)$	1900	$\frac{3}{2}^+$	$\frac{1}{2}$
Δ	1232	$\frac{3}{2}^+$	$\frac{3}{2}$
$\Delta(1600)$	1600	$\frac{3}{2}^+$	$\frac{3}{2}$
$\Delta(1620)$	1620	$\frac{1}{2}^-$	$\frac{3}{2}$
$\Delta(1700)$	1700	$\frac{3}{2}^-$	$\frac{3}{2}$
$\Delta(1910)$	1910	$\frac{1}{2}^+$	$\frac{3}{2}$
$\Delta(1920)$	1920	$\frac{3}{2}^+$	$\frac{3}{2}$

Particle	Mass (MeV)	J^P	I
Λ	1115	$\frac{1}{2}^+$	0
$\Lambda(1405)$	1405	$\frac{1}{2}^-$	0
$\Lambda(1520)$	1520	$\frac{3}{2}^-$	0
$\Lambda(1600)$	1600	$\frac{1}{2}^+$	0
$\Lambda(1670)$	1670	$\frac{1}{2}^-$	0
$\Lambda(1690)$	1690	$\frac{3}{2}^-$	0
$\Lambda(1810)$	1810	$\frac{1}{2}^+$	0
$\Lambda(1890)$	1890	$\frac{3}{2}^+$	0
Ξ	1315	$\frac{1}{2}^+$	$\frac{1}{2}$
$\Xi(1530)$	1530	$\frac{3}{2}^+$	$\frac{1}{2}$
Σ	1190	$\frac{1}{2}^+$	1
$\Sigma(1385)$	1385	$\frac{3}{2}^+$	1
$\Sigma(1670)$	1670	$\frac{3}{2}^-$	1

Table D.1: Basic properties of particles used in this work.

Parent	Full Width (MeV)	Decay Mode	Partial Width (%)	Partial Wave	p_{CM} (MeV)
$N(1440)$	350	$N\pi$	65	P	391
	350	$\Delta\pi$	20	P	135
$N(1520)$	115	$N\pi$	60	D	453
	115	$\Delta\pi$	15	S	225
$N(1535)$	150	$\Delta\pi$	2	D	242
	150	$N\pi$	45	S	468
$N(1650)$	140	$\Delta\pi$	12.5	D	344
	140	$N\pi$	60	S	546
	140	$N(1440)\pi$	3	S	147
$N(1700)$	150	$\Delta\pi$	50	S	385
	150	$N\pi$	12	D	580
$N(1710)$	125	$N\pi$	12.5	P	587
	125	$\Delta\pi$	39	P	393
	125	$N(1535)\pi$	15	S	100
$N(1720)$	250	$N\pi$	11	P	593
	250	$\Delta\pi$	75	P	401
$N(1875)$	250	$N\pi$	7	D	694
	250	$\Delta\pi$	40	S	520
$N(1900)$	200	$N\pi$	5	P	710
	250	$\Delta\pi$	7	D	305
Δ	117	$N\pi$	100	P	229
$\Delta(1600)$	320	$N\pi$	17.5	P	513
	320	$\Delta\pi$	55	P	328
	320	$N(1440)\pi$	22.5	S	75
$\Delta(1620)$	140	$N\pi$	25	S	534
	140	$\Delta\pi$	45	D	318
	140	$N(1440)\pi$	9.5	P	107
$\Delta(1700)$	300	$N\pi$	15	D	580
	300	$\Delta\pi$	37.5	S	385
$\Delta(1910)$	280	$N\pi$	22.5	P	716
	280	$\Delta\pi$	60	P	545
	280	$N(1440)\pi$	47	P	393
$\Delta(1920)$	150	$N\pi$	12.5	P	722

Table D.2: Nucleon and Δ particle decay data used to calculate $f_{\pi B_1 B_2}$ coupling constants. Partial widths are the average of minimum and maximum uncertainty ranges listed in PDG [9].

Parent	Full Width (MeV)	Decay Mode	Partial Width (%)	Partial Wave	p_{CM} (MeV)
$\Lambda(1405)$	50	$\Sigma\pi$	100	S	151
$\Lambda(1520)$	16	$\Sigma\pi$	42	D	266
$\Lambda(1600)$	150	$\Sigma\pi$	35	P	336
$\Lambda(1670)$	35	$\Sigma\pi$	40	S	393
$\Lambda(1690)$	60	$\Sigma\pi$	30	D	409
$\Lambda(1810)$	150	$\Sigma\pi$	25	S	500
$\Lambda(1890)$	100	$\Sigma\pi$	10	P	558
$\Sigma(1385)$	36	$\Lambda\pi$	87	P	208
$\Sigma(1385)$	36	$\Sigma\pi$	11.7	P	126
$\Sigma(1670)$	60	$\Sigma\pi$	45	D	415
$\Xi(1530)$	10	$\Xi\pi$	1	P	654

Table D.3: Hyperon particle decay data used to calculate $f_{\pi B_1 B_2}$ coupling constants. Partial widths are the average of minimum and maximum uncertainty ranges listed in PDG [9].

Parent	$A^p_{1/2}$	$A^n_{1/2}$	$A^p_{3/2}$	$A^n_{3/2}$	p_{CM} (MeV)	$g_{\omega NN^*}$
$N(1440)$	-0.060	0.040	0	0	414	0.867
$N(1520)$	-0.020	-0.050	0.140	-0.115	470	2.711
$N(1535)$	0.115	-0.075	0	0	480	1.228
$N(1650)$	0.045	-0.050	0	0	558	0.193
$N(1700)$	0.015	0.020	-0.015	-0.030	591	2.968
$N(1710)$	0.040	-0.040	0	0	597	0
$N(1720)$	0.100	-0.080	0.150	-0.140	604	2.091

Table D.4: Data used to calculate coupling constants for ωNN^* interactions derived from helicity amplitudes. Helicity amplitudes taken from PDG [9].

Coupling	Value
$f_{\pi NN}$	1.1
$f_{\pi N\Delta}$	3.044
$f_{NN(1440)}$	0.576
$f_{NN(1520)}$	0.125
$f_{NN(1535)}$	0.253
$f_{N\Delta(1600)}$	0.668
$f_{N\Delta(1620)}$	0.285
$f_{NN(1650)}$	0.252
$f_{NN(1700)}$	0.049
$f_{N\Delta(1700)}$	0.109
$f_{NN(1710)}$	0.095
$f_{NN(1720)}$	0.243
$f_{NN(1875)}$	0.030
$f_{NN(1900)}$	0.138
$f_{N\Delta(1910)}$	0.332
$f_{N\Delta(1920)}$	0.412

Coupling	Value
$f_{\pi\Delta N(1440)}$	1.785
$f_{\pi\Delta N(1520)}$	0.305
$f_{\pi\Delta N(1535)}$	0.128
$f_{\pi\Delta\Delta(1600)}$	0.464
$f_{\pi\Delta\Delta(1620)}$	0.158
$f_{\pi\Delta N(1650)}$	0.135
$f_{\pi\Delta N(1700)}$	0.368
$f_{\pi\Delta\Delta(1700)}$	0.329
$f_{\pi\Delta N(1710)}$	0.338
$f_{\pi\Delta N(1720)}$	0.531
$f_{\pi\Delta N(1875)}$	0.328
$f_{\pi\Delta\Delta(1910)}$	0.379
$f_{\pi N(1440)\Delta(1600)}$	4.903
$f_{\pi N(1440)\Delta(1620)}$	0.754
$f_{\pi N(1440)N(1650)}$	0.185
$f_{\pi N(1440)\Delta(1910)}$	0.702
$f_{\pi N(1535)N(1710)}$	0.487
$f_{\pi N(1535)N(1900)}$	0.142

Coupling	Value
$f_{\Sigma\Sigma(1385)}$	0.683
$f_{\Sigma\Lambda(1405)}$	1.093
$f_{\Sigma\Lambda(1520)}$	0.216
$f_{\Sigma\Lambda(1600)}$	0.541
$f_{\Sigma\Lambda(1670)}$	0.222
$f_{\Sigma\Sigma(1670)}$	0.155
$f_{\Sigma\Lambda(1690)}$	0.131
$f_{\Sigma\Lambda(1810)}$	0.306
$f_{\Sigma\Lambda(1890)}$	0.251
$f_{\Lambda\Sigma(1385)}$	0.325
$f_{\Lambda\Sigma(1670)}$	0.110
$f_{\Xi\Xi(1530)}$	0.654
$g_{\omega NN}$	11.0
$g_{\omega NN(1440)}$	0.867
$g_{\omega NN(1520)}$	2.711
$g_{\omega NN(1535)}$	1.228
$g_{\omega NN(1650)}$	0.445
$g_{\omega NN(1700)}$	0.193
$g_{\omega NN(1710)}$	0.0
$g_{\omega NN(1720)}$	2.091
$g_{\omega NN(1875)}$	2.015
$g_{\omega NN(1900)}$	2.887

Table D.5: Baryonic coupling constants used in this work.